EXPLORING SINGLE HOLE STATES IN INAS/GAAS QUANTUM DOTS AND QUANTUM DOT MOLECULES UNDER 2-D ELECTRIC FIELDS

by

Xiangyu Ma

A Dissertation submitted to the Faculty of the University of Delaware in partial fulfillment of the requirements for the degree of Doctor of Philosophy in Physics

Fall 2018

EXPLORING SINGLE HOLE STATES IN INAS/GAAS QUANTUM DOTS AND QUANTUM DOT MOLECULES UNDER 2-D ELECTRIC FIELDS

by

Xiangyu Ma

Approved: _____
Edmund R. Nowak, Ph.D.
Chair of the Department of Physics and Astronomy

Approved: _____
John A. Pelesko, Ph.D.
Interim Dean of the College of the Arts and Sciences

Approved: _____
Douglas J. Doren, Ph.D.
Interim Vice Provost for Graduate and Professional Education

I certify that I have read this Dissertation and that in my opinion it meets the academic and professional standard required by the University as a Dissertation for the degree of Doctor of Philosophy.

Signed: _____

Matthew Doty, Ph.D.
Professor in charge of Dissertation

I certify that I have read this Dissertation and that in my opinion it meets the academic and professional standard required by the University as a Dissertation for the degree of Doctor of Philosophy.

Signed: _____

Garnett Bryant, Ph.D.
Member of Dissertation committee

I certify that I have read this Dissertation and that in my opinion it meets the academic and professional standard required by the University as a Dissertation for the degree of Doctor of Philosophy.

Signed: _____

Lars Gundlach, Ph.D.
Member of Dissertation committee

I certify that I have read this Dissertation and that in my opinion it meets the academic and professional standard required by the University as a Dissertation for the degree of Doctor of Philosophy.

Signed: _____

John Xiao, Ph.D.
Member of Dissertation committee

I certify that I have read this Dissertation and that in my opinion it meets the academic and professional standard required by the University as a Dissertation for the degree of Doctor of Philosophy.

Signed: _____

Joshua Zide, Ph.D.
Member of Dissertation committee

ACKNOWLEDGEMENTS

I graduated with a Bachelor of Science degree in Astronomy at Nanjing University. I shifted my research interests from astrophysics in college to semiconductor science in graduate school when I first joined UD. Although there are similarities between analyzing the spectra of a star and analyzing the spectra of a semiconductor, the transition wasn't easy. I'm sincerely grateful for the knowledge Dr. Doty has shared with me, which helps my transition and brings me to the wonderland of solid-state physics. I could not have finished my dissertation without his invaluable guidance and generous support for the past 6 years. I also want to thank all my committee members for their mentorship, and I want to thank Dr. Bruce Chase, and all the UDNF staff members for their incredible support in helping me complete this program.

I want to extend my acknowledgment to all my friends and family members, for supporting me through this unbelievable journey. I want to give special thanks to my group members past and present, for their useful discussions and lab-work: Dr. Darry Liu, Dr. Xinran Zhou, Dr. Chelsea Haughn, Dr. Laura Vanderhoef, Dr. Anagha Kulkarni, Dr. Diane Sellers, Dr. Eric Chen, Dr. Chris Milleville, Dr. Yu-sheng Ou, Zhuohui Li, Henry Carfagno, Jill Cleveland, Jamie Beshore. Moreover, I want to express my gratitude to the MBE group members, especially Dr. Jing Zhang, and Yuejing Wang, who helped growing the QDs. I'm also lucky to spend three months studying in Germany with Dr. Joerg Martin, who taught me many things about device engineering and fabrication.

Last and the most important, I cannot express how thankful I am for my husband Matt. He stands by me regardless of sickness and health, and he encourages me when I feel joy and sorrow. He helps me build systematic thought processes and

challenges me to be a better person. I could not accomplish my degree without his love and encouragement.

TABLE OF CONTENTS

Chapter

LIST OF TABLES

LIST OF FIGURES

xviii

ABSTRACT

InAs/GaAs quantum dots (QDs) and quantum dot molecules (QDMs) are self-assembled semiconductor nanostructures that can trap a single electron or hole in a 3-D potential-well. Grown by molecular beam epitaxy (MBE), they have excellent optical qualities that can be used in applications for quantum information processing and quantum computing. Specifically, hole spins in a single QD/QDM have longer decoherence time than electron spins due to the lack of hyperfine interaction, making hole spins a great qubit candidate. However, many challenges such as QD growth, device integration, and spin manipulation inhibit the scalability of a hole-spin-based quantum information platform. A deeper understanding of the hole spin physics and the QD/QDM material system is needed to advance device engineering opportunities.

In this dissertation work, we explore a hole spin in an InAs/GaAs QD/QDM under a 2-D electric field. We develop a hybrid computational method that combines a tight-binding atomistic simulation and a finite matrix approximation. This hybrid method can quickly explore the properties of a single hole spin state under a variety of electric field conditions. We discover that a hole spin in a single QD can be polarized in the vertical direction with an in-plane (lateral) electric field and a Voigt (lateral) direction magnetic field. We show that this effect persists with different QD shape, composition, and orientation. We also demonstrate the ability to control hole spin states using a lateral electric field in a QDM, particularly the ability to induce hole spin mixing with a gradient 2-D electric field. We will discuss the spin texture concept that explains these exotic spin effects using an animated visualization algorithm.

We also present the experimental effort to apply 2-D electric field to a single QD/QDM. We use COMSOL semiconductor simulation to design a 3-electrode device that can apply 2-D electric field in GaAs. We discuss a range of device parameters and

their influence on the device performance. We grow a single QD sample in an intrinsic GaAs matrix using MBE. We fabricate the 3-electrode device on this sample using electron beam lithography, ICP etching, Ion Milling and angled e-beam metal evaporation. The device is then characterized by low-temperature micro-photoluminescence. We show that we are able to control the charging of a single hole state in a QD using two different voltage geometries. Combining the experimental data with the COMSOL simulation results, we show the charging comes from the induced 2-D electric field around a single QD. We will discuss the improvements required to continue on the path to full 2-D field control of a single QD.

<div align="center">

Chapter 1

INTRODUCTION

</div>

1.1 Quantum Computing Introduction

1.1.1 Concept of Quantum Computing

Classical computers use transistors to indicate logic, which can be either 0 or 1. This binary logic architecture has grown with Moore's law for the past decades, shaping the fundamentals of our current digital infrastructures. However, to keep increasing the computational power of a classical CPU, logic gates have to become smaller and smaller so that more computational units can be integrated per area. This strategy will eventually hit the quantum barrier where carriers become quantized and cannot be simply described by classical theory. For example, when a dielectric insulators' thickness is reduced to less than 10nm, carriers can easily tunnel out of the barrier and cause logic errors. New computing paradigms need to be explored if we want to keep increasing our computation power.

Quantum effects do not just pose an obstacle for computing, they also provide an opportunity for an entirely new and extraordinarily powerful computing paradigm. With quantum computing, the classical computing unit is replaced by qubits, where each qubit can simultaneously exist in a superposition of the 0 and the 1 state. This superposition increases the amount of information one computational unit can hold, and allows multiple qubits to effectively store and process multiple states simultaneously by quantum entanglement. A significant increase in the computational power can be achieved with a sufficient number of entangled qubits. For example, a common hypothetical scenario is solving a 2048 binary digit key using a classical computer and a quantum computer. A quantum computer with 2048 qubits can encode 2^{2048} different

key combinations all at once, where a classical computer can only consider one key combination at one time. This makes the theoretical speed of finding the correct key combination in a quantum computer 2^{2048} faster than a classical computer.

1.1.2 Quantum Computing vs Classical Computing

Although quantum computing and quantum information processing is very promising and, theoretically, very powerful, it is extremely challenging to implement in practice. Following the previous example, a 2048-qubit quantum computer might possess 2^{2048} different states at once, but the time it takes to extract the one correct combination from all the 2^{2048} combinations can be significant. Good quantum algorithms are required to process the quantum information accurately and achieve a speedup, and not every type of classical problem can be directly implemented in a quantum computer. Despite this limitation, the improvement in computational power that would be enabled by quantum computers is still extraordinary, if enough qubits can be employed by the hardware.

Figure 1.1 gives an explicit comparison between the classical algorithm and quantum algorithm[1] for the speed of factoring a product of two large prime numbers. The horizontal axis is the length of the number to be factored, which is the same as the number of qubits, and the vertical axis is the time needed. The solid black line indicates the amount of time required to factor a number using a classical algorithm with a 1GHz Opteron CPU. The black vertical dashed line is the recommended Rivest–Shamir–Adleman (RSA) public key length in 2007. It will take billions of years to factor a 2048 bit number using the classical algorithm. Even with the constant increasing classical computation power, the amount of time required is still astronomical.

The colored lines are different combinations of quantum computer logical clock speed for 1) a three-qubit operation called the Toffoli gate (1Hz and 1MHz), 2) methods of implementing the arithmetic portion of Shor's algorithm (BCDP, D, and F), and 3) quantum computer architectures (NTC and AC). [1] Without getting into much detail about each of these algorithms, it is clear that the time required to factor a 2048

bit number can be reduced to seconds, as indicated by the blue line. However, the speedup only occurs with enough qubits, and the threshold for speedup depends on both the algorithm implementation and hardware architectures. The overaching point is that: 1) the quantum algorithms are paramount if we want to solve problems that can not be solved using the classical computers and 2) building quantum computing hardware with thousands of qubits is essential to realizing a useful quantum computer. The advances enabled by pratical quantum computing will accelerate fields ranging from computation aided design, large molecule simulation related to drug delivery, to cracking a security passcode.
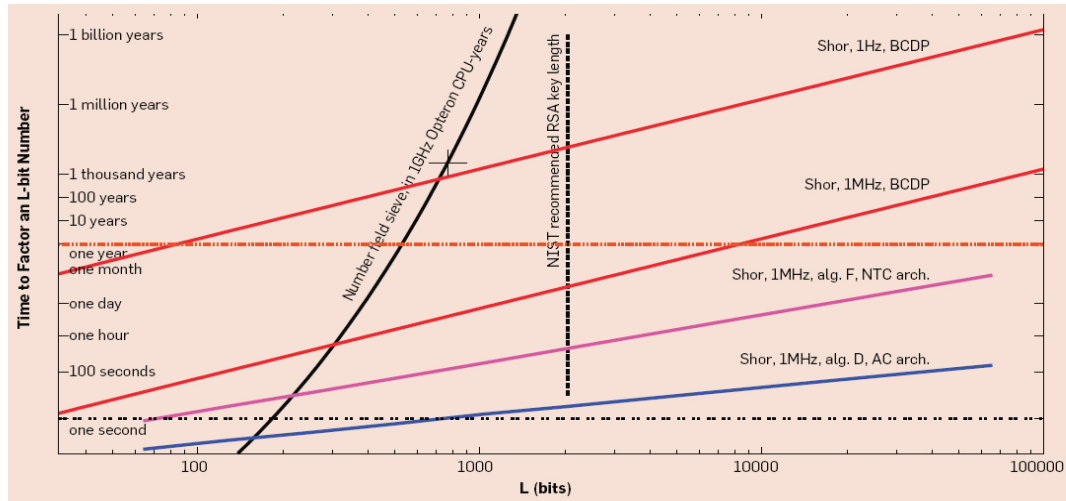
Figure 1.1: The computation time of factoring L-bit number. picture adapted from Van Meter, Rodney ; Horsman, Clare. " A blueprint for building a quantum computer." In: Communications of the ACM. 2013 ; Vol. 56, No. 10. pp. 84-93[1]

1.1.3 Quantum Logic Gates and Their Challenges

Many quantum computing models use the advantages of quantum mechanics. These models include gate quantum computing, one-way quantum computing, adiabatic quantum computing, and topological quantum computing. In this work, we will only introduce the gate quantum computing architecture and in order to motivate the

needs to find new materials platforms that can incorporate better and more scalable qubits.

Building a universal gate-model quantum computer requires two things: A) a two-level superposition system that represents two quantum states $|0\rangle$ and $|1\rangle$ and B) a set of universal gates that manipulate these two superposition quantum states. One example of a universal quantum gate is a combination of a Hadamard (H) gate, a phase rotation gate $R(cos^{-1}\frac{3}{5})$, and a controlled-NOT gate. The Hadamard gate operates on a single qubit and maps $|0\rangle$ to $\frac{1}{\sqrt{2}}(|0\rangle + |1\rangle)$ and $|1\rangle$ to $\frac{1}{\sqrt{2}}(|0\rangle - |1\rangle)$, creating a superposition of $|0\rangle$ and $|1\rangle$ such that the measurement outcome will have equal possibility of being one $|0\rangle$ or $|1\rangle$. The phase gate R operates with one qubit, leaving $|0\rangle$ unchanged and mapping $|1\rangle$ to $e^{i\phi}|1\rangle$, which changes the phase of the quantum state. The CNOT gate operates with two qubits, using the first qubit as the control and flipping the state of the second qubit if the control is $|1\rangle$[2]. Using a set of universal gates such as the one described here, all qubits can be manipulated independently and coupled together to execute an arbitrary quantum algorithm.

One of the biggest challenges in creating superposition states for quantum gate operations is decoherence. Decoherence means the loss of coherence in the quantum superposition state due to the non-perfect isolation between the state and its environment. The time that a superposition state can exist without collapsing to a classical states is the decoherence time (T1). A special kind of decoherence occurs when the orthogonal phase of the superposition state decays due to interactions with the environment. The time a superposition state maintains its phase is called the dephasing time (T2). These timescale set fundamental limits of time on how quickly quantum information must be manipulated and extracted before the information is lost permanently.

Because of the existence of decoherence, a quantum gate cannot be operated perfectly and indefinitely. The success rate of a gate operation (fidelity) defines the quality of the qubit and physical gate. The fidelity is a measurement of how robust the coherent superposition state is and also how identical each qubit is. Non-identical

qubits are often the number one cause of two-qubit gates operation failures. To achieve higher fidelity gates in general, we need to find material platforms that can provide a scalable path to identical qubits, improve the gate operation speed, and increase the decoherence time and dephasing time.

Another way to improve the fidelity of a qubit gate is to use error correction. While classical error correction uses redundancy and stores the information multiple times in multiple bits, quantum information cannot be copied due to the no-cloning theorem. However, it is possible to encode the information of one physical qubit in multiple highly-entangled physical qubits. The collection of these physical qubits can from a logical qubit that with error corrections, outperforms any single physical qubit. The requirement for building a logical qubit with error correction is high-fidelity physical qubit with gate error rate typically smaller than 10^{-5} to 10^{-6}[3], which is extremely demanding.

Several quantum error correction algorithms based on this concepts have been invented, including the Shor code[4] that uses 9 fully-entangled qubits, the CSS code[5][6] that uses 5 fully-entangled qubits, and more recently the Surface code[7]. The surface code, specifically, operates on a two-dimensional physical qubit array, uses the nearest-neighbor qubits as a stabilizer, and can achieve a physical qubit error tolerance of 1%, which is three orders of magnitude higher than what is typically required for other approaches such as the CSS code[8, 7]. Based on the 1% error rate, the number of physical qubits needed to form a surface code corrected logical qubit is estimated to be around 10^8. Although this number can be reduced with physical qubits with lower error rates (higher fidelity), the number of physical qubits needed to build a universal gate-model quantum computer and achieve a speed-up against classical computer is still very large.
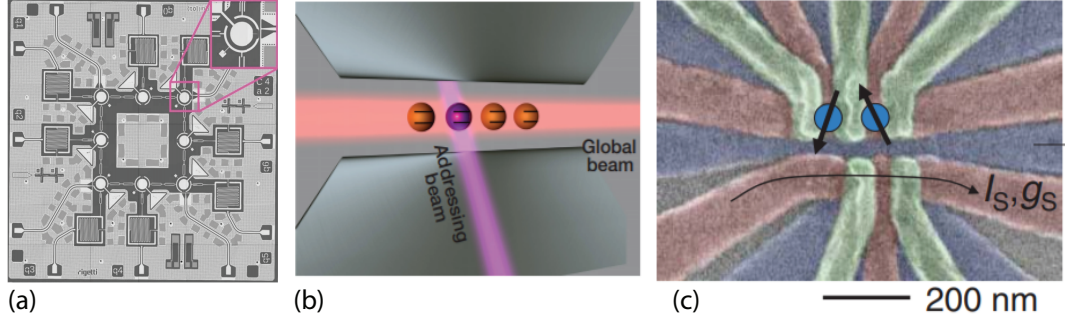
Figure 1.2: Examples of different quantum computing platforms. (a) a superconductor based 8 qubit system developped by Rigetti Computing.[9] Permission granted (CC BY-NC 4.0) (b) The schematic of a linear Paul trap experiment set-up, where a string of 40Ca+ ions is confined. The electronic states of each ion, depicted as horizontal lines, encode a spin $|\uparrow\rangle$ or $|\downarrow\rangle$. These states can be manipulated using laser beams. [10] (c) lithography defined two Si/SiGe QD spin qubit and their neighbouring qubit for charge sensor.[11]

1.2 Current Progress in Quantum Computing Research

1.2.1 Quantum Computing Platforms

Many different material platforms have been proposed to accommodate the gate quantum computing model. Several important material platforms include Josephson-junction-based superconducting platforms, trapped ion based quantum computers, silicon lithographically-defined QD platforms, photon-based quantum computers, and InAs quantum dot-based qubits, as shown in figure 1.2.

Superconductor-based quantum computers use Josephson-junctions as qubits, which can form a proper quantum 2-level system based on the junction charge, flux, or phase. Superconducting qubits' operates at hundreds of mK, and they are coupled and manipulated using microwave photon[12, 13, 14]. Figure 1.2 (a) shows a microscopy image of an adjacently-connected 8-qubit system on a 1cm*1cm die developed by Rigetti Computing using Josephson-junctions and microwave cavities.[9]

Trapped-ion based quantum computers use the highly identical atomic transitions of ion states as qubit states, and qubits are manipulated by either photons or phonons.[15, 14, 16] Figure 1.2 (b) shows a schematic of trapping Ca^+ ions with a linear

Comparison of state of the art metrics in leading QC platforms					
Platform	Superconductor	Trapped Ion	Si/SiGe Spin	Photonic	InAs QDs
Decoherence/ Dephasing	$30 \sim 60\mu s$ [12, 13, 14]	1 min [15]	$\sim 20\mu s$ [17, 11]	NA	1 ns [21, 22] / $(1 \sim 6\mu s)$ [23]
Gate operation time	$250 \sim 450$ ns [14]	$1 \sim 10\mu s$ [24, 15]	30 ns [17]	10 ms [19]	≤ 38 ps [25]
# of interacting qubits	$5 \sim 50$ [13, 12, 26]	5 [14] 53 [16]	$2-3$ [17, 11, 18]	4 [19]	$1 \sim 2$ [27]
Two qubit gate fidelity	99.4% [12]	$\geq$ 99.9% [24, 15]	78% for CNOT [11]	90% [20] 99.1% [19]	$\sim$ 80% in QDM [27]
Operation temperature	$\leq 25mK$ [14, 13, 12, 26]	$\leq 100K$ [24]	$\leq 150mK$ [28]	RT	$4K \sim 30K$ [29, 30]
Qubit Size	1 mm^2 [26, 12]	2.5mm^2 [24, 15]	63 nm^2 [28]	flying	$\sim$900 nm^2

Table 1.1: Comparison of state of the art metrics in leading QC platforms

Paul trap, initializing the ion state using a global laser beam while dressing individual ions using a different frequency laser beam.[10]

Si/SiGe based qubit uses lithographically-defined quantum dots to form electron/hole traps and manipulate the electron's spin state via tunneling using different gate voltages[17, 11, 18]. Figure1.2 (c) shows a color enhanced SEM image of a double Si/SiGe quantum dot qubit. The bottom quantum dot is used as a charge sensor and readout of the qubit state.

Besides these solid material platforms, another important quantum computing platform is the photon-based platform, which uses single photon sources and entangled photon pairs to generate flows of quantum information[19, 20]. Photonic qubit systems can be either constructed using free-space optics or integrated on-chip with photonic waveguides and couplers.

1.2.2 State-of-the-art Metrics in Various QC Platforms

We compile some of the state-of-the-art metrics in these leading quantum computing systems in Table 1.1. For instance, superconductor platform can now achieve tens of μs decoherence time and fast gate operation speed around hundreds of ns. The number of interacting qubits has increased dramatically in the past decades to around 50, and possibly more as I write this sentence. The best two-qubit gate fidelity is as high as 99.4%, reaching the limit of the error threshold of surface code. The drawback of this system is that it operates at an extremely low temperature, typically lower than 25mK, imposing significant extra cost and major engineering hurdles to scale-up.

Other systems also have their advantages and disadvantages. For example, trapped ion qubits have incredibly long decoherence times and close to unity two-qubit gate fidelity, but their estimated qubit size is on the scales of millimeters. Si/SiGe spin qubit systems have the smallest qubit sizes, which can be much more favorable for mass integration, but they also operate at extremely low temperature with a fidelity not high enough for fault-tolerant error correction. Photonic qubits, while having high gate fidelity and working at room temperature, often requires a free-space optical setup on the scale of square meters, naturally inhibiting its scalability.

1.2.3 Spin Qubit with InAs Quantum Dot and Quantum Dot Molecule

Without discrediting the significant advances many quantum computing platforms have achieved, it is safe to say that the need to find a better qubit system cannot be ignored. InAs quantum dot-based quantum computing systems use electrons or hole spins trapped in a single quantum dot or quantum dot molecule as the qubit, and these qubits are controlled using ultra-fast pulsed laser sources. This approach has the advantage of achieving ultra-fast gate operation speed down to several tens of picoseconds while coupling to photons for on-chip photonic mass integration. Moreover, the operation temperature for the InAs quantum dot system is usually around 4K to 30K. Although not as convenient as room temperature, this temperature range is easily accessible with modern closed-cycle cryostats and poses far fewer engineering

challenges than mK temperatures. Although the current gate fidelity is still low, and the interacting numbers of qubits are still limited, integrating a large number of qubits on-chip is possible with the sub-um size qubit unit and appropriate semiconductor fabrication techniques.

Both electron spins and hole spins are promising candidates for spin qubit using InAs QDs, as demonstrated by many groups.[25, 31, 32] However, hole spins are particularly interesting because of the lack of hyperfine interaction with the nuclei spin.[33, 34, 32] The relatively strong hyperfine interaction for electrons leads to coupling between the electron wavefunction and the random fluctuations of nuclear spins in the ensemble, leading to fast decoherence times around several ns.[21, 22] However, the p-type Bloch wavefunction for hole states results in zero wavefunction overlap with the nuclei spin and dramatically reduced decoherence. For instance, Warburton et al. have demonstrated a close to 1 millisecond spin relaxation time using hole spins in a QD under a weak magnetic field. [33] Moreover, hole states in InAs QDs and QDMs often have strong spin-orbit coupling interactions that lead to novel quantum device oppotunities such as non-destructive quantum state readout. [35] These features of hole spins make them an incredibly appealing qubit candidate.

InAs QDs and QDMs are also highly tunable by external electric and magnetic fields. For instance, vertical electric fields are widely used to tune the emission energies of QDs and QDMs [36, 37, 38, 39], which has the potential of enabling integration of large numbers of qubits into a scalable device. However, there is a lack of study on how electron or hole spins behave under an in-plane electric field. A systematic study of the spin states in QDs and QDMs under in-plane electric field could help reveal new spin physics, spark novel device applications, and complete the blueprint for InAs QD/QDM spin qubit.

1.3 Dissertation Content

In this dissertation, we will systematically explore how hole spin states behave in QDs and QDMs, subject to both vertical and in-plane electric field. We will also

design, fabricate, and characterize devices that can apply a 2-D electric field to a single QD or QDM. The content is structured as follows:

In Chapter 2, we will introduce the InAs QD/QDM system in detail. We will cover InAs QD/QDM's growth, optical properties with electric fields and magnetic fields, basic spin qubit structures with InAs QDs and QDMs, and their current challenges in fabrication and spin manipulation. We will introduce the need to apply lateral electric fields and 2-D electric fields, for full spin control of a QD/QDM system.

In Chapter 3, we will introduce the tight-binding simulation method for calculating single electron or hole spin states in a QDs. We will develop a hybrid simulation technique combining the tight-binding simulation with a finite matrix approximation. We will also introduce a visualization algorithm which reveals the spin texture of a hole state in a single QD.

In Chapter 4, we will use the hybrid simulation method to calculate hole spin states in a single QDs. We will uncover a novel hole spin polarization effect induced by a lateral electric field. We will explore this effect under various simulation conditions such as electric fields and magnetic fields orientations, QD geometries, QD compositions. We will further introduce the concept of spin texture and give explanations of the repolarization effect based on spin texture.

In Chapter 5, we will use the hybrid simulation method to calculate hole spin states in an InAs/GaAs QDM. We will discuss the effect of 2-D electric fields on Stark shifts, the formation of molecular states, and the hole spin mixing effect. We will also present the hole spin mixing effect with the spin texture visualization method.

In Chapter 6, we will introduce the 3-electrode device designs that can apply 2-D electric fields in the InAs QD/QDM system, validated by COMSOL simulation. We will discuss the importance of including the semiconductor module and examine the device parameters that might limit our device functionality.

In Chapter 7, we will introduce nanofabrication methods that are commonly used for III-V device manufacturing. We will focus on the fundamentals of e-beam lithography, inductively coupled plasma (ICP) etching, e-beam metal evaporation and

dielectric depositions using plasma enhanced chemical vapor deposition (PECVD) and atomic layer deposition (ALD).

In Chapter 8, we will describe the detailed fabrication process for the 3-electrode device as designed in chapter 6. We will illustrate our pattern layout, detailed recipes for each fabrication step, and discuss potential recipe improvements.

In Chapter 9, we will introduce optical characterization methods that are used to characterize InAs QDs. We will introduce the wafer imaging method that uses wafer scale photoluminescence (PL) to identify the density threshold of the QDs, and micro-photoluminescence (micro-PL) spectroscopy to characterize the spectral behavior of QDs under electric fields.

In Chapter 10, we will present the micro-PL data of the 3-electrode device, under different voltage geometries. We will show charging diagrams with different symmetries. We will use power-dependent and wavelength-dependent PL data to explain the physics behind the charging diagram. We will also show 2-D band-structures that correspond to charging a single QD using lateral electric fields, simulated using COMSOL.

In Chapter 11, we will summarize the main results of the spin properties, especially holes, in a QD or QDM, subjected to a lateral/2-D electric field, both in simulation and in experiment. We will discuss potential improvement in the device design, fabrication, and characterization of a QD's spectrum under 2-D electric fields. We will provide future research directions for simulations and full 3-D control over the electric field environment for a single QD or QDM.

Chapter 2

BACKGROUND

2.1 From Bulk Semiconductor to Quantum Dot

Semiconductors, such as Si, Ge, and GaAs, are materials that have electrical properties between insulators and metals. Their electrical properties are primarily defined by their bandgap energy, which is the energy required to promote a valence band electron to the conduction band, leaving behind a hole. In an intrinsic semiconductor, the Fermi-level lies at the center of the band-gap, making the semiconductor behave like an insulator. When the Fermi-level of a semiconductor moves close to the conduction band (valence band), the semiconductor will become more conductive because less energy is required to promote an electron (hole) to the conduction band (valence band). Besides versatile electric properties, semiconductors can also absorb or emit different energy photons depending on the bandgap of the material. We will specifically introduce the formation of a semiconductor quantum dot and its optical properties in this chapter.

Heterostructures formed by different semiconductors can have different band-alignment, which yields different electrical, and optical properties. For example, a quantum well can be formed by a type I band alignment between intrinsic GaAs and InAs, as shown in Figure 2.1. The lower band gap material InAs is sandwiched by the higher bandgap material GaAs, forming an InGaAs quantum well. The schematic of a 2-D potential well in Figure 2.1 shows confined energy states of electrons and holes in the z-direction. Electrons and holes that are trapped in the quantum well can recombine and emit a photon that corresponds to the energy difference of the confined states. Because quantum wells can only confine carriers in 1 dimension, electrons and

holes can still move freely in x-direction and y-direction, resulting in a continuous density of states.
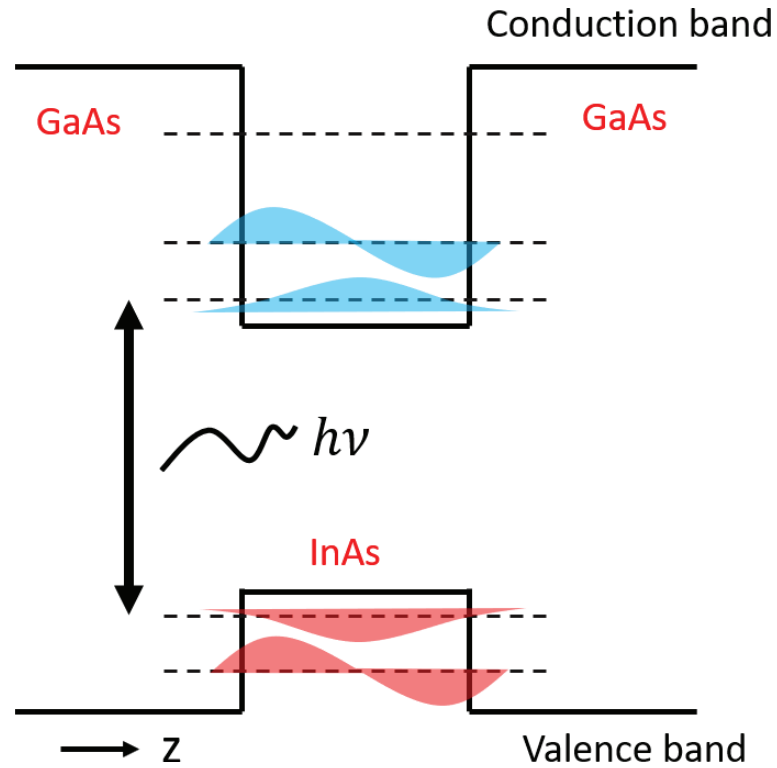
Figure 2.1: Schematic of a InAs/GaAs 2-D quantum potential well structure with type-I band alignment. Electrons and holes are tightly confined in the z direction but are free to travel in x and y direction. This 2-D potential well model can also help explain the discrete energy state in a QD. Electron (blue) and hole (red) wavefunction with strong overlap can recombine and emit/absorb a photon with the energy that's equal to the energy gap between the two states.

Expanding the potential confinement into all three dimensions leads to nanostructures that are called quantum dots (QDs). Electrons and holes inside a QD have discrete energy levels, giving them unique electrical and optical properties. Similar to a quantum well, QDs are often formed with two semiconductor materials that have different bandgap energies. The type of QD can vary based on different material compositions and fabrication techniques. Most commonly, there are three types of QDs: 1) Using lithography to define gates that are used to localize single electrons or holes

13

on a semicondutor surface, such as Al gates on GaAs, or SiGe gates on Si. People often refer to these QDs as lithographically-defined QDs or gated QDs. [40][41] 2) Using colloidal self-assembly to form nanoparticles that suspend in a solution. These are called colloidal QDs.[42, 43, 44, 45] 3) Use bottom-up growth technique such as molecular beam epitaxy (MBE) or MOCVD to form self-assembled quantum dots in a solid state system, such as InAs QDs. [46, 47, 48, 49, 50, 51] We will focus on self-assembled quantum dots composed of group III-V materials grown by MBE.

Many III-V QDs, such as InAs/GaAs QDs, are constructed from two direct bandgap materials. The strong wavefunction overlap between electron states and hole states in III-V QDs can lead to strong optical activities such as emission and absorption. The energy and material structure of InAs QDs can also be precisely deducted by characterizing the energy of the emitted or absorbed photon using spectroscopy. This is why InAs QDs with properly designed structure can be used in many applications that involve light. For example, combining InAs QD with an optical cavity and electrically pumping the nanostructure with carriers can generate strong optical emissions for lasing applications.[52, 53] Other applications include intermediate bandgap solar cells[54], light-emitting diodes[55], photoconductive field effect transistor designs[56], infrared photo detectors[57], and quantum information/computation applications.[58] Here, we will focus on the spin properties of a single hole carrier in a QD and its quantum computing applications.

2.1.1 The Formation of InAs/GaAs QD and QDM

InAs/GaAs QD are usually grown by molecular beam epitaxy(MBE). MBE has the ability to deposit materials such as Ga and As layer by layer down to the atomic level. When a single layer of InAs is deposited on GaAs, strain forms because of the lattice-constant mismatch between InAs and GaAs. During the strain relaxation process, InAs atoms can aggregate (self-assemble) and form island-shaped structures that are around several nanometers high, and several tens of nanometers wide. This island structure can later be capped with a much thicker layer GaAs to form a QD. The

bandgap mismatch between GaAs and InAs forms a 3-D potential well at the island, allowing the nanostructure to trap a single electron or hole. This growth method is called the Stranski-Krastanow (S-K) method. [46] A scanning electron microscopy (SEM) picture of a island shape InAs QD is shown in Figure 2.2 (a)[59]. A vertical Quantum Dot Molecule (QDMs) is grown by depositing a second thin layer of InAs several nanometers above the original QD layer. The second QD will tend to nucleate directly on top of the bottom dot, due to favorable strain conditions.[60] The GaAs between the two QD serves as a tunneling barrier for charges moving between the two QD. Figure 2.2 (b) shows a cross-section transmission electron microscopy (TEM) picture of a vertically stacked InAs QDM. [51]

(a)   (b)
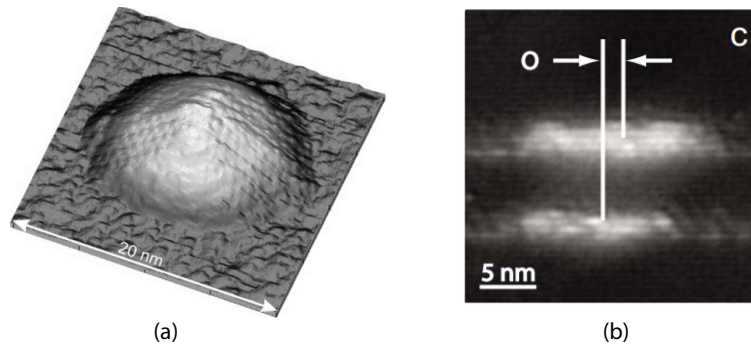
Figure 2.2: (a)H. Eisele, et al. demonstrated STM image of an uncapped InAs/GaAs QD. [59] (b)TEM image of a InAs/GaAs QDM with a slight geometric offset. [51]

One technique commonly used in InAs QD growth is cap-and-flush[61]. The cap-and-flush method caps the island-shaped QD with some GaAs (2-3nm) partially-covering the island but leaving the top exposed. The substrate is first heated to the InAs growth temperature so that Indium migrates from the QD to GaAs, and then slowly raised to the GaAs growth temperature to flush the exposed In away. The result is that the top part of the QD island can be removed, leaving a truncated QD shaped like a disk. This is why in Figure 2.2 (b) the two QDs cross-section view looks like a rectangle. Using cap-and-flush, the height of the QD can be precisely controlled,

15

decreasing the ground state photoluminescence (PL) emission wavelength from 1.3um to around 950nm by increasing quantum confinement.

The advantage of the Stranski-Krastanov growth is that the defects between InAs and GaAs interfaces are kept to minimum so that the optical properties of the QDs are excellent. The downside is that the location, size, shape, and density of QDs cannot be precisely controlled because of the self-assembly process. This means that every QD has a slightly different size and shape, which influences its energy structure and optical qualities[46]. The randomness of the QD locations also causes difficulties in device fabrication.

2.2 InAs QD and QDM Optical Properties

InAs QD/QDM grown by S-K method after cap-and-flush have a strong confinement in the growth direction, close to a square well. The confinement in the in-plane direction is usually not that strong, resulting in a parabolic potential well. Electrons and holes trapped in the potential well have strong wavefunction overlap in the growth direction and can emit light in the near infrared region. The excitation can be either from an above-bandgap photon source[62, 63], below-bandgap photon source (intermediate band excitation)[54] or electrical injection (electroluminescence)[53]. In my dissertation, we will mainly discuss above-bandgap excitation photoluminescence(PL) signatures of QD and QDMs for quantum computing/information applications.

Laser light with an energy higher than the GaAs bandgap can excite electrons in a QD from the valence band to the conduction band, leaving a hole behind. The combined states of excited electrons and holes are called excitons. Under low excitation power conditions, only the PL from the lowest unoccupied energy states can be observed, giving insights into the energy structure of the QD. Consequently, photoluminescence (PL) is one of the most convenient ways of studying an InAs QD/QDM. PL study of a QD usually requires cryogenic temperature lower than 80K, since nonradiative recombination is significant at a higher temperature. While ensemble QD

16

emission has a Gaussian linewidth of several tens meV, due to the random size difference of each QDs; the linewidth of a single QD's photoluminescence has a Lorentzian shape theoretically, and it can be significantly reduced (down to several μeV) under low excitation power and low-temperature condition. We will focus on a single QD PL in our discussion.

The PL from a single QD also has fine structure splittings on the μeV scale. In detail, PL emissions from a single QD consist of two distinguishable, radiative recombinations with distinct linear polarizations. This effect largely originates from the ellipticity of QD's shape in the in-plane direction, resulting in different optical dipole moments in different directions.[64, 65] This anisotropic exchange splitting is very important. Tuning the FSS to minimum can be useful for the generation of entangled photon pairs from QDs and increase the efficiency of coupling a single spin in a QD to photons. Successfully reducing the fine structure splittings in QDs can lead to high fidelity spin operations and single photon generations. [66, 67, 68]

It is also worth mentioning that single photon sources are crucial for photonic based quantum information technologies. InAs QDs has been reported to be able to generate single photons at a purity higher than 99.99%, based on two-photon excitation of the biexciton state [69]. InAs QDs also has been reported to achieve 99.5% indistinguishability using adiabatic rapid passage[63]. Using spontaneous coupled down conversion, QD can also generate entangled photon pairs, where the two photon's energy and momentum are coupled and can be used in quantum information applications[70]. Because utilizing all these properties in device applications are still challenging, studying the fundamental properties of QD using photoluminescence can improve QD engineering and inspire more accessible application ideas.

2.2.1 Photoluminescence of QD with Vertical Electric Fields

Single InAs QD can be used to confine a single electron or a single hole. The common strategy to charge a quantum dot with a single electron or hole is to use vertical (growth direction) electric field. Figure 2.3 shows a typical InAs QD device structure
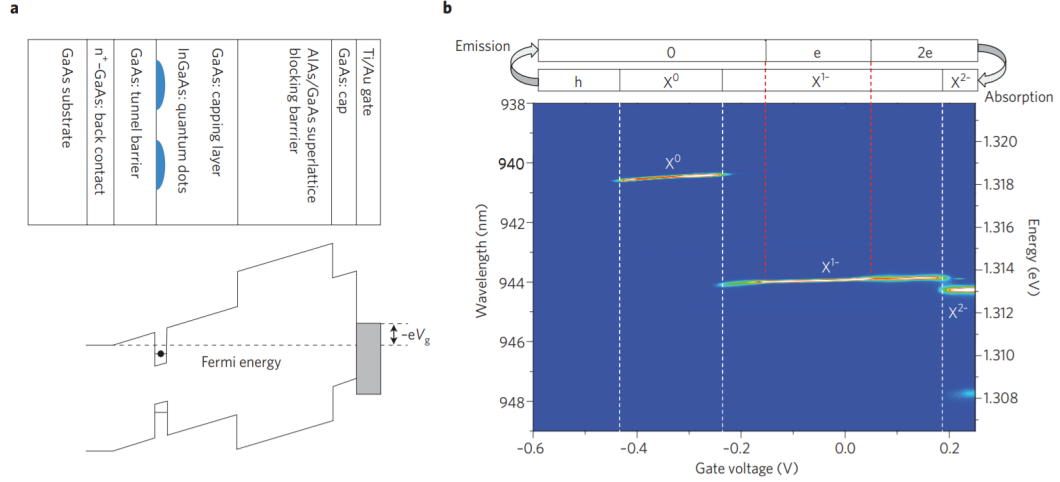
Figure 2.3: (a)A common vertical electric field QD device with a n-i-Schottky heterostructure. Graph below shows the band-alignment of a vertically gated InAs quantum dot. (b) A photoluminescence intensity graph with different gate voltage and photoluminescence wavelength(energy). The diagram above shows the charging sequence as the tuning of the gate voltage. Graphs come from review paper by Warburton, et al. [71]

and its PL as a function of different vertical electric fields. (picture from review article by Warburton)[71]. As shown in (a), the QD is grown on a GaAs substrate that has a n^+ back contact. A thin GaAs intrinsic barrier is grown between the QD and the n^+ contact as the tunneling barrier. Electrons can tunnel into the QD when the electron states' energy matches the Fermi level of the n^+ layer. A higher bandgap material such as AlAs/GaAs is used to form a blocking layer, preventing holes from tunneling in from the other side. Finally, a Schottky contact is formed on top of the QD to tune the electric field.

Figure 2.3 shows the photoluminescence intensity as a function of gate voltage. X^0, X^{1-}, X^{2-} represent the neutral exciton, the single electron charged exciton (negative Trion), and the doubly electron charged exciton respectively. These states occur consecutively as the gate voltage changes the band alignment of the structure and allows electrons to tunnel into the QD one at a time. The energy shift of the PL upon

18

charging is due to changing many-body interactions within the QD. The photoluminescence of a single charge state also shifts in wavelength as the gate voltage increases. This is due to the Stark shift that changes the band structure in the QD. This shift can be used to tune the two QDs into resonance if they have different energies. However, the tunability is very limited for single QD and is usually not enough to offset the inhomogeneity among the QDs.

2.2.2   PL from a QDM with Vertical Electric Fields
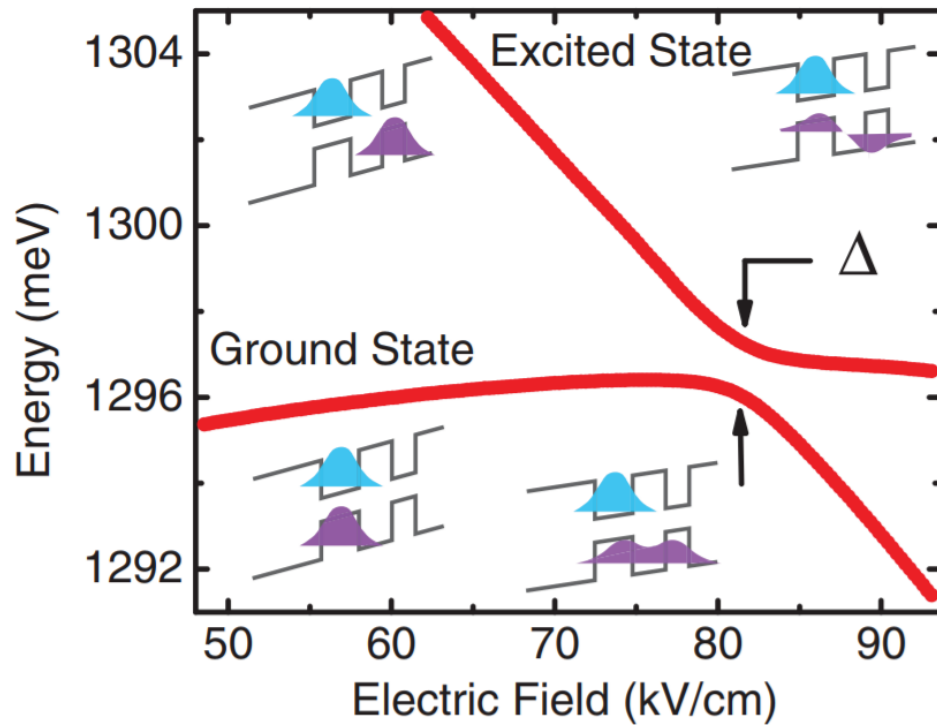
Figure 2.4: Photoluminescence of a quantum dot molecule and the formation of the anti-crossing molecular state of a neutral exciton. The wavefunction distribution of electron (blue) and hole (purple) is indicated along with the band diagram of the QDM. Anti-crossing forms around 80kV/cm, indicating coherent tunneling of hole state between the two QD and forming hybridized molecular state[72]

A QDM in a similarly gated device has a similar PL signature in that electrons

or holes can be injected into the QDM one at a time, forming neutral excitons and charged excitons. One major difference is that electrons or holes can now reside in either quantum dot (bottom or top), and different PL signatures can occur when they recombine from different dots. Figure 2.4 shows the PL signature of a neutral exciton in a QDM under external vertical electric field[72, 39]. The two QDs in the QDM have different truncation heights, which leads to different ground state energies for the two dots. The four insets in the graph show the band structure of a quantum dot molecule with different electron (blue) and hole (purple) wavefunction distributions. The left part of the bandstructure indicates the bottom dot and the right part indicates the top dot. Electrons and holes can recombine from either the same dot (direct transition), or from different QDs (indirect transition). Indirect transitions have significant larger tunability with electric field because of the increased charge dipole moment.

Another signature of QDMs happens when the energy levels of the two QDs are at resonance. As shown in the graph, when the electric field is around 80kV/cm, holes (purple wavefunction) can tunnel between the two QD and form molecular states. This is why there's an anti-crossing, instead of a crossing, at 80kV/cm when direct transitions state meets indirect transition state. It is very similar to the molecular orbitals hybridization phenomenon, thus the name quantum dot molecule.

It is also worth mentioning that similar molecular states can be observed with electron tunneling between the two QDs. In both cases, indirect transitions have lower PL intensities because the electron/hole wavefunction overlap is significantly reduced compared to the direct transition. Therefore, finding the right balance between tunability and good optical properties is key to many QDM optoelectronic applications.

2.2.3 Effect of Lateral Electric Fields

Numerous studies have been done on single QD systems with lateral (in-plane) electric fields. Just as for the vertical electric field, the lateral electric field also induces the Stark effect, changing the energy of the QD. While in theory similar to the vertical electric field, in reality the reported magnitude of the Stark shift induced by lateral

electric fields varies significantly from experiment to experiment. [73, 74, 75, 76] For instance, Gerardot et al. reported up to 1meV Stark shift in a single InAs QD using gate electrodes separated by 15um [73], while Kowalik et al. only observed 100 μeV Stark shift with gate electrodes separated by 2um. We should point out that the magnitude of the Stark shift strongly depends on the size, the geometry and the symmetry of the quantum dot and more studies are required to improve the design and device fabrication for QDs with a lateral electric field.

Besides Stark shift effects, the lateral electric field can also induce forbidden optical transitions and modify the linewidth of the quantum dot. Reimer et al. report that with the lateral electric field, electrons can recombine with holes from the p shell state instead of the s shell state.[74] Additionally, they report that the lateral electric field can help reduce the fine structure splitting of the QD emissions by 60%. Moreover, Moody et al. report that by applying a lateral electric field in a QD coupled with a waveguide structure, they can increase the coherence time from 1.4 to 2.7 ns. [77]

Despite the interest in lateral electric fields, little study has been done on how lateral electric field affects a single hole spin state in an InAs QD. Additionally, there are no experimental efforts in applying lateral electric fields to a single vertically-stacked QDM. Moreover, devices used to apply lateral electric field are often designed according to experience, but without systematic numerical simulations. [78] Considering all the reported effects of induced lateral electric field, there is significant opportunity for controlling a hole spin with 3-D electric field for quantum computing applications.

2.2.4 Effect of Magnetic Fields

2.2.4.1 Zeeman Effect

Zeeman effect refers to the splitting of spectral lines in the presence of a magnetic field. The splitting originates from the coupling between the magnetic field and the angular momentum and the spin angular momentum of the electron or hole. At zero magnetic field, electrons or holes in the s-shell of a QD with different spins will have

degenerate energy levels. The degeneracy will be lifted in the presence of a magnetic field B, with a splitting energy ΔE. In a simple form:

$$\Delta E = \mu_B g B \tag{2.1}$$

The factor g is the Lande g-Factor that is an intrinsic property of the carrier. In a QD, g is dependent on the carrier type (electron, hole, or exciton), magnetic field direction, and sometimes electric field. The magnetic field is commonly used to create an energy difference between the orthogonal spin states, i.e., a 2-level system, for spin manipulations.

2.2.4.2 Hyperfine Interactions

Hyperfine interactions refer to the coupling between the electron spin and the nuclear spin. Because the nuclear spins of III-V materials are not zero, electron spins in an InAs/GaAs quantum dot are subject to interactions with an ensemble of $10^4 - 10^6$ fluctuating nuclear spins. This means that electron spins are exposed to a magnetic field (Overhauser field) with random magnitude and direction. The result is a fast decoherence time usually in the range of several ns. [79] A common way of reducing the hyperfine interaction and improving the decoherence time is to apply a static magnetic field. Nuclear spins will line up with the direction of the external magnetic field, becoming less noisy.

Besides suppressing the hyperfine interaction magnetically, we can potentially eliminate the hyperfine interaction completely by using hole spin. Unlike electron spin wavefunctions, the natural p-like symmetry of the hole spin Bloch wavefunctions have nearly zero amplitude at the nuclear site. Thus the hyperfine interaction is kept at a minimum. We will later introduce how this effect can be used in hole spin manipulations in a single QD.

2.3 Spin Qubit using InAs/GaAs QD and QDM

2.3.1 Single QD Spin Qubit

A single QD has the ability to trap a single electron or single hole, providing an environment for single electron/hole spin manipulation. Previously we mentioned that magnetic fields are commonly used to break the degeneracy between different electron/hole spin states, creating a 2-level system for qubit applications. Moreover, because the optical emission energies of InAs QDs are in the NIR region, commercially available wavelength-tunable laser beams can be used to address a single spin state deterministically. Here, we will introduce how spins in a QD can be manipulated optically.

To start, we will use electron spin as an example. Figure 2.5 shows the electron spin operation in a QD with a magnetic field along the growth direction (z, also called Faraday geometry magnetic field), as reported by Warburton. In this illustration, solid arrows $|\uparrow\rangle$ and $|\downarrow\rangle$ represent electrons with spin up and down, and double arrows $|\Uparrow\rangle$ and $|\Downarrow\rangle$ represent holes. Because of the Zeeman splitting effect, different spin state exhibit different energy states, which leads to the slight energy mismatch between state $|\uparrow\rangle$ and $|\downarrow\rangle$.
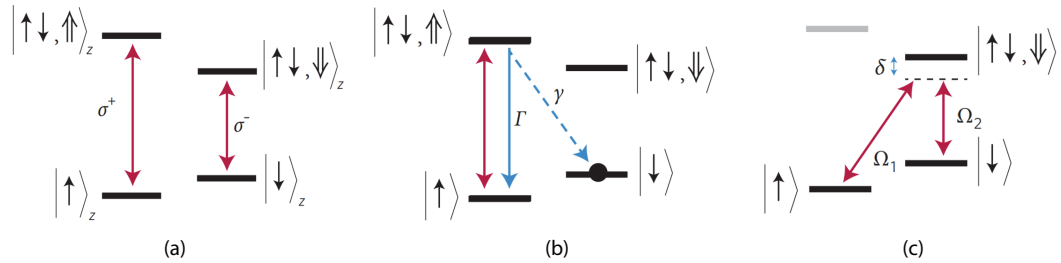
Figure 2.5: Single QD spin initialization and manipulation, using optical transitions. (a) optical transition rule in a vertical magnetic field. (b) single spin initialization using optical coherent trapping. (c) optical manipulation of spin state using Raman transitions. [71]

As shown in (a), due to optical transition rules and the Pauli exclusion principles, σ^+ photons can only drive transitions from the $\uparrow\rangle$ state to the $|\uparrow\downarrow,\Uparrow\rangle$ and vice

versa. The readout of the spin state can be performed by measuring the time-averaged absorption of the laser with the resonant energy and polarization corresponding to the QD's spin transition.

To initialize a spin state, we can use optical coherent trapping (OCT) as illustrated by (b). Transitions between state $| \uparrow \rangle$ and $| \uparrow \downarrow, \Uparrow \rangle$ are driven by a narrow bandwidth laser resonant with the transition energy. Spontaneous emission takes place at rate Γ from the vertical transition $| \uparrow \downarrow, \Uparrow \rangle \rightarrow | \uparrow \rangle$ and at rate γ from the diagonal transition $| \uparrow \downarrow, \Uparrow \rangle \rightarrow | \downarrow \rangle$. Provided the optical coupling is comparable to Γ, and γ is much greater than the spin relaxation rate, the electron is shelved by the diagonal spontaneous emission in the $| \downarrow \rangle$ state.

Stimulated Raman transitions are usually used to manipulate the electron spin state between $| \uparrow \rangle$ and $| \downarrow \rangle$, as shown in Figure 2.5 (c). Two pulsed lasers are used to address the spin state with an in-plane magnetic field (Voigt geometry). The two laser's energies are $\hbar\Omega_1$ and $\hbar\Omega_2$, and the difference between the two equals the splitting of the two ground states. Detuning between the two lasers leads to Rabi Oscillations that creates superposition states of $| \uparrow \rangle$ and $| \downarrow \rangle$. [71]

Similar spin manipulation strategies can be applied to hole spins in QDs. It is also worth mentioning that besides using an external magnetic field to create the 2-level system, Gerardot, et al.[33] reported coherent optical pumping of a single hole spin without the presence of the magnetic field. The electron-nuclei hyperfine interaction results in coupled excitons states with opposite electron spin polarization, creating a Λ system for spin pumping. The pumping of a single hole state will therefore solely depends on the circular polarization of the laser, instead of the laser wavelength.

2.3.2 QDM Hole Spin Qubit

Although there has been much success in single QD spin operations, the tunability of single QD's emission under electric fields are very limited. This is a problem because of the inhomogeneity of as-grown QDs and the importance of identical transition energies for scalable quantum computing devices. Indirect optical transitions in

QDMs have much larger tunability than direct optical transitions in QDs and QDMs. Using the indirect optical transitions for qubit applications can therefore ease the scalability challenge by individually tuning each QDM's emission energy to the target wavelength. When combined with the reduced hyperfine interaction described above, this makes holes confined in a QDM a promising qubit candidate. In this subsection, we will introduce an additional advantage for hole spins in QDMs as qubits, a phenomena known as hole spin mixing. We will explore how hole spin mixing and indirect transitions can be used as hole spin qubit in a QDM.[51, 35]

2.3.2.1   Hole Spin Mixing State in QDMs

When we apply a vertical direction (Faraday geometry) magnetic field in a vertically-stacked quantum dot molecule, a single hole spin state could have 4 different configurations: hole spin up in the bottom dot, hole spin down in the bottom dot, hole spin up in the top dot, hole spin down in the top dot. In the scenario where there are only heavy holes, the four different configurations could be represented by matrices with double arrows respectively as: $(\Uparrow, 0)$, $(\Downarrow, 0)$, $(0, \Uparrow)$, $(0, \Downarrow)$. Previously we discussed that under a growth direction electric field, electron and holes could tunnel between the two QDs and forms molecular states. These states can be represented as: $(\Uparrow, 0) \pm (0, \Uparrow)$ and $(\Downarrow, 0) \pm (0, \Downarrow)$. In this case, holes maintain their spin projection while tunneling between the two QDs.

An interesting spin effect happens in asymmetric QDMs, i.e. those that have a lateral offset in which top quantum dot is not symmetrically centered on the bottom quantum dot. In other words, the internal geometrical symmetry of the QDM along the growth direction is broken. An example is shown in Figure 2.2 (b). This symmetry breaking, in conjunction with spin-orbit interactions, leads to the mixing between the heavy hole states and the light-hole states. As a result, hole spin states that are coherent superpositions of holes with orthogonal spin orientiations can form. Mathematically, such states can be expressed as: $(\Uparrow, 0) \pm (0, \Downarrow)$ and $(\Downarrow, 0) \pm (0, \Uparrow)$. Conceptually, these states are equivalent to a spin flip during tunneling.
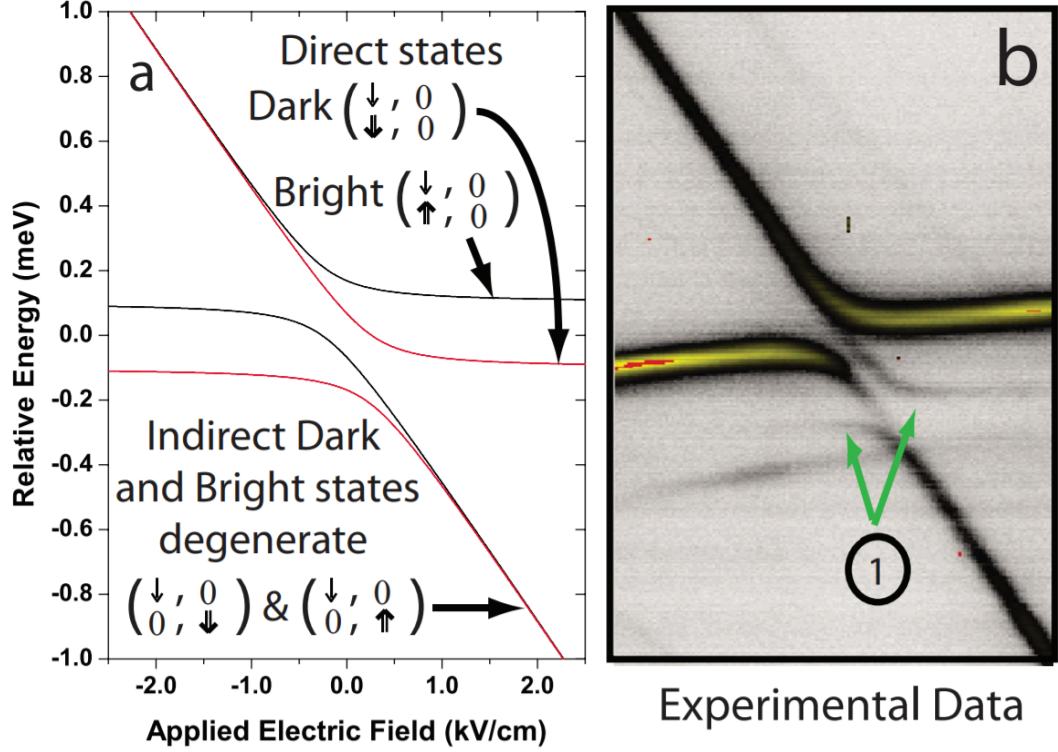
Figure 2.6: Hole spin mixing effect explained with theoretical calculations and photoluminescence. (a) Energy levels of bright and dark state calculated at 0 magnetic field. (b) Photoluminescence of a single QDM at 0 magnetic field showing the dark state. Picture adapted from [51]

One of the direct experimental observations of the hole spin mixing effect is the existence of dark states photoluminescence. According to the optical transition rules, electrons and holes will only recombine and emit a photon if their total spin angular momentum equals ±1. Electron spins $\downarrow$ and hole spins $\Downarrow$ won't emit a photon because their combined angular momentum is ±2. These exciton states are called dark states and normally they cannot be observed optically. The observation of photoluminescence from such a state implies that this state must be mixed with a bright state, which in turn implies hole spin mixing must be present. Indeed, this effect has been reported by Doty et al. in a photoluminescence experiment under 0 magnetic field and Faraday geometry magnetic field.

Figure 2.6 (a) shows the bright and dark transitions of a single QDM at 0

magnetic field. In this case, we only consider the scenario where the electron is located at the bottom dot and the molecular state can form with the hole tunneling between the two dots. The two bright states $\left(\begin{smallmatrix}\downarrow,0\\0,\Uparrow\end{smallmatrix}\right)$ and $\left(\begin{smallmatrix}\downarrow,0\\\Uparrow,0\end{smallmatrix}\right)$ are drawn in black line and the two dark states $\left(\begin{smallmatrix}\downarrow,0\\0,\Downarrow\end{smallmatrix}\right)$ and $\left(\begin{smallmatrix}\downarrow,0\\\Downarrow,0\end{smallmatrix}\right)$ are drawn in red line. The energy split between the two direct transitions are due to the symmetric electron-hole exchange interaction. This interaction is proportional to the wavefunction overlap between electrons and holes, and thus is suppressed to negligibly small in indirect transitions.

Figure 2.6 (b) shows the experimental photoluminescence data from a QDM with a 4 nm lateral offset, as a function of the applied vertical electric field. As pointed out by the two green arrows, a weak anti-crossing is observed in PL, indicating forbidden optical transitions as shown in Figure 2.6. Doty et al. also observed a more complicated spin mixing effect under a 6T vertical magnetic field, further proving the existence of the hole spin mixing states. The physical origin of the hole spin mixing effect is explained using a Luttinger spinor calculation, where heavy hole states with angular momentum of $\pm\frac{3}{2}$ mix with light hole states with angular momentum $\pm\frac{1}{2}$. The hole spin mixing state could recombine with electrons and emit a photon, making the dark states visible. [51, 35] The calculation also shows that the hole spin mixing state only exist in a QDM that has a lateral offset.

2.3.2.2 Qubit Based on Hole Spin Mixing

Based on the hole spin mixing effect and indirect transitions in QDMs, Doty, et al. have developed single hole spin qubit operation strategies using an optical manipulation concept.[35] As shown in Figure 2.7, hole spins can be initialized, controlled and read out under a vertical magnetic field. The left side of the 2 by 2 grid represent the bottom dot and the right side represent the top dot. The strategy uses two hole spin states $\left(\begin{smallmatrix}0,0\\0,\Downarrow\end{smallmatrix}\right)$ and $\left(\begin{smallmatrix}0,0\\0,\Uparrow\end{smallmatrix}\right)$ as our qubit 2-level basis. The strategy also uses the highly tunable indirect transition states to mediate the interactions between these two basis, giving it great potential for scale-up.
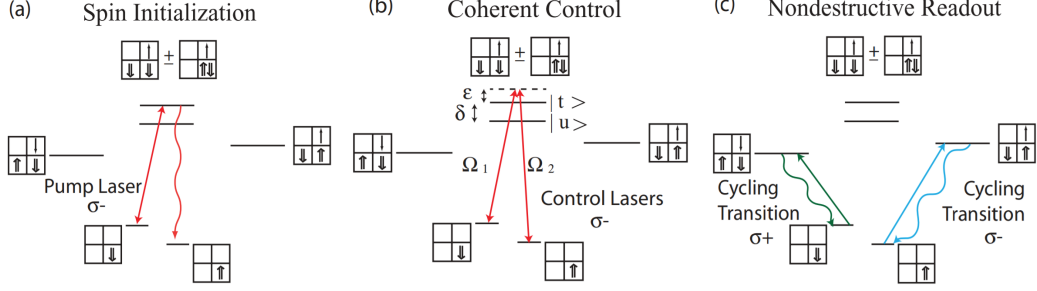
Figure 2.7: QDM spin initialization and manipulation, using hole spin mixing with a Voigt geometry magnetic field. (a) optical pumping from spin down state to spin up state using a $\sigma-$ circular polarized pump laser. (b) Raman transition using $\sigma-$ polarized laser with two detuned frequencies $\Omega 1$ and $\Omega 2$. (c) Spin readout using cycling transitions with $\sigma+$ polarized laser. [80]

To initialize a hole spin in the top dot, we can use optical coherent trapping with a $\sigma-$ polarization pump laser as shown in Figure 2.7 (a). The laser can continuously pump hole spin state $\left(\begin{smallmatrix}0,0\\0,\Downarrow\end{smallmatrix}\right)$ to state $\left(\begin{smallmatrix}0,0\\0,\Uparrow\end{smallmatrix}\right)$ by using the hole spin mixing exciton state $\left(\begin{smallmatrix}0,\uparrow\\\Downarrow,\Downarrow\end{smallmatrix}\right) \pm \left(\begin{smallmatrix}0,\uparrow\\0,\Uparrow\Downarrow\end{smallmatrix}\right)$. Using two laser beams with frequencies Ω_1 and Ω_2 slightly detuned from the hole spin mixing state, we can create Rabi oscillation that rotates the spin projection of a single hole state. This is shown in (b).

More interestingly, the readout of the spin state can be "Non-destructive" if we use cycling indirect optical transitions between the hole spin state $\left(\begin{smallmatrix}0,0\\0,\Downarrow\end{smallmatrix}\right)$ and $\left(\begin{smallmatrix}0,\downarrow\\\Uparrow,\Downarrow\end{smallmatrix}\right)$. Since the only allowed transition is the electron and the $\Uparrow$ hole state, the hole state $\Downarrow$ can be preserved during optical readout.

2.3.3 Coupling QD/QDM Qubit to Photons

Coupling between QD or QDM spin states and photons are usually mediated by photonic nanostructures patterned on-chip, such as a micro-pillar[82], a micro-disk[83], a slab waveguide[84], or a photonic crystal cavity.[85, 81, 86, 29] Specifically, photonic crystal cavities, as shown in Figure 2.8, creates photonic bandgaps and traps photons in their defects. It allows strong couplings between a photon and an exciton, creating an entangled quantum state that can be used to mediate QD qubit to qubit interactions.
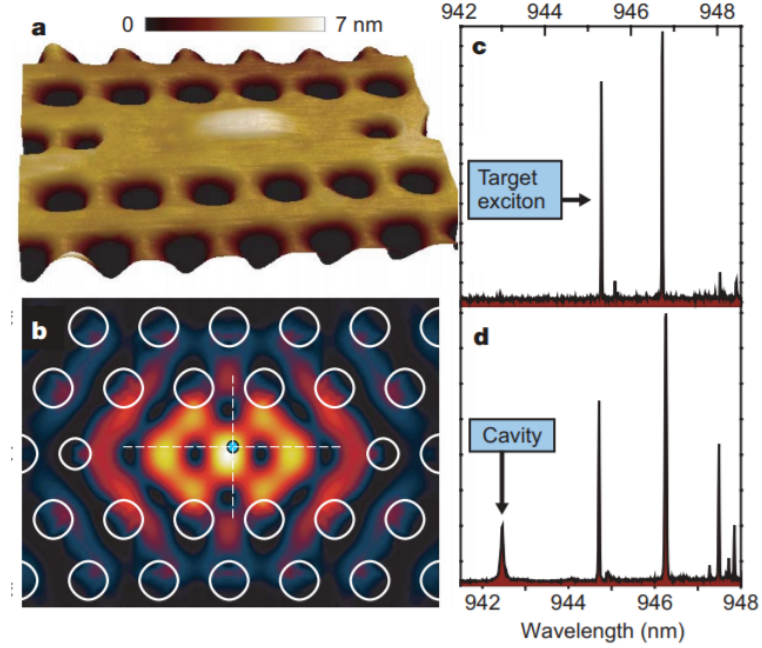
Figure 2.8: A single InAs QD deterministically coupled to a photonic cavity. a, AFM topography of a QD and photonic cavity [81]

In the example presented by Hennessy et al.[81], a quantum dot is pre-selected using atomic force microscopy (AFM), and periodic holes are patterned around the QD to create a photonic cavity, as shown in Figure 2.8(a). Figure 2.8(b) shows the electric field intensity of the photonic crystal cavity mode, while the QD is located at the cavity field maximum (white) to ensure optimal coupling. The size and periodicity of the holes are designed to create a cavity resonance wavelength similar to the QD's emission. Figure 2.8(c) and (d) shows the PL spectrum from the same QD before and after the cavity fabrication, with the cavity mode located 2nm apart from the target exciton wavelength.

Achieving exact overlap between the as-grown QD emission energy and the as-fabricated photonic crystal resonance is extremely challenging. Because the QD emission is much more sensitive to temperature than the cavity mode, many have demonstrated strong coupling between a QD and the cavity mode by temperature detuning. [87, 81] Additionally, people have demonstrated using a vertical electric field

tuning to couple a QD's emissions with the cavity mode, by embedding the photonic crystal in a vertical diode structure.[86, 29] While on-chip strong coupling between individual quantum dot is yet to be realized, coupling QD emissions using free-space optics has shown great potential in photon based qubit applications.[88]

2.3.4 Challenges Facing QD and QDM

2.3.4.1 Growth and Fabrication

As mentioned before, MBE grown QD are usually randomly located. This alone can cause significant trouble in single QD characterization. Currently, people use different techniques to study the behavior of QD/QDM without in-situ grown QD. For example, the density of the QD can be modulated by stopping the wafer rotation during the InAs QD layer deposition. The no-rotation growth creates a QD density gradient in the wafer that can be later characterized optically. People also use microscopy methods such as AFM to pre-locate a good QD before device fabrication.[81, 89] Without these approaches, hundreds of apertures need to be fabricated to isolate a single QD optically. There are also many ways to grow QD in-situ. For instance, the substrate can be patterned with pits or pyramids to form favorable strain conditions for QD to nucleate.[90, 91, 92, 93] These techniques, however, all result in QDs with poor optical quality (low quantum yield, high inhomogeneity) and can not be used for reliable qubit applications.

Besides the random nucleation sites in growth, QDs are also grown with different density, sizes, and shapes. The result is that every QD/QDM has its own emission wavelength and polarization, and thus couples to photons of different energies. To the best of our knowledge, the smallest ensemble QD PL linewidth is around 20meV. [46, 61]. This puts a lot of constraints on how a QD qubit device can be fabricated. For example, in order to build a QD/QDM-based 2-qubit system, photonic structures such as cavities and waveguides must be fabricated to mediate the interactions between two QDs. Each QD's energy has to match precisely to the energy of the cavity in order to generate strong interactions between the QD's state and cavity state, forming cavity

QED. In order to tune the energy of the cavity with just one QD, external tuning mechanisms such as electric field or temperature have to be introduced to the qubit system, thus increasing the noise and the decoherence.[94, 29] Additionally, coupling between two or more QD/QDM on-chip requires all QDs to be located at the photonic cavity's field maximum as designed. The precision required is usually on the scale of 10 nm, which is impossible without the precise location control during the growth stage and reliable alignment procedures across the entire fabrication.

The self-assembled growth also inhibits our ability to control the symmetry of the QDM. As mentioned before, the hole spin mixing effect has only been observed in QDMs that have a geometric offset. Additionally, the magnitude of hole spin mixing also depends on the magnitude of the geometric offset, which eventually leads to different gate fidelity and decoherence. Because the growth of a self-assembled quantum dot is a mostly random process, deterministically controling the geometric offset of two stacked QD during growth is awfully challenging. Therefore external controls of the hole spin mixing effect have to be invented to make this material a more viable qubit candidate.

2.3.4.2 Decoherence

Decoherence is the main antagonist of all qubit systems, including spins in InAs QDs. One of the main sources of decoherence is the hyperfine interaction. As we mentioned before, electron spins have strong hyperfine interactions, which usually leads to fast spin relaxation time in the scales of nanoseconds. Optical techniques such as spin echo, which uses laser light to manipulate the phase of the electron spin, can help increase the decoherence time to μs. However, combining the spin echo with qubit gate operations is still challenging. [23] While hole spins wavefunctions have the symmetry of atomic p orbitals, the hyperfine interaction can only be completely removed with pure-Ising like heavy hole states. This puts many challenges on light-hole heavy-hole interaction-based qubit applications.

Another major source of decoherence is local fluctuations of the electric field. Fluctuating electric field can be generated from nearby defects or other QDs, resulting in Stark shift to the emission energy of the exciton. While it does not directly interact with the spin states, such inhomogeneous linewidth broadening caused by electric field fluctuation could result in variations of coupling strength between an exciton and a photon, reducing the spin operation fidelity.[95]

2.3.4.3 How 2-D Electric Field Can Help

Studying QD and QDM in a 2-D electric field system by itself helps us understand the physics behind experimental phenomena such as the magnitude of the Stark shift and hole spin mixing. It is also possible that new physics can be observed when QDs and QDMs are subject to a 2-D electric field. Such new phenomena may also find applications in quantum computing. Here are three specific examples of how 2-D electric fields in a QD can help:

1. In previous examples, we've seen the effect of a 1-D electric field on a QD system. The vertical electric field can be used to charge a QD with a single electron or hole, shifting energy levels by the Stark effect. Lateral electric fields can induce Stark shifts and change spin fine-structure splitting effects in QD. One of the drawbacks of applying the vertical electric field is that the tunability from the Stark shift is significantly hindered by charging because the charged state can "disappear" when an extra carrier is injected into the QD. Lateral electric fields, on the other hand, are usually induced by Schottky contact gate electrodes that do not have a doped Fermi-sea on the side to charge a single QD. Combining these two functions and applying vertical and lateral electric fields simultaneously could achieve individual tuning between charge injections and energy level tunning by Stark shifts.

2. 2-D electric field can help change the local electric field environment, and thus fine tune the fine-structure splitting. While using the vertical electric field alone suppresses field fluctuations in one direction, defects in material growth could generate

field fluctuation in the lateral direction. Recently, Zeeshan et al. have proposed a strategy of applying quadrupole electric field on a single QD to suppress the local electric field and eliminate the spin fine-structure splitting. It could increase the decoherence time significantly. [96]
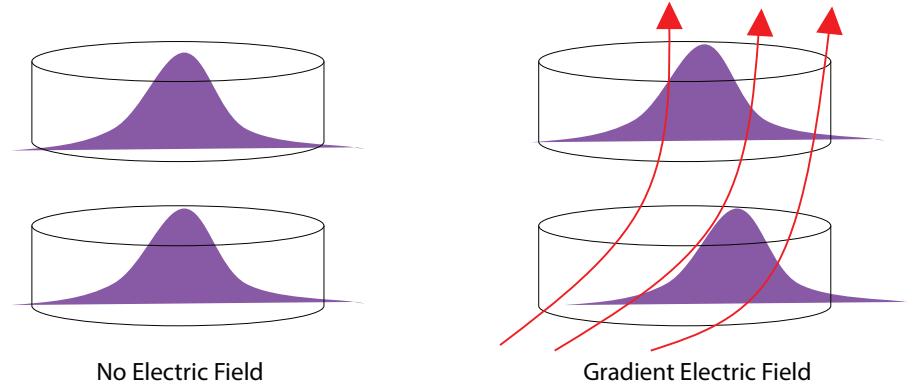
Figure 2.9: Quantum Dot Molecule and hole wavefunction (purple) under a gradient electric field. Schematics not to scale.

3. 2-D electric fields can prompt new spin physics and spin engineering applications. For example, there's a lack of study on how hole spins behave in a single QD with Voigt geometry magnetic field and lateral electric field. A thorough understanding of the hole spin in this scenario is necessary for quantum device engineering. Another example would be inducing and controlling the hole spin mixing effect, which only exists in asymmetric QDMs. To control the asymmetry of the growth is extremely difficult, but 2-D electric fields might be able to mediate this problem. As shown in figure 2.9, if we apply an electric field that has a gradient in the growth direction, we could asymmetrically push the wavefunction of holes in a QDM, thus creating an artificial lateral offset.

In this dissertation, we will focus on how lateral electric fields induce new spin physics in a vertical field charged single QD, and how 2-D electric fields help shape the wavefunction of a QDM. We will then explore different device design parameters that help us apply the 2-D electric field to a single QD/QDM nanostructure. We will discuss how this device is fabricated and characterized. Finally, we will present our

closest effort yet to deterministically control a single spin in an InAs using a 2-D electric field.

Chapter 3

SIMULATION METHOD

3.1 Tight-binding Theory

Tight-binding simulation is a semi-empirical model that's commonly used in simulating bulk and finite scale semiconductors. The premise of tight-binding is the assumption that electron and hole wavefunctions can be described as a set of atomic orbitals. We consider inter-orbital and nearest neighbour atom-atom interactions, as a matter of convenience, which gives us a good description with the band structures. A simple s band 1-D tight-binding model can be found in the appendix.

3.1.1 Tight-binding Model for III-V Quantum Dot

In the tight-binding model we used, the basis states for each atom includes an s orbital, three p orbitals and an excited s^* orbital[97, 98, 99, 36, 78]. The on-site orbital energies and nearest neighbour coupling parameters for InAs and GaAs are adjusted to reproduce the InAs and GaAs bulk band structures.[97] Roughly more than half a million atoms are used to construct the InAs/GaAs QD and QDM structure.

The strain due to the the lattice mismatch is also accounted for by using the valence-force-field method to find the relaxed lattice configurations with the minimum strain energy.[100, 98, 99, 36] The tight-binding parameters are re-scaled using Harrison scaling laws to account for deviations of the local atomic lattice from the bulk configurations with bulk bond lengths and bond angles.[101]

The tight-binding model also needs to accommodate different electric field and magnetic field conditions. A static applied electric field can be included in the tight-binding approach via a potential energy shift of the atomic orbital energies. A constant, static magnetic field $\vec{B}$ is incorporated, in a gauge-invariant form, in the tight-binding

approach via a Peierls transformation[102] that includes the magnetic vector potential via a phase shift of the tight-binding nearest-neighbor hopping parameters. Spin-orbit effects are included atomistically.[103, 104]. The interaction with atomic orbital angular momentum and spin is also included with an additional Zeeman energy term, $\mu_B(\vec{L}_{at} + 2\vec{S}) \cdot \vec{B}$ where $\vec{L}_{at}$ is the atomic orbital angular momentum and $\vec{S}$ is the spin.

III-V semiconductors are piezoelectric materials where local charge is produced proportionally by local strain. This local charge creates an additional local electric field and corresponding potential. We use the approach employed by Zielinski[105, 106] to include the potential for the piezoelectric field as an additional shift of the on-site orbital energies.

We will also refer to the full tight-binding simulation as atomistic calculation for the rest of our discussion.

3.2 Finite Matrix Method

3.2.1 Theory

The atomistic tight-binding simulation provides the eigenstates energies and wavefunctions of a semiconductor model with high precision. However, exploring the parameter space of different electric fields or magnetic fields could be very time-consuming, because each data point at a specific field condition requires a full calculation that takes into account of all the energy states' interactions. A simple bias-energy map that varies with 20 different electric field conditions could take days. Therefore, it's not practical to use tight-binding simulation alone for exploring a QD's spin state under electric fields with different directions, magnitudes, and gradients.

To solve this problem, we construct a finite matrix calculation method based on the Hamiltonian calculated from a tight-binding simulation. Specifically, we use this method to calculate a single hole spin state in a QD or QDM with electric fields. We first perform a tight-binding calculation at a chosen electric field $\vec{F}_0$ to define a basis of exact eigenstates for this field. These basis states contain the information of each

eigenstate's energy and wavefunction. We then choose a finite number of basis states that's energetically close to the ground hole-state to construct the following matrix:

$$H' = \begin{bmatrix} E_1^{(0)} + V_{11} & V_{12} & \ldots & V_{1n} \\ V_{21} & E_2^{(0)} + V_{22} & \ldots & V_{2n} \\ \vdots & \vdots & \ddots & \vdots \\ V_{n1} & V_{n2} & \ldots & E_n^{(0)} + V_{nn} \end{bmatrix} \tag{3.1}$$

The n states, with energies $E_n^{(0)}$ are computed by the atomistic method. The wavefunction that describes each state (ϕ_{r_i}) consists of amplitudes for every electron orbital (s, p and $s*$) at each atomic site $\vec{r}$. At each atomic site α, the external potential value $V_r = (\vec{F}_\alpha - \vec{F}_{0,\alpha}) \cdot \vec{r}$ is the product of the external electric field ($\vec{F}$) and the position of each atom ($\vec{r}$). The interaction terms (V_{ij}) are constructed from the integration of two wavefunctions over the electric potential, $V_{ij} = \sum_r \langle \phi_{r_i} | V_r | \phi_{r_j} \rangle$. In practice, the potetial V changes very slowly over the lattice, so that it becomes a constant at each atomic site. The calculation can then be rewritten as $V_{ij} = \sum_r V_r \langle \phi_{r_i} | \phi_{r_j} \rangle$. Using this basis, we then calculate the eigenenergy for an arbitrary field condition $\vec{F}$ by diagonalizing the matrix Hamiltonian.

The diagonalization of the finite Hamiltonian H that contains less than 100 element per dimension usually takes less than a second. On the other hand, diagonalizing the Hamiltonian in the tight-binding simulation which contains 500,000 times 500,000 elements will take hours. This is why the finite Hamiltonian method is much faster compared to the tight-binding simulation, for the purpose of exploring many Hamiltonian under different electric fields. We also further accelerate our calculation by first calculating the states interacting terms at each atomic site $\langle \phi_{r_i} | V_r | \phi_{r_j} \rangle$ and store it as a matrix, then reuse the matrix for different electric field conditions.

We refer to this method as finite matrix Hamiltonian method, to distinguish it from the full tight-binding calculation.

3.2.2 Calculating the Spin

As we mentioned before, the spin effects are included atomistically in the tight-binding simulation[103, 104]. Specifically, each orbital's wavefunction amplitude is divided into two parts that represent the spin up and the spin down in the growth (z) direction. In formula, we could write the specific hole (electron) states' (j) wavefunction as:

$$\Psi_j = \psi_{\vec{r}_j,\alpha_j,s_j}|\vec{r}_j,\alpha_j,s_j\rangle \tag{3.2}$$

Where $|\vec{r}_j,\alpha_j,s_j\rangle$ is the wavefunction basis at the location $\vec{r}$, with the orbital $\alpha = s,p,d,s^*$ and the z component spin s. To convert the z component spin to x and y components, we use Pauli matrices:

$$\sigma_z = \begin{bmatrix} 1 & 0 \\ 0 & -1 \end{bmatrix} \sigma_x = \begin{bmatrix} 0 & 1 \\ 1 & 0 \end{bmatrix} \sigma_y = \begin{bmatrix} 0 & \text{-i} \\ \text{i} & 0 \end{bmatrix} \tag{3.3}$$

The interactions between the z component spin ↑ and ↓ and Pauli matrices can be summarized as:

$$\langle\uparrow|\sigma_z|\uparrow\rangle = 1, \langle\downarrow|\sigma_z|\downarrow\rangle = -1$$

$$\langle\downarrow|\sigma_x|\uparrow\rangle = 1, \langle\uparrow|\sigma_x|\downarrow\rangle = 1$$

$$\langle\downarrow|\sigma_y|\uparrow\rangle = i, \langle\uparrow|\sigma_y|\downarrow\rangle = -i$$

Consider a single hole state j, the eignevalue of the spin under the new 1/2 spin basis k=x,y,z is

$$\langle\Psi|S_k|\Psi\rangle = \frac{\hbar}{2} \sum_{\vec{r},\alpha,\hat{S},\hat{S}'} \psi^*_{\vec{r},\alpha,\hat{S},\hat{S}'} \langle\hat{S}|\sigma_k|\hat{S}'\rangle \psi_{\vec{r},\alpha,\hat{S},\hat{S}'} \tag{3.4}$$

Where $\hat{S}$ and $\hat{S}'$ represent different spin directions ↑ or ↓.

We also find it interesting when we dissect a single hole spin wavefunction and spin amplitude into different locations in the quantum dot. Instead of treating each hole energy state as a envelope wavefunction across the quantum dot, we could analyze the spin and amplitude wavefunction from each atomic site by calculating them

individually instead of summarizing everything. We will cover the details in the next section.

3.3 Accuracy Test and Results

Linear perturbation theory tells us that the major factors that limit the accuracy of the perturbation results are: 1) the orders of perturbation involved, 2) the number of interacting states included, 3) the magnitude of the perturbation itself. We choose this finite matrix Hamiltonian method which includes all orders of perturbation, because we are unable to use the 2nd order perturbation theory or even the 3rd order perturbation theory to generate high accuracy results that agree well with the tight-binding theory.

That being said, the accuracy of the finite matrix method compared to the full tight-binding results still strongly depends on the number of states included in the matrix. We perform convergence tests using different number of states in a QDM simulation with different external electric fields. We calculate the discrepancies among different state's energy levels, Zeeman splitting magnitude and spin, with different QD and QDM models. For example: Figure 3.1 shows the energy level errors when calculated with different number of eigenstates included in the finite matrix, from a minimum of 16 states to 28 states. The 12 cases represent the energy from different hole states (1st being the ground state) and the lateral electric field condition from $Ex = 5kV/cm$ to $Ex = 50kV/cm$. In all cases, including more than 24 states could reduce the overall error down to 8%. Moreover, the smaller the electric field, the smaller the error as compared to tight-binding model.

Another example is shown in Fig 3.2. In this case, we calculated the spin component (Sx, Sy, Sz) errors in a AlAs/GaAs Dome shaped QD with a magnetic field B(110)=1T and different lateral electric fields. The finite matrix contains either 20 hole states or 56 states (36 hole states and 20 electron states). The differences between the two cases is obvious at large lateral electric fields: the 20-state finite matrix has more than 10% error starting at 120kV/cm, while 56-state finite matrix keeps the spin error below 10% even at 200kV/cm.
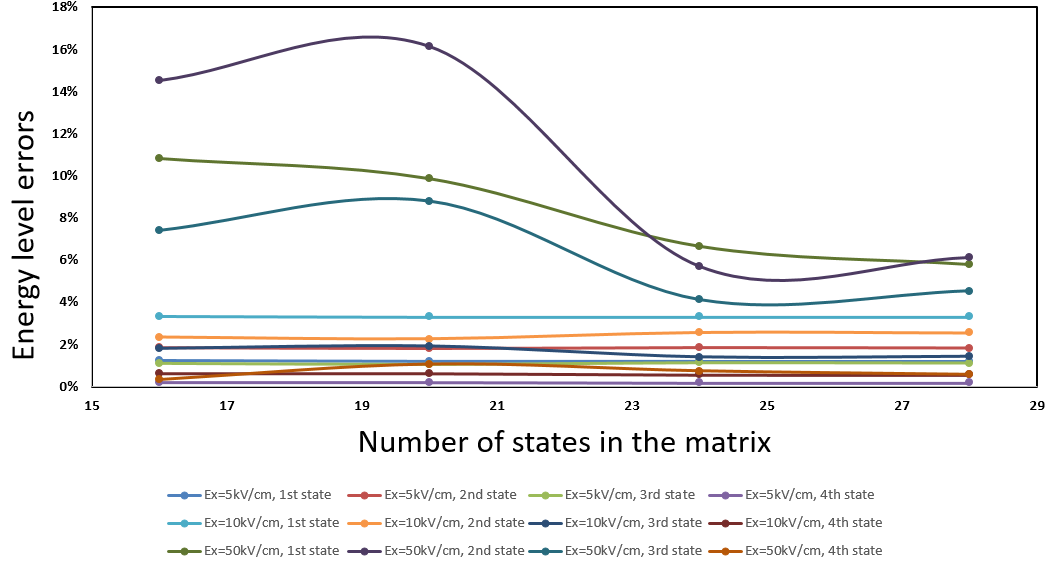
Figure 3.1: Energy level error in symmetric QDM without piezo-electric effect
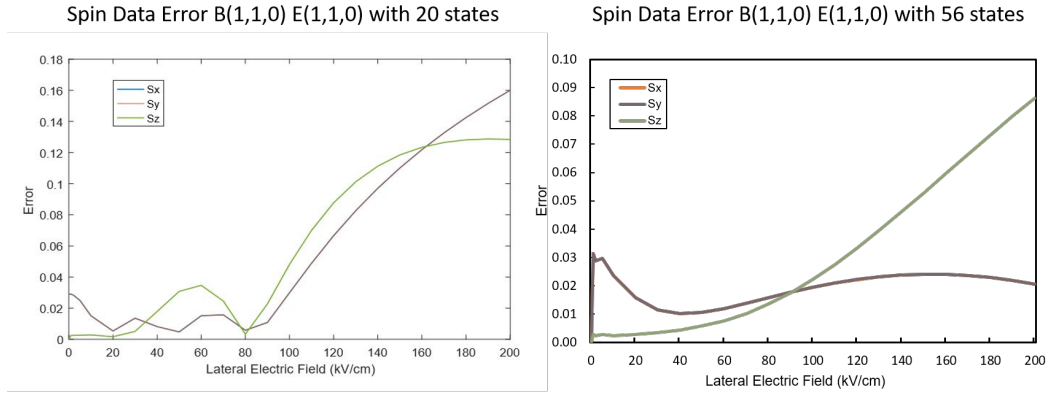
Figure 3.2: Spin error in a single AlAs/GaAs quantum dot with B(110) E(110) symmetry

While increasing the number of states in the finite matrix increases the accuracy, it also increases the calculation time significantly. In this work, in order to balance between the calculation accuracy and calculation speed, we will include a minimum of 44 states for the single QD calculations (unless stated otherwise) and a minimum of 24 states for the QDM calculations.

3.4 Spin Texture Visualization

In this section, we will go over the details of visualizing hole spin texture in a quantum dot or quantum dot molecule.

The traditional interpretation of a single electron or hole in a semiconductor is the effective-mass model which uses envelope wavefunctions to describe the amplitude along with a net spin. This interpretation needs to be improved, because hole states in a 3-D confined semiconductor nanostructure have strong spin orbit coupling effects that are usually hard to explain using an envelope wavefunction. In our discussion, we developed a computation method that interprets a single hole state wavefunction as the integration of amplitude and spin-projection contributions from different atomic sites. This method allows us to visualize the transformation of the spin with different electric fields, as well as the spin orientation from each atomic site that forms the net spin. It is extremely useful in terms of explaining hole spin mixing effects that often occurs in a QD/QDM system.

The method to visualize the spin texture of a hole in a QD or QDM, which contains more than half a million atomic sites, can be summarized as follows:

1) In order to directly visualize the spin texture in a 2-D graph, we need to reduce the amount of spin information. We first calculate the spin amplitude of a given atomistic location r, by the finite matrix method described above. We then integrate the (x,y,z) spin of all atoms in the QD/QDM along z axis, generating the spin information in the (x,y) plane. To make each spin diagram readable, we reduce the numbers of atomic sites in the (x,y) plane by combining the cation site and anion site, and then condensing them by a 3*3 lattice grid. The result is a reduced number of spin contributions from half of a million atoms to roughly 500 atomic sites, which represent the spin information around their location in the (x,y) plane. In the single QD simulation, the (x,y) plane is particularly interesting to analyze because both the electric and magnetic field lies in this plane. In the QDM cases, we will summarize all the spin component to two (x,y) planes, relative to each QD, so that the spin behavior in each QD in the QDM is analyzed separately.

2) We present the condensed spin contributions in the x-y plane with 3-D arrow plot. To properly illustrate the spin property without distorting the underlying physics, we unified the scale of all three axis and plot arrows individually and proportionally based on their atomistic locations and spin components. We modified the 3D arrow plot developed by Shawn Arseneau[107] to form each individual arrow, where the length and direction of each arrow represent the magnitude and direction of the spin contribution, respectively. The code to calculate wavefunctions and generate spin texture graphs using finite matrix approach can be found in the appendix.
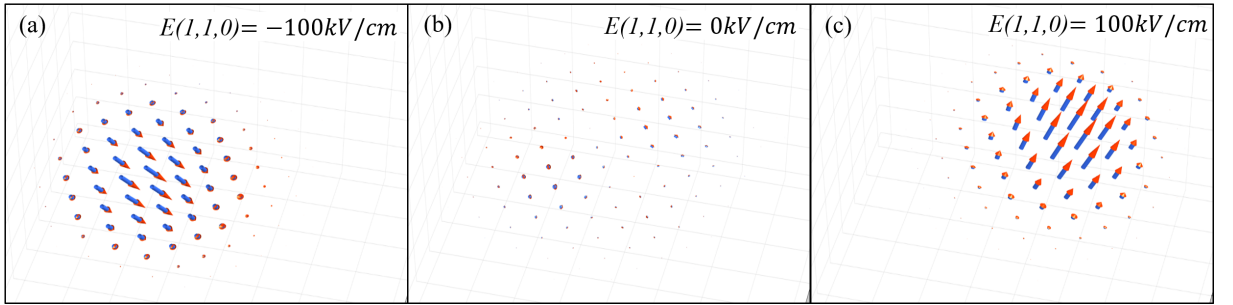
Figure 3.3: Spin texture in single AlAs/GaAs QDs with different electric field[108]

An example is shown in Figure 3.3. We calculate a single AlAs/GaAs QD with a Voigt geometry 1T magnetic field that's pointing in the (1,1,0) direction. Each arrow represents the spin amplitude and direction around its atomistic location, relative to the (x,y) plane. When the electric field $E(1,1,0) = -100kV/cm$, which points opposite to the magnetic field direction, most spin components point in the negative z direction, while centered around the (-1,1,0) side of the QD. The exact opposite is shown when $E(1,1,0) = 100kV/cm$, where most spin components point in the positive z direction. At $E = 0kV/cm$, however, the net spin is too small so that the lengths of the arrows are hard to resolve. We will use this visualization tool to explain hole spin effects in QDs and QDMs in the following chapters.

Chapter 4

HOLE STATE IN A SINGLE QD

In this chapter, we will discuss the hole spin properties of a single QD under both in-plane magnetic fields and electric fields. We will start with a relatively simple GaAs/AlAs model, and examine the hole spin properties including Stark shifts, wave-function distributions, and polarizations. We will then examine the hole spin with different parameters, such as the geometry and composition of the QD, the magnetic field orientation, and the electric field orientation. We will also use the spin texture visualization method to explain the physical origins of the hole spin properties.

4.1   Dome-shaped AlGaAs QD

We first simulate an GaAs/AlAs QD that has a dome shape. The geometry of the QD model is shown in Figure 4.1.
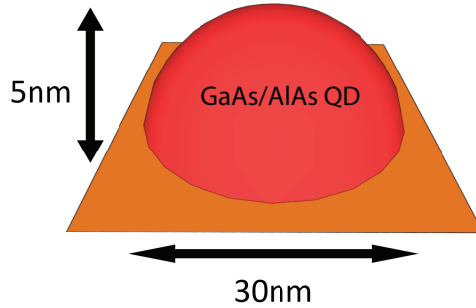
Figure 4.1: Single GaAs dome-shaped QD embedded in AlAs

The model consists of a semi-spherical GaAs QD embedded in an AlAs matrix. The dome height is 5nm, and the diameter is 30nm. While such a QD does not

actually exist and cannot be grown by the Stranski-Krastanov method, this theoretical model eliminates any strain effect caused by the lattice mismatch between different materials. To lift the degeneracy of different spin states, we computationally apply a 1T magnetic field in the in-plane direction (Voigt geometry). We include the 44 lowest-energy hole spin states and 30 electron states in the finite matrix for all the following calculations. In the following sections, We analyze the hole spin states under varying electric field conditions, through many aspects such as Stark shift, spin polarization, and wavefunction distribution.

4.1.1 Stark Shift
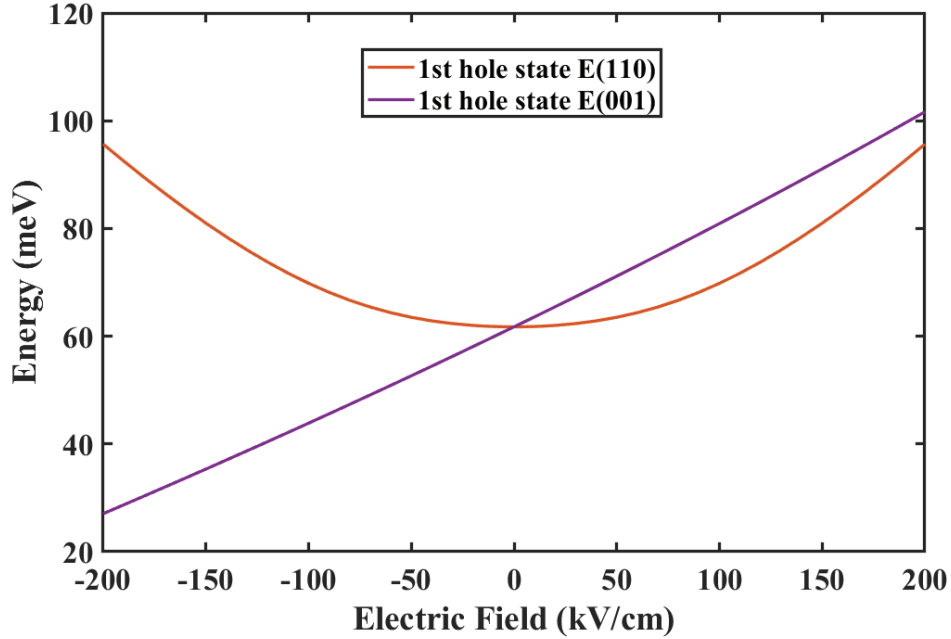
Figure 4.2: Lowest hole spin state stark shift under different electric field. B(110) = 1T

The Stark shifts of the lowest hole spin state under different electric fields are shown in Figure 4.2. When the electric field is along the (001) crystal direction, the Stark shift of the ground hole spin state resembles a straight line, indicated by the purple line. When the electric field is along the (110) direction, parallel to the wetting

layer, the Stark shift is a parabolic function of the external electric field, indicated by the orange line. This difference originates in the symmetry of the QD. Because the QD model is symmetric in the in-plane direction, the first order perturbation from the external electric field goes to zero due to symmetry, giving the Stark shift the parabolic shape. On the other hand, the QD is not symmetric along the (001) direction, making the first order perturbation the dominant factor in the Stark shift, therefore the straight line.

4.1.2 Spin
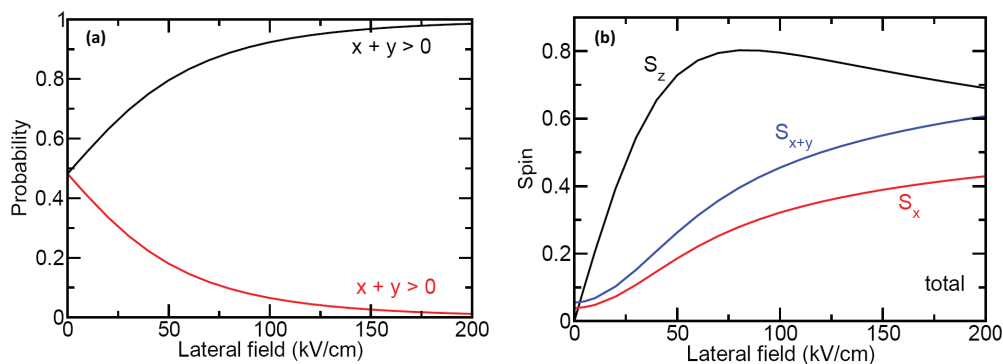
Figure 4.3: Ground hole spin state under in-plane electric field E(110), parallel to the magnetic field. (a) the probability of ground hole spin state at the $x + y > 0$ region (black) and $x + y < 0$ region (red). (b) the Spin polarization in x, x+y, z direction with the increase of lateral electric field E(110).

The lateral electric field can have a surprising effect on spin polarization, as shown in Figure 4.3. We apply up to 200kV/cm electric field parallel to the (110) magnetic field direction, pushing the wavefunction of hole spin states towards the $x + y > 0$ side of the QD, as shown in Figure 4.3(a). At 200kV/cm, the occupancy probability of the hole wavefunction in the $x + y > 0$ region becomes more than 98%. The spin polarization also changes with the movement of the wavefunction: the normalized Sx, Sx+y, and Sz components of the hole spin start around 0 at 0 lateral

electric field and gradually increase with the lateral electric field. Specifically, the Sz component peaks at 60kV/cm and maintains a highly polarized value (higher than 0.7) up to 200kV/cm.

The large Sz spin polarization is surprising because both the electric field and magnetic field are in the in-plane direction, perpendicular to the z axis. Our hypothesis is that the spin polarization in the z direction comes from the symmetry of the relationship between the magnetic field and the QD itself. In other words, we hypothesize that different regions of the QD contribute Sz up and Sz down components to the net spin projection. When the wavefunction is well centered in the QD, these contributions are equal and the net spin polarization along the z axis is zero. When the lateral electric field displaces the hole spin wavefunction, the opposing contributions are no longer equal in magnitude and a net spin polarization appears. To validate this theory, we will explore this effect with various electric field orientations, magnetic field directions, and different QD models.

4.1.2.1 Spin with B(110) and E(110)

Figure 4.4 shows the magnified spin texture of a GaAs/AlAs QD under a B(110)=1T Voigt geometry magnetic field, with 0 external electric fields. We use 3-D arrows to represent the spin components in the (x,y) plane and we magnify the absolute value of the spin uniformly without distorting the relative spin magnitude in the graph, as described in Chapter 3. We can tell from the direction of the arrow-plot that: 1) most arrows in the $x + y < 0$ region have a negative z component and most arrows in the $x + y > 0$ region have a positive z component; 2) Judging from the length of the arrows, the magnitude of the out-of-plane spin components in the (+x,+y) direction and in the (-x,-y) direction are equal. This is why the net spin in out-of-plane direction at E=0 is 0. This texture under the magnetic field B(110)=1T defines the spin polarization when the hole wavefunction is pushed to either $x + y > 0$ or $x + y < 0$ side of the QD.
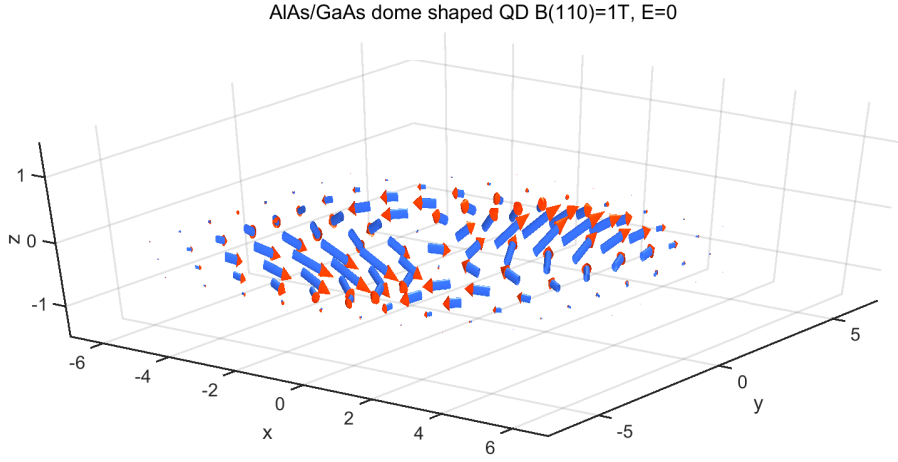
Figure 4.4: Magnified spin texture from a single GaAs/AlAs QD with B(110)=1T, E=0kV/cm

Figure 4.5 shows the spin polarization of the ground hole state as a function of lateral electric field in the GaAs/AlAs semi-spherical QD model with a 1T magnetic field in the (110) direction. The results correlate well with the hypothesis proposed previously, that the electric field pushes the wavefunction towards the edge of the quantum dot and the spin components in that direction get magnified. When the electric field is along the direction of the magnetic field, as shown in Figure 4.5(a), the net z-spin becomes positive as the wavefunction being pushed to the (+x, +y) direction by the (110) electric field. The net z-spin reverses its direction at 0 electric field, and becomes negative when the wavefunction being pushed to the (-x, -y) direction by the (-1-10) electric field. This spin polarization direction follows the spin texture shown in Figure 4.4. On the other hand, as shown in Figure 4.5(b), electric fields in the (-110) direction or (1-10) direction do not polarize the hole spin in the z-direction because of the equal and opposite contribution of z spin component from the $x + y > 0$ and $x + y < 0$ sides of the QD.

47
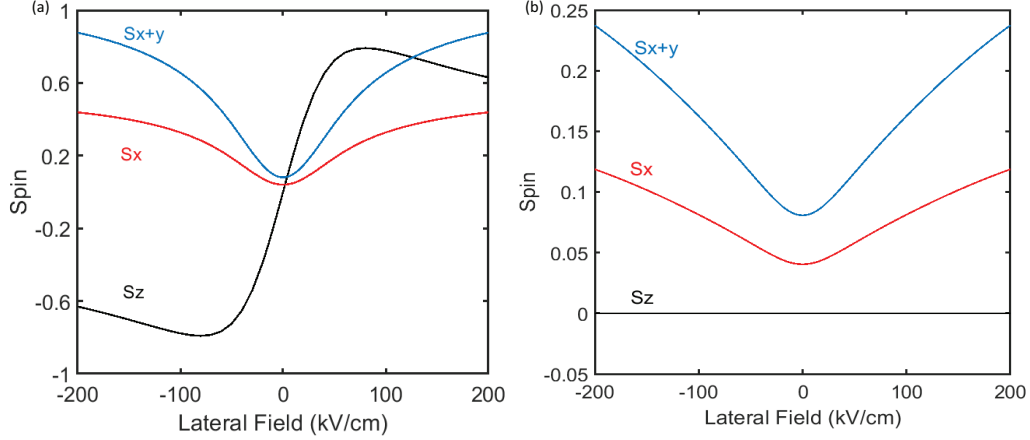
Figure 4.5: Spin component with B(110)=1T under different electric field (a) Lateral electric field (110) along the magnetic field direction. (b) Lateral electric field perpendicular (-110) to the magnetic field direction.

The spin texture also explains the spin in the x and x+y direction. At 0 electric field, most Sx and Sx+y spin components in the $(x > 0, y > 0)$ region and the $(x < 0, y < 0)$ region are positive, and some Sx and Sx+y spin components in the $(x > 0, y < 0)$ and the $(x < 0, y > 0)$ region are negative. Increasing the electric field in the (110) direction magnifies the positive Sx and Sx+y components by pushing the wavefunction towards either the $x + y > 0$ or $x + y < 0$ region. The Sx+y can be polarized to nearly 1 under ± 200kV/cm (110) lateral electric field, as shown in Figure 4.5(a). The (-110) lateral electric field, although increases both Sx and Sx+y net spin, does not polarize the spin as much as the (110) electric field, as shown in Figure 4.5(b). This is likely due to the negative Sx and Sx+y contribution from the $(x > 0, y < 0)$ and the $(x < 0, y > 0)$ region.

4.1.2.2 Spin with B(-110) E(-110) and E(110)

To determine whether the magnetic field plays a role in the spin texture symmetry, we repeat the calculation of single hole states in the GaAs/AlAs QD model with a magnetic field in the (-110) direction. Figure 4.6 shows the ground hole state spin texture of this model in the (x,y) plane with 0 electric fields. The spin-texture

magnitude is re-scaled to improve the visibility of the effect. Although the out-of-plane component of the spin is not obvious, it is not hard to tell that the spin texture is, in this case, analogous to the B(110) case rotated by 90 degrees counter clockwise. This indicates that the spin texture symmetry is dependent on the magnetic field direction.
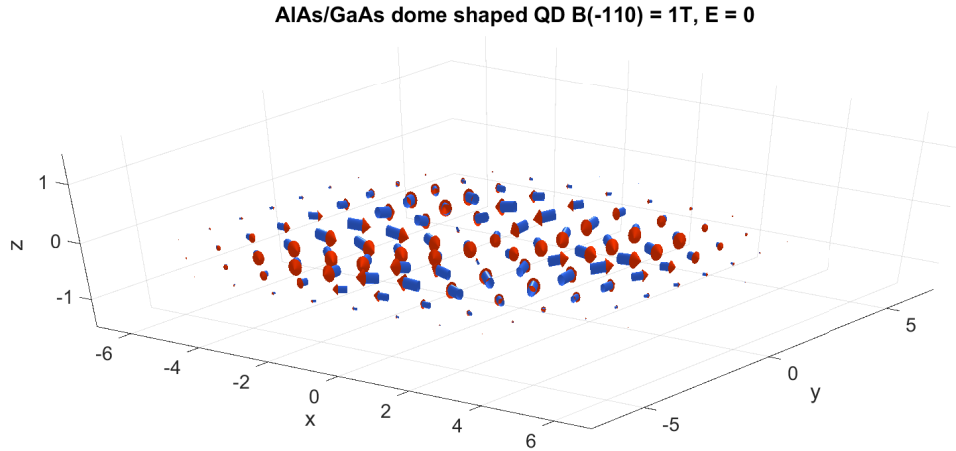
Figure 4.6: Spin texture with B(-110) = 1T , 0 electric field

Figure 4.7 shows the net spin of the hole ground state as a function of lateral electric field under the same (-110) magnetic field. When the electric field is along the magnetic field direction (-110) as shown in the left figure, Sz quickly increases from 0 to close to 0.8 at a moderate electrical field magnitude. Sz changes its polarization when the electric field is in the opposite direction to the magnetic field, dropping to -0.8 when E=-25kV/cm. The Sz spin component remains unchanged when the electric field is along the (110) direction, as shown in Figure 4.7(b). The Sx and Sx-y net spin decrease with increasing lateral electric fields, regardless of the electric field's polarization. And similar to the case with the (110) direction magnetic field, the magnitude of the Sx and Sx-y spin polarization with the (110) lateral electric field (Figure 4.7(b)) is much smaller compared to one with the (-110) lateral electric field (Figure 4.7(a)) .

49

The above result establish that the out-of-plane spin component Sz is strongly tunable when an in-plane magnetic field and parallel electric field are applied. The direction of the polarization depends on the sign of $\vec{B} \cdot \vec{E}$. The in-plane spin components can be magnified by an in-plane electric field either parallel or orthogonal to the magnetic field direction. The polarization of the in-plane net spin follows the direction of the magnetic field.
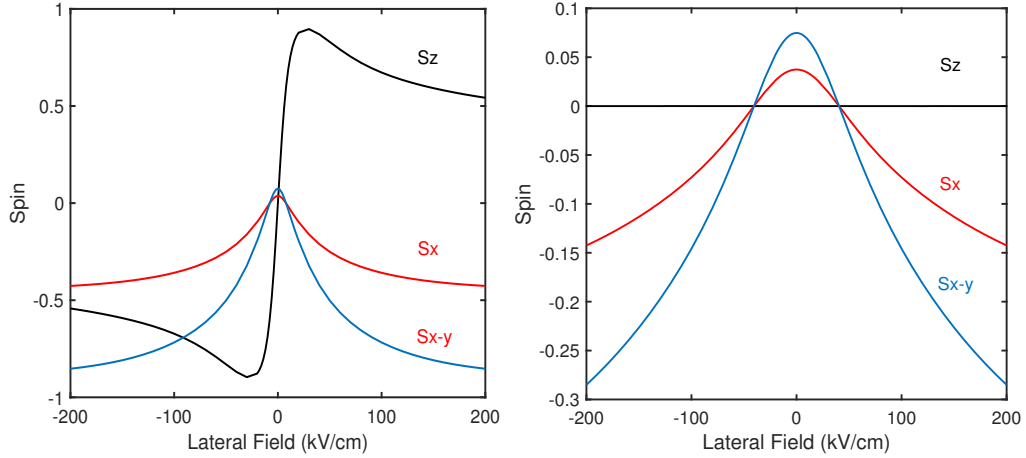
Figure 4.7: Spin polarization with B(-110) = 1T, as a function of (-110) lateral electric field (left), and (110) lateral electric field (right).

4.2 Increasingly Realistic Models of QD Structure and Composition.

In the previous section we explored the spin texture of hole states in a GaAs/AlAs quantum dot that has a dome shape. Such a quantum dot geometry provides a clear illustration of the emergence of spin textures. However, because InAs has a different lattice constant than GaAs, the strain and piezo-electric effect in InAs/GaAs QD can create different effects that do not exist in GaAs/AlAs QDs. Moreover, QDs are often truncated to create a disk shape that provides a stronger confinement in the vertical direction. In this section we will analyze the spin texture for QDs with compositions and geometries closer to our experimental materials. The results also help us to understand the physical origins of the spin texture.

4.2.1 Disk-shaped AlGaAs QD
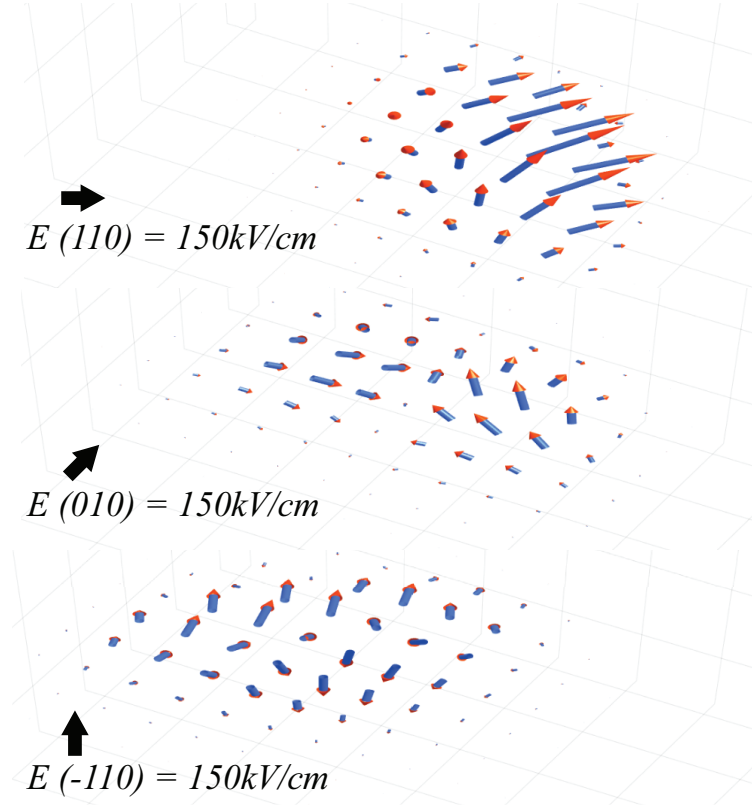
Figure 4.8: Spin polarization with rotating B//E in a disk-shaped AlGaAs QD. The arrows indicate the atomistic spin contribution to a single hole spin state from different atomic sites, integrated at the z=0 plane

We calculate the ground hole spin state in a disk-shaped GaAs/AlAs quantum dot under an in-plane magnetic field and a parallel electric field. This model contains a disk shaped QD without a wetting layer, and the thickness of the disk is $2a$ where a is the lattice constant of GaAs. We keep the magnetic field at 1T and electric field at 150kV/cm and rotate their direction synchronously from (110) to (-110). Figure 4.8 shows the in-plane spin texture of the hole ground state with the rotating parallel electric and magnetic fields. The Sz component of the hole spin starts positive when E and B are in the (110) direction then changes to almost 0 when E and B are in the (010) direction. The Sz component reverses its sign to negative when E and B are in

the (-110) direction.

This result shows that the net hole spin polarization and underlying spin texture of the hole states could remain dependent on the crystal orientation. This is different from the dome-shaped QD model we discussed earlier. In this disk-shaped QD model, the QD structural geometry maintains symmetric in both the in-plane and z direction. However, there's a symmetry shift of the lattice dipole moment when viewing from the (-110) and (110) crystal planes. The spin-flip when E and B field rotates from (110) direction to (-110) direction could be a result of the reversed electrical dipole moment of the atomic lattice.

4.2.2 Dome-shaped Alloyed QD

We next calculate the net spin polarization and spin texture for a dome-shaped InGaAs alloyed QD model with a fixed 1T magnetic field pointing in the (110) direction. This model considers the strain and local piezo-electric fields generated in an alloyed dot. This model represents a QD geometry and composition that can be easily grown experimentally using MBE. The calculation allow us to understand whether the strain or the local piezo-electric field changes the Sz behavior. We present the in-plane spin texture of the hole ground state in Figure 4.9. The Sz component polarizes easily with 100kV/cm electric field, similar to the AlGaAs dome shaped QD model. However, the magnitude of the Sz polarization is not symmetric with electric field, possibly due to the asymmetric piezo-electric field distribution in the alloyed QD.

4.3 Spin Texture Movies

To better visualize the impact of electric fields on the spin texture, we generate animated movies that depict evolutions of the spin texture in the (x,y) plane evolving with different electric fields. Each frame of the film indicates a spin texture under a specific magnetic field and electric field conditions. Here's a list of movies that are related to this work:

1. Single QD GaAs/AlAs dot (dome)
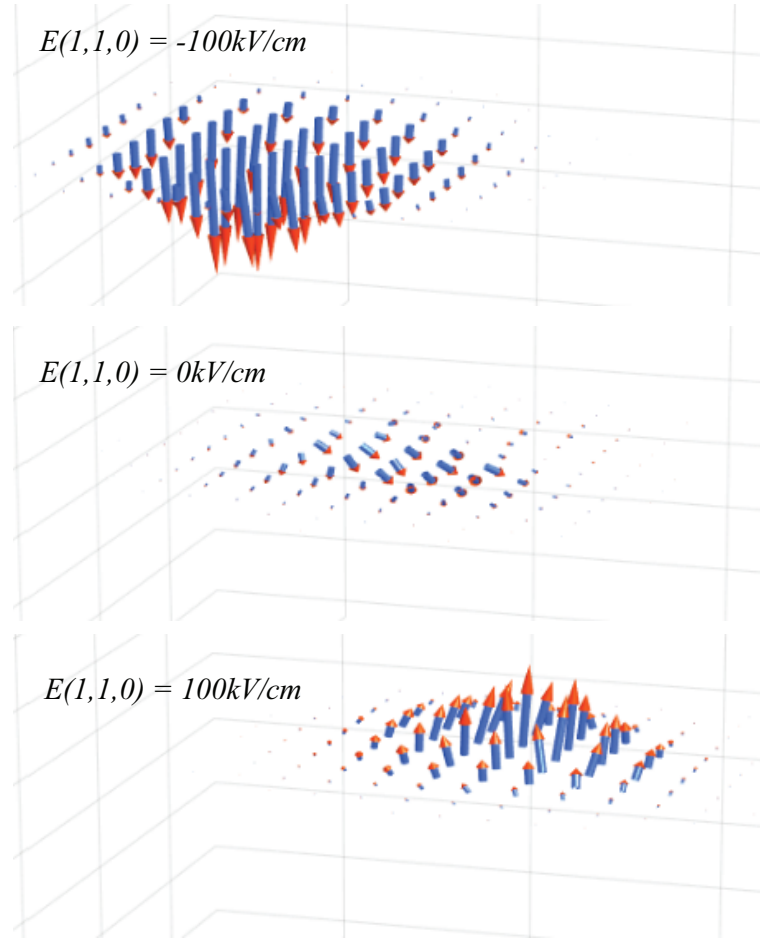
Figure 4.9: Hole spin texture in a disk-shaped InGaAs QD, with a constant (110) direction magnetic field, and three different lateral electric field. The arrows indicate the spin contribution to a single hole spin state from different atomic sites, integrated at the z=0 plane

- $B(110)E(110)$
  https://youtu.be/bJ-LHNIQ_-4
- $B(-110)E(-110)$ https://youtu.be/p8xEniJb-mg
- $B(110)E(-110)$
  https://youtu.be/UkoifLne1Y0
- $B(-110)E(110)$ https://youtu.be/YTLF-uh5MMw

2. GaAs/AlAs QD (disk)

   - Rotation of $B//E$ from (110) to (-110) $B = 1T$, $E = 150kV/cm$
     https://youtu.be/HyFB8gQO7LE

3. InGaAs alloy dot (dome)

  - B(110) E(110) https://youtu.be/bJ-LHNIQ_-4
  - B(110) E(-110) https://youtu.be/yZATIlrOTPk

4.4 Conclusion and Discussion

In this chapter we calculate the spin properties of a hole state in a single QD. The results review new spin phenomenon when we apply an in-plane magnetic field and an in-plane electric field. Specifically, we discover that the out-of-plane components can be polarized by an in-plane electric field that's parallel to the magnetic field's direction. The sign of the Sz component strongly depends on the relative symmetry between magnetic field, electric field, and GaAs crystal plane, and this effect persists in many simulation models that consider different QD shapes and compositions. We explain these surprising net spin effects with the concept of spin texture: a single hole spin state in a QD system is distributed across different atomic sites, rather than a single envelope wave-function that contains only one spin quantum number. This explanation is depicted by the visualization method we established in the previous chapter, and corresponds well with the spin behavior observed in these simulations. We want to emphasize that the spin texture visualization does not show multiple spin states in a single QD, nor the interactions between a hole spin and the nuclear spin bath, but rather the atomistic contributions to a single hole spin wavefunction. Effectively, we are looking at the spin character of each localized Bloch wavefunction that contributes to the overall envelope function describing the single hole. The inhomogeneous spin contribution possibly originates in the boundary conditions of the QD due to the 3-D confinement. We further note that the spin polarization only occurs in hole states. This suggests that the symmetry of the Bloch states unique to the valence band (e.g. spin-orbit coupling) are part of the physical origin of this phenemona. We expect this theory will advance the understanding of the hole states in a confined quantum system and provide new applications based on electrically-controlled spin states in InAs QD systems.

Chapter 5

HOLE STATES IN A VERTICALLY-STACKED QDM

5.1 Introduction

Vertically-stacked quantum dot molecules (QDMs) provide many interesting effects that do not exist in single quantum dots. For example, hole spins states that co-exist in the two quantum dots that compose a QDM can create a hole spin mixing effect, in which the net spin of the hole is a coherent mixture of orthogonal hole spinor projections localized in the two QDs. This effect arises through spin-orbit coupling between the heavy- and light-hole components that make up each hole spinor and relies on symmetry breaking within the QDM and has been both observed experimentally[51] and understood theoretically.[51, 109]

Growth and fabrication of a QDM with a controlled lateral offset in a controllable fashion is extremely hard. To analyze the possibility of controlling this effect using external electric fields and to resolve these spin effects in an arbitrary electric field condition, we applied our tight-binding finite matrix method and spin texture analysis. We will first discuss the important energy features that emerges under a 2-D vector electric field. We will then analyze the spin states in detail using spin texture visualization.

To illustrate our calculation strategy we will look at an example that shows the 4 lowest-energy hole states in a InAs/GaAs QDM, with and without lateral offset. Both QDMs have a 10nm radius, 2nm height and a 4nm GaAs barrier. The asymmetric QDM has a lateral offset of 4nm, as indicated by Fig. 5.1 (a). The geometry of the coordinates (x,y,z) follows the crystal axis ((100), (010), (001)) where z is the growth direction. We first identify the vertical electric field that creates the molecular states in each model
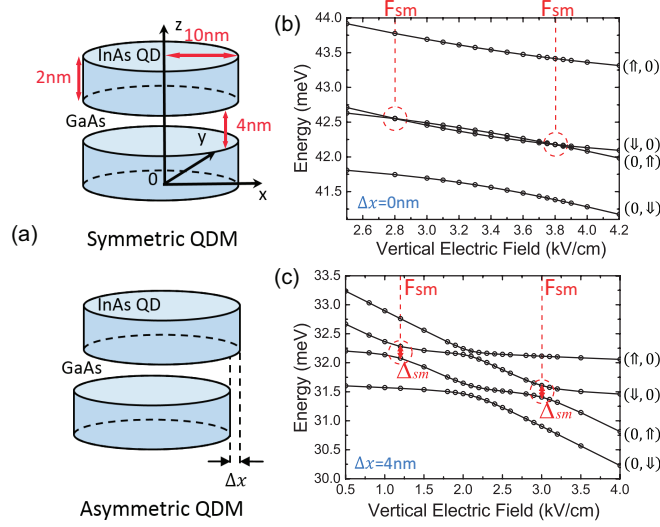
Figure 5.1: (Color Online) (a) Disk shaped QDMs without (symmetric) and with (asymmetric) lateral offset. (b and c) The four lowest-energy hole states as a function of vertical (z-direction) electric field in a symmetric QDM for $B_z = 12$ T (b) and asymmetric QDM with $\Delta x = 4$ nm and $B_z = 6$ T (c).

system. We fix the vertical electric field at that value and then we apply a magnetic field in the z direction to break the spin degeneracy of the hole states (12T for the symmetric QDM, 6T for the asymmetric QDM.) The open circles in Fig. 5.1 indicate the state energies at a specific vertical electric field, as calculated by tight-binding simulation. The lines represent the finite matrix extrapolation of the state energies. To clarify our discussion of spin states, we describe the states away from the resonance electric field with heavy-hole spin state nomenclature: $(\Uparrow, 0)$, $(\Downarrow, 0)$, $(0, \Uparrow)$, and $(0, \Downarrow)$ with the hole located in the bottom (left) or top (right) QD, respectively. Vertical electric fields that create crossing or anti-crossing features of opposite hole spin states are marked as F_{sm} and the anti-crossing gap is labeled as Δ_{sm}. For the asymmetric QDM, whose state energies are shown in Fig. 5.1 (c), two such anti-crossings are observed, at 1.1 kV/cm and 3.2 kV/cm. We will discuss 4 different QDM models: symmetric QDM without piezo-electric field, asymmetric QDM without piezo-electric field, symmetric QDM with piezo-electric field and asymmetric QDM with piezo-electric field. We will

56

explain the results from these models systematically. We will further define these spin states based on their spin texture properties around the resonance electric field.

5.1.1 Symmetric QDM without Piezo-electric Field

We will first take a look at a symmetric QDM without piezo-electric field. Eliminating the piezo-electric field generated in III-V materials helps simplify the simulation and allow us to capture qualitative effects that help us to develop a conceptual understanding of the underlying physics. Based on the model shown in Fig 5.1 (a), we apply increasing x-direction lateral electric field under the constant 12T magnetic field and vertical electric field $F_{sm} = 3.8 kV/cm$. Because the magnitude of the electric field we applied in this model is relatively small, we can achieve high finite matrix calculation accuracy with only 16 states included. Figure 5.2 (a) shows the energy levels of the four lowest-energy hole states as a function of lateral electric field in the x-direction. The state energy decreases by about 3.5 meV when a 30 kV/cm lateral electric field is applied. The nearly parabolic decrease in energy indicates the absence of the permanent dipole moment in the lateral direction, which results from the symmetric cylindrical shape. However, the Stark shift when electric fields are applied along the lateral direction tunes the state energy over a much larger range than the Stark shift for an electric field applied along the growth direction. This larger tuning range for lateral electric fields is due to the extended distribution of the hole wavefunction in the lateral direction. Thus, lateral electric fields may provide a method for fine-tuning the optical transition energies of QDs or QDMs for use in device applications.

An interesting effect of Zeeman splitting quenching is shown in Fig. 5.2 (b). Previous experimental work on InAs QDM have shown that the magnitude of Zeeman splitting can be a function of growth-direction electric field due to the changing spatial distribution of electron and hole wavefunctions.[50, 110, 111, 112, 113, 114] In our case, the changing Zeeman splitting originates, at least in part, from the changing spatial extent of the hole in the lateral direction. This dependence of the hole wavefunction distribution on lateral field is displayed in Figure 5.2 (c). Figure 5.2 (c) shows the

spatial distribution of the third-lowest hole state wavefunction in the $y = 0$ plane computed directly from tight-binding results for three different lateral electric fields. We can clearly see the increasing displacement of the wavefunctions in both QDs, relative to the blue dashed line at $x = 0$, with increasing lateral electric field.

The vertical electric field controls the energy offset between hole states in the two QDs and thus the localization/delocalization of the hole state along the growth axis. The Zeeman splitting reduction should also result in changes of the hole distribution along the z-axis because the shift in Zeeman splitting changes the resonance between the hole states in the separate QDs. Fig. 5.2 (d) shows that the hole distribution along the growth axis changes non-monotonically with increasing lateral electric field. The hole state is more delocalized with a non-zero lateral electric field (5 kV/cm) than for zero lateral electric field. However, the hole state becomes more localized as the lateral electric field increases further (10 kV/cm). We believe that this non-monotonic behavior originates in the competition between multiple effects, including Zeeman splitting reduction and hole spin mixing. [78] The effect of the wavefunction distribution will be clearly illustrated in section 1.3, which describes QDM spin texture.

Finally, the hole spin mixing can be turned on with a constant lateral electric field. As shown in Fig. 5.2 (e), the hole spin mixing anti-crossing gap (Δ_{sm}) becomes positive in the presence of the lateral electric field (F_x). Under this 2-D vector field, a linear increase of Δ_{sm} is observed with increasing F_x, which indicates the ability to tune the hole spin mixing magnitude by lateral electric field. The resonance vertical electric field F_{sm} also changes with the increase of lateral electric field. This effect originates from the Zeeman splitting variation that influences the crossing/anti-crossing points between these two states. In fact, the spin feature for $F_x > 12kV/cm$ becomes extremely hard to resolve in a simple energy diagram because both F_{sm} bunch together to form mixed states. Later in this chapter, we will use our spin texture visualization to see how the spin evolves at higher lateral electric field.
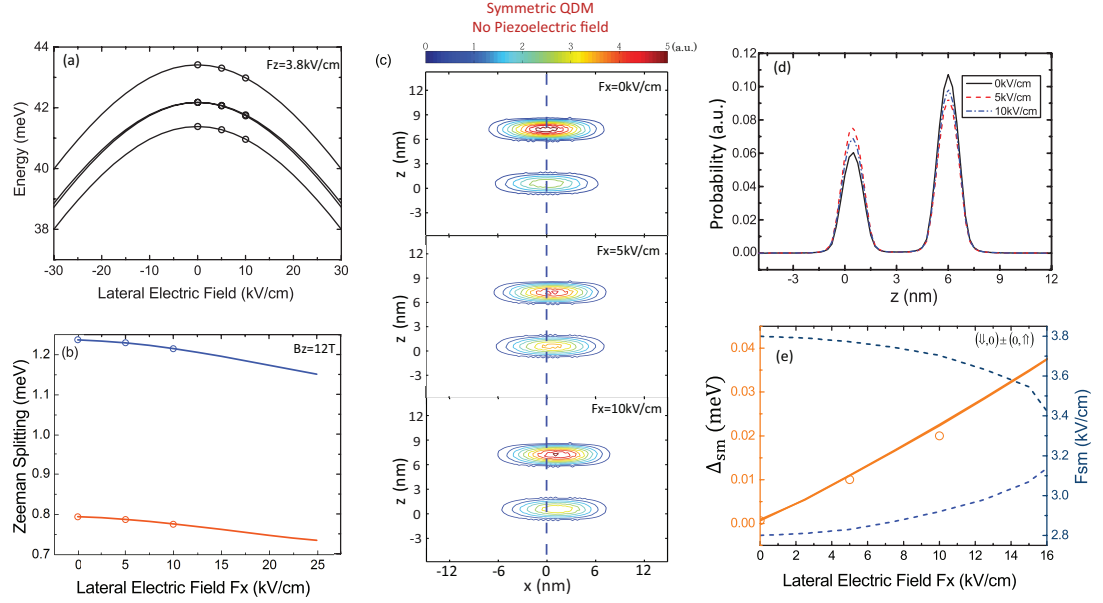
Figure 5.2: (Color Online)Effect of a lateral (x-direction) electric field on a symmetric QDM under a constant 12 T magnetic field in the absence of piezoelectric fields. (a and b). Energy (a) and Zeeman splitting (b) of the four lowest-energy hole states as a function of lateral electric field when $F_z = 3.8$ kV/cm. (c and d) Spatial distribution of a hole wavefunction in $y = 0$ plane (c) and along z axis (d) with different lateral electric fields as derived from the full tight-binding results. (e) Spin mixing anticrossing splitting (Δ_{sm}) and spin mixing resonance vertical electric field (F_{sm}) as a function of lateral electric field.

5.1.2   1 nm Shifted QDM Without Piezoelectric Field

Despite the lack of control of lateral offsets during the growth of QDMs, lateral offsets are commonly observed experimentally, with an average displacement of about 1.8nm. [51] Because such offsets are common in realistic materials, it is important to understand the hole spin properties in such QDMs with lateral offsets, before we move on to more complicated piezo-electric models. In this section, we calculate the energy levels for a QDM model with $\Delta x = 1$ nm lateral offset under a variety of lateral electric fields. Unlike the case of symmetric QDMs, in which the model maintains symmetry in the (x,y) plane, QDMs with an offset behaves differently because of symmetry breaking. We therefore consider two cases: lateral electric field along the shift direction (F_x)
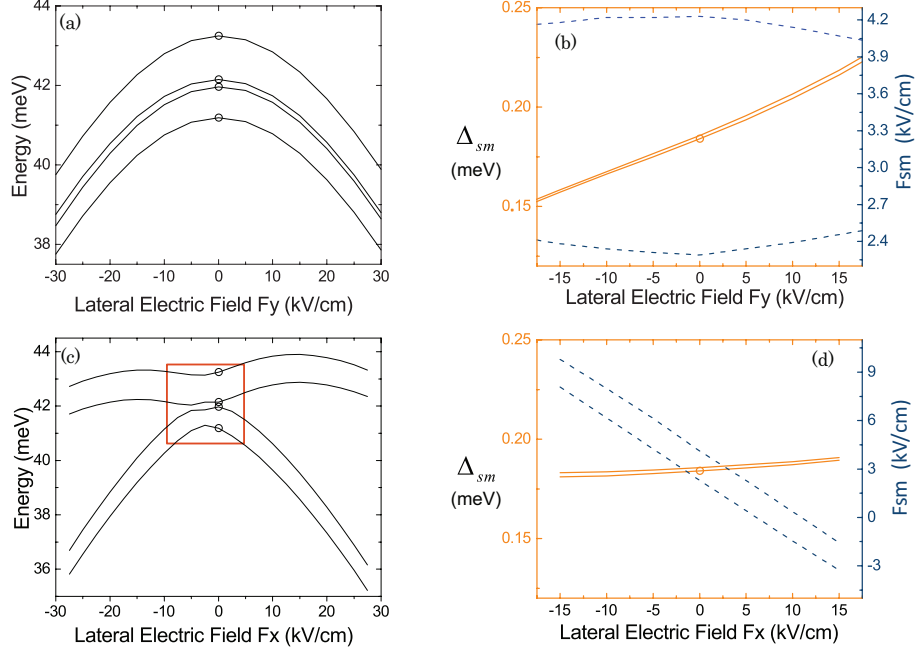
Figure 5.3: (Color Online) Effect of lateral electric field on an asymmetric QDM for $B = 12$ T, in the absence of piezoelectric field. (a) Energy level of the lowest four hole states for $B = 12$ T and $F_z = 3$ kV/cm, as a function of lateral electric field (F_y) perpendicular to the QDM offset direction (x). (b) Spin mixing splitting amplitude Δ_{sm} (yellow solid line) and spin mixing resonance vertical electric field F_{sm} (blue dashed line) as a function of F_y. (c) Energy levels of hole states as a function of lateral electric field along the QDM's offset direction, F_x. (d) Δ_{sm} and F_{sm} as a function of lateral electric field F_x.

and lateral electric field perpendicular to the shift direction (F_y). Again, because the electric field we explore here is relatively small, we find that including 16 states in our calculation is sufficient.

Lateral electric fields (F_y) that are perpendicular to the lateral offset direction (x) generate a Stark shift effect similar to that of the symmetric QDM case. As shown in Fig. 5.3 (a), lateral electric fields in both $\pm y$ directions cause parabolic shifts of the four lowest-energy hole states. The effect of F_y on hole spin mixing states is shown in Fig. 5.3 (b). At 0 lateral electric field there exists a non-zero anti-crossing gap with $\Delta_{sm} = 0.18$ meV. Changing the lateral electric field F_y can modify the hole spin

mixing interaction in a direction-dependent manner. For example, Δ_{sm} decreases with negative y-direction electric field and increases with positive y-direction electric field, as shown in Figure 5.3(b). We suspect that this is because both the lateral electric field and the Δ_{sm}geometry offset contribute to the symmetry breaking in the (110) lattice direction. Changing the direction of y will change the contribution of geometric offset and lateral electric field in the (110) direction from parallel to anti-parallel, which is why the Δ_{sm} can be increased or decreased. A similar effect has been reported in QDMs subject to external strains, which provides an alternative path toward controllable hole spin mixing in QDMs.[115] We again observe a Zeeman splitting reduction in this asymmetric QDM with similar magnitude to that observed in a symmetric QDM. In summary, lateral electric fields orthogonal to the QD shift direction modify hole states in a manner similar to the effect on perfectly aligned QDs, with the exception that the field direction determines whether the hole spin mixing magnitude increases or decreases.

In contrast, Lateral electric fields along the QD shift direction (x) impact the hole state energies in a manner that changes the molecular resonance field F_{sm}. Figure 5.3 (c) shows the energy of the four lowest-energy hole states as a function of lateral electric field along x (i.e. F_x), with a constant vertical electric field. The highlighted red square area shows an energy structure that resembles the effect of vertical electric field. Outside of the red square area, none of the four states resembles a parabola, which is a signature of Stark shift. This is because the lateral electric field, if parallel to the lateral offset direction, changes the wavefunction overlap between the two quantum dot just as the vertical electric field does. It also generates Stark shifts in the lateral direction similar to F_y. The energy feature we see here is a result of a competition between the formation of molecular states and Stark shifts. In section 5.3.2, we will use the spin texture visualization to validate this hypothesis.

The direct impact of F_x on the hole spin mixing vertical resonance field F_{sm} is that it shifts both F_{sm} values the same distance, as plotted in Figure 5.3 (d). The hole spin-mixing anticrossing magnitude Δ_{sm} stays relatively the same compared to the

magnitude under the lateral electric field F_y. This is not surprising because the lateral electric field shifts the hole wavefunctions in each QD similarly in the x direction, thus the electric field applied along the shift axis does not introduce any significant symmetry breaking of the QDM.
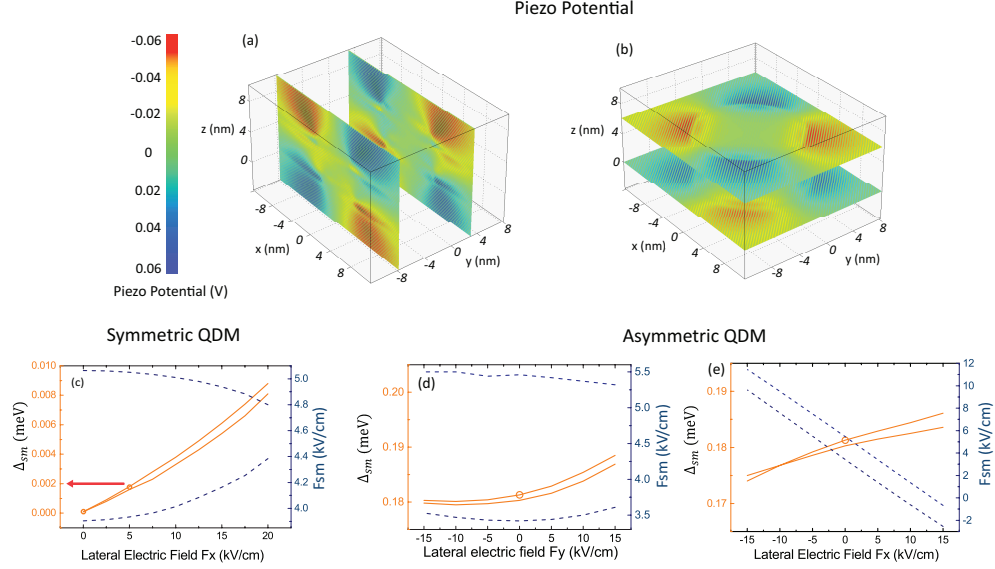
Figure 5.4: (Color Online) Effect of lateral electric field on a symmetric QDM under 12 T constant magnetic field with the piezoelectric field. Planes of the piezo potential at the edge of the QDs (a) and the middle of the QDs (b). (c),(d),(e) Spin mixing splitting amplitude Δ_{sm} (orange) and spin mixing resonance vertical electric field F_{sm} (blue) as a function of lateral electric field in different directions, ((c) Symmetric QDM, (d),(e) asymmetric QDM))

5.1.3 QDM with Piezo-electric Field

In the previous sections we explored the effect of lateral electric field on symmetric and asymmetric QDMs without including the piezoelectric field. However, strain-induced piezoelectric fields can make an important contribution to the local electric field of the QDM. We include piezoelectric effects in our tight-binding calculations as described in the simulation method section. We repeat the process of calculating the energy levels of symmetric and asymmetric QDMs under applied electric fields with

piezoelectric fields included. We analyze the results to understand the physical conse-
quences of the piezoelectric fields and their interplay with QDM symmetry and applied
lateral electric fields.

Figure 5.4 (a) and (b) display two different 2D cross-sectional planes of the
piezoelectric potential of a symmetric QDM. The vertical planes in Figure 5.4 (a) lie
at the outer edges of the two QDs and the horizontal planes in Figure 5.4 (b) lie at the
middle of each QD. These figures show that piezoelectric potential dipoles are formed
at the corner of each quantum dot, but with a 90° rotation of the dipole orientation
between the two dots. The symmetry of piezoelectric potentials has been found to
depend on a variety of parameters.[116, 117, 118] The rotated symmetry we find occurs
when QDs are close together and act as a strongly coupled entity.[116] Under a constant
lateral electric field, we observe Stark shifts and Zeeman splitting reduction similar to
QDMs without piezoelectric fields with only small shifts in the resonant electric fields
F_{sm} at which molecular states are formed. However, piezoelectric fields substantially
change the magnitude and tuning range of hole spin mixing, as we now discuss.

Figure 5.4 (c) plots the Δ_{sm} and F_{sm} for the two hole spin mixing anticrossings
of a symmetric QDM as a function of a lateral electric field along x. In a symmetric
QDM model, piezoelectric field alone cannot induce hole spin mixing, and two crossings
occur as a function of applied vertical electric field. In other words, $\Delta_{sm} = 0$ when
$F_x = 0$. Anticrossings at both F_{sm} emerge when a non-zero lateral electric field is
applied ($F_x > 0$). Zeeman splitting effects (not shown) cause the two F_{sm} to converge
with increasing lateral electric field as described above. Although the emergence of
non-zero Δ_{sm} as a function of F_x is qualitatively similar to what is observed in the
absence of piezoelectric fields, the magnitude of Δ_{sm} is substantially reduced. As
shown in Fig. 5.4 (c), Δ_{sm} at $F_x = 15$ kV/cm is about 6 μeV, much smaller than the
35 μeV anticrossing observed in the absence of piezoelectric fields (Fig. 5.2).

We next explore the consequences of including piezoelectric fields in the simula-
tions of asymmetric QDMs with $\Delta x = 1$ nm. Following the analysis described above,
we consider lateral electric fields perpendicular to (F_y) and parallel to (F_x), which is

the lateral offset direction (x). The results are presented in Figure 5.4 (d) and (e), respectively. In both cases, the Δ_{sm} value remains nearly constant as a function of lateral electric field. For electric fields parallel to the shift axis (Figure 5.4 (e)), this result is similar to what is observed without the inclusion of piezoelectric fields (Fig. 5.3 (d)). We therefore conclude that the inclusion of piezoelectric fields does not significantly alter the physics of hole spin mixing for electric fields along the shift axis. For electric fields perpendicular to the shift axis (Figure 5.4 (d)), the change in Δ_{sm} is about 7 times smaller than that observed when piezoelectric fields are not included (Fig. 5.3 (b)). This suggests that the symmetry breaking induced by the applied lateral electric field is largely compensated by the local piezoelectric field.

In summary, the emergence and evolution of hole spin mixing is qualitatively similar for QDMs studied with and without the inclusion of piezoelectric fields. However, the magnitude of hole spin mixing interactions (Δ_{sm}) is reduced when piezolectric fields are included. Piezoelectric fields are inherent to the InAs/GaAs QDM system, and thus intentional generation of strong spin mixing interactions using constant lateral electric fields will be challenging. A possible explanation is that the piezoelectric field counters the effects of external electric field and preserves the existing symmetry of QDM. As a result, constant electric fields do not substantially alter the symmetry of the electronic states of the QDM. This suggests that a gradient in the lateral field, with different lateral fields applied to each dot, may enhance the symmetry breaking. We next explore the consequences of lateral electric field profiles that have a gradient with different lateral field magnitudes at the locations of the two QDs that comprise the QDM. In the subsequent section we will use spin texture visualizations to understand these effects.

5.2 Lateral Electric Fields with a Gradient

Before we begin discussions about applying a gradient electric field, we'd like to understand the physics behind a gradient electric field. From Maxwell's Equations we know that under a static magnetic field, the divergence of an electric field is zero.

Therefore, $\frac{\partial F_y}{\partial z} = \frac{\partial F_z}{\partial y}$. We consider $G_{yz} = \frac{\partial F_y}{\partial z}$ and write the electric field at location (x,y,z) with a constant gradient in the (y, z) plane as

$$\vec{F(x, y, z)} = \vec{x}F_x + \vec{y}(F_y + G_{yz}(z - z_0)) + \vec{z}(F_z + G_{yz}(y - y_0)) \tag{5.1}$$

This type of electric field is commonly applied in ion-trap quantum computing applications, where the gradient factor G is not a constant but a function of coordinate. To simplify this problem and make it suitable for our discussion, we assume that the QDM is small enough so that we can approximately treat G as a constant. We will also choose (y_0, z_0) as the bottom of the top quantum dot in a quantum dot molecule.
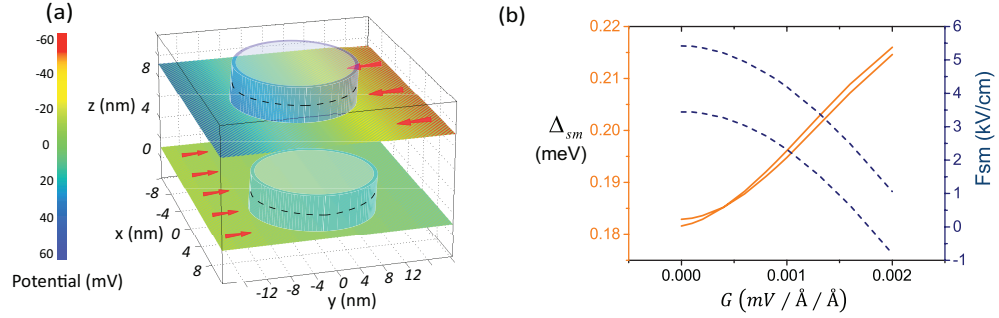
Figure 5.5: (Color Online) Effect of lateral electric field with a gradient in the growth direction on asymmetric QDMs with piezoelectric fields included. (a) Electric potential for gradient $G_{yz} = 0.002$ $(mV/)/$. (b) Δ_{sm} (orange) and F_{sm} (blue) as a function of lateral electric field gradient G.

In order to calculate the state energy under a gradient electric field, additional finite matrix terms must be calculated, namely $V_{ijy} = \langle \phi_i | \vec{r} | \phi_j \rangle$. After computing those terms, we perform the calculation on both symmetric QDM and asymetric QDM, considering G_{yz} values ranging from 0 to 0.002 $(mV/)/$.

The results in Figure 5.5 show the gradient electric field effect in an asymmetric QDM. In this case, we applied an electric gradient in the (y,z) direction, perpendicular to the lateral offset direction x. Figure 5.5 (a) shows the electric potential in the plane of the two QDs where $G = 0.0002$ $(mV/)/$. The red arrows indicate the direction

and relative magnitude of F_y. On the right side, we can see that the hole spin mixing magnitude Δ_{sm} clearly increases with the increase of the electric field gradient, while the resonance electric field shifts in the vertical direction. The oppositely-oriented electric fields in the planes of the two QDs will cause the hole wavefunctions to shift in opposite directions, breaking the QDM symmetry in a manner similar to the lateral shift that occurs in asymmetric QDMs.

The range of Δ_{sm} values accessible for this range of G_{yz} is still limited, possibly because of the strong piezoelectric fields, and thus larger field gradients would likely be desirable for device applications. F_{sm} shifts with G_{yz} due to the changes in both F_y and F_z. Unlike the case with constant lateral electric field, we do not observe a Zeeman splitting reduction as a function of increasing gradient magnitude. As a result, the spacing between the two F_{sm} is nearly independent of G_{yz}.

5.3 Spin Texture in QDM

In the previous sections, we explored the effects of different electric fields in QDM with or without symmetry breaking. We used the energy diagram and the interaction signature anti-crossing to explain the formation of a hole spin mixing state and a molecular state. However, this method becomes increasingly unreliable as we dig deeper into the energy diagram and the anti-crossing or crossing points become harder to resolve. For example, the difference between "crossing" and "anti-crossing" in the energy diagram is hard to determine if the two lines anti-cross with a very small gap. We usually have to refine the electric field search down to a resolution of several mV until we can confirm existence or absence of a spin mixing anti-crossing from the energy diagram. Furthermore, the actual hole state near multiple anti-crossing features can be hard to resolve, such as in Figure 5.1 (b) at around 3.3kV/cm where the second/third lowest hole state sits between two anti-crossings. Moreover, in Figure5.1 (c), there seem to be two other anti-crossings forming around 2.2kV/cm. All of these spin states are impossible to identify if we judge solely on the energy diagram.

In this section, we use the same spin texture method we used in single QD to explain the hole spin mixing effect, and illustrate spin states that are hard to identify in the energy diagram.

5.3.1 Hole Spin Mixing Effect in QDM

We will start by focusing on the hole spin mixing effect in QDM models that considers piezo-electric fields. Hole states in these models can be more explicitly explained when we summarize all the hole spins into 2 different planes, each containing spin contributions from each QD. Figure 5.6 shows the spin property of the states indicated by the red dot in the energy diagram, evolving with vertical (growth direction) electric field. The energy diagram indicates that the 2nd and 3rd lowest hole states cross at F=3.8kV/cm and Fz=5kV/cm. The spin polarization around these crossing points tell us that the spin contribution from each QD points in the same z direction, and they flip directions whenever the red dot passes over a crossing point. This is because the lack of interaction at F_{sm} simply makes the two spin states flip in the central region. In fact, if we trace over the parabolic curve on the 2nd lowest states at Fz=3kV/cm, instead of flipping the state at each crossing point, we observe same Sz projection across all electric field strengths. In other words, this discontinuity at the crossing point indicates two individual states without interaction, i.e. no anti-crossing. A full animation based on this effect can be found in the appendix.

In contrast, the spin texture of a hole spin mixing effect is shown in Figure5.7, with an asymmetric QDM (1nm shift) model including piezo-electric fields. Each frame in the figure corresponds to a different vertical electric field magnitude, as indicated by the x axis on the right. The spin polarization of the state indicated by the red dot has opposite Sz component near the resonance electric field F_{sm} (-1kV/cm and 0.5kV/cm). This is a direct illustration of the hole spin mixing effect using the atomistic method. Furthermore, as we increase the vertical electric field from one F_{sm} to the other, the spin component in each dot will flip its Sz projection and form another hole spin mixing point. As for the states in between the hole spin mixing resonance electric field, the spin

contribution from each individual QD maintains its direction, indicating no spin mixing effects around those electric field regions. In other word, the range of vertical electric fields that generate the spin mixing effect is around 0.6kV/cm. However, molecular states emerge at the central electric field F=4.5kV/cm, which properly explains the reverse anti-crossing feature between the 2nd lowest hole state (red) and the 3rd lowest hole state(yellow), in the energy diagram.

Using the spin texture method, we illustrated the evolution of the atomistic contributions to the spin projection of the molecular state around the hole spin mixing region, which would not have been possible with only the energy diagram. Next, we will discuss the effect of applying different lateral electric fields.

5.3.2 Lateral Electric Fields in QDM

We discussed previously how lateral electric field changes the energy diagram and how hole spin mixing states are formed in a QD/QDM. Using the spin texture visualization method, we will further this discussion and give direct explanations of the effect of lateral electric fields.

We first explore the symmetric QDM model. The spin texture with different vertical electric fields under a constant lateral electric field Fx=10kV/cm is shown in Figure 5.8 The energy diagram shows a negligible anti-crossing gap around $4\mu eV$ at Fx=10kV/cm, as indicated by Figure 5.4. The spin distribution in the two QDs are shown on the left, with little indication of opposite spin contributions from each QDM. If we choose our vertical electric field carefully enough, some spin mixing effects could appear at Fz=5kV/cm, as indicated by the 4th picture, even though the magnitude of the spin mixing is very small. If we increase the lateral electric field to 20kV/cm, the Zeeman splitting quenching effect will dominate and push the two F_{sm} closer, as shown in Figure 5.9. While it is hard to determine the spin mixing effect using the energy diagram alone, we do not see spin mixing textures forming around the two new F_{sm} either.

The more effective way of inducing the spin mixing effect in a symmetric QDM is to apply a gradient electric field. We therefore use the spin texture calculation to analyze the same gradient electric field model presented in section 5.1.2. As shown in Figure 5.10 with a gradient factor G=0.002mV/A/A, the two anti-crossing gaps are visibly significant, and the spin contribution from the two QD are opposite of each other, providing direct evidence of the formation of spin mixing effect.

5.3.3 Electric Field Parallel to the Lateral Offset

Spin texture can also helps us illustrate the effect of the lateral electric field parallel to the geometric offset in an asymmetric QDM. In our previous discussion, we observed an energy diagram that shows the formation of molecular states and hole spin mixing states in a asymmetric QDM by changing the x direction of the electric field only. The origin of this effect is yet unclear. However, we can better explain this effect with the help of the spin texture visualization that plots the distribution of spin/wavefunction in a QDM directly. In Figure 5.11, we can see how the spin states in this QDM evolves with x direction electric field that's parallel to the geometric offset. The spin texture with different lateral electric field confirms the formation of the hole spin mixing effect at Fx=3kV/cm and Fx=8kV/cm and the molecular state around 5.5kV/cm. The QD spin contribution transforms from mostly in the bottom dot to mostly in the top dot as a result of the shift in wavefunction amplitude caused by the electric field in the x direction.

5.4 Summary

In this Chapter, we explored the effect of different lateral electric fields on a single InAs/GaAs QDM using tight-binding and finite matrix calculations. We discovered that lateral electric fields can induce Stark shifts that are lager than that observed under vertical electric fields and can induce Zeeman splitting quenching effects. Moreover, lateral electric fields can generate/modulate hole spin mixing states in a InAs/GaAs

QDM. However, the effect is strongly inhibited by local piezo-electric fields. A gradient electric field, on the other hand, can be used to simulate the geometric offset and generate hole spin mixing effect with a large magnitude. We further explain the origin of spin mixing using spin texture visualizations, allowing us to resolve hole spin states that cannot be resolved using energy diagrams alone. In this way, the existence of hole spin mixing partially validates our spin texture hypothesis. This work therefore suggests the possibility of building a qubit system based on hole spin mixing states controlled by external 2-D electric fields.

Figure 5.6: Symmetric QDM with different vertical electric field at 0 lateral electric field.
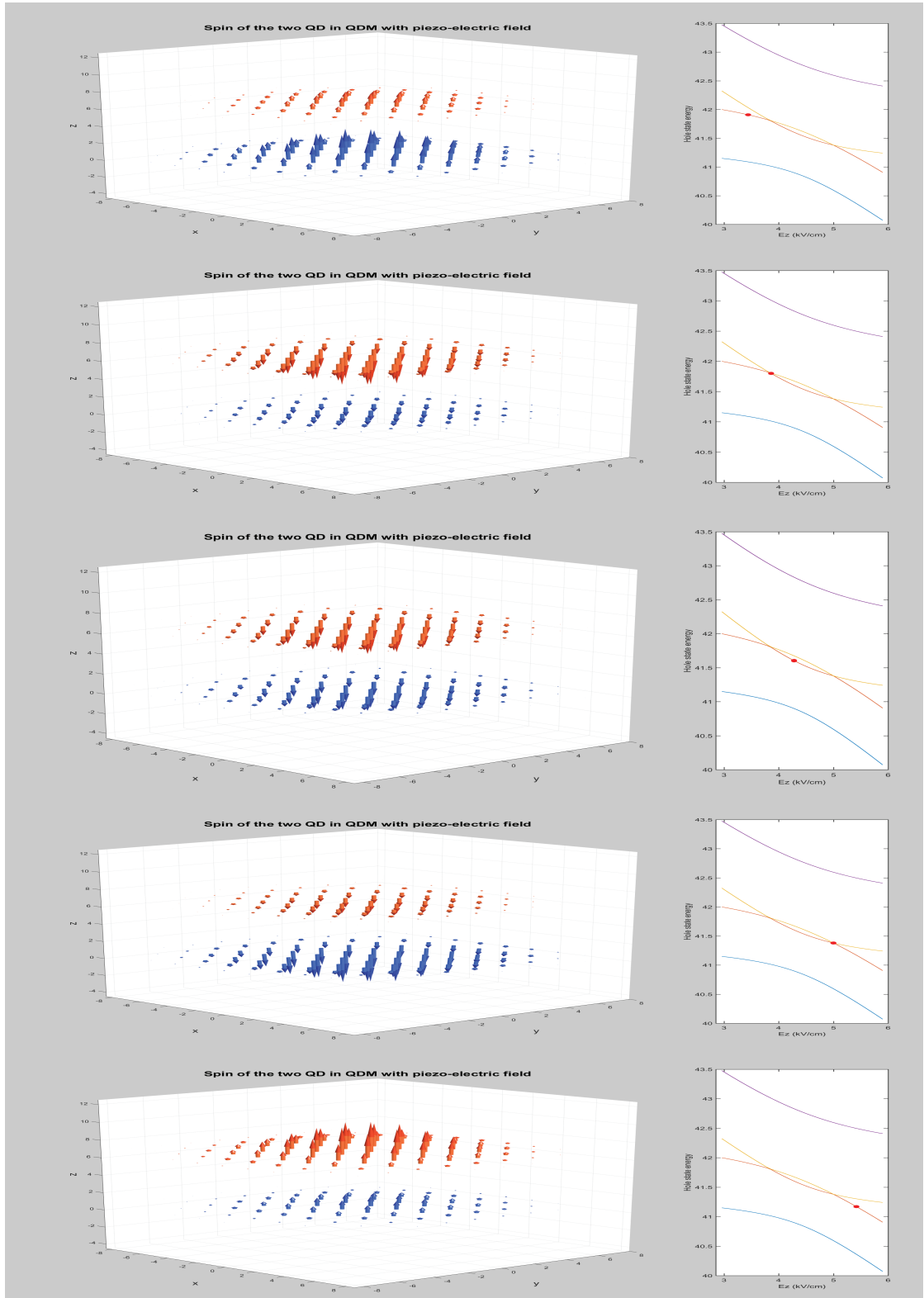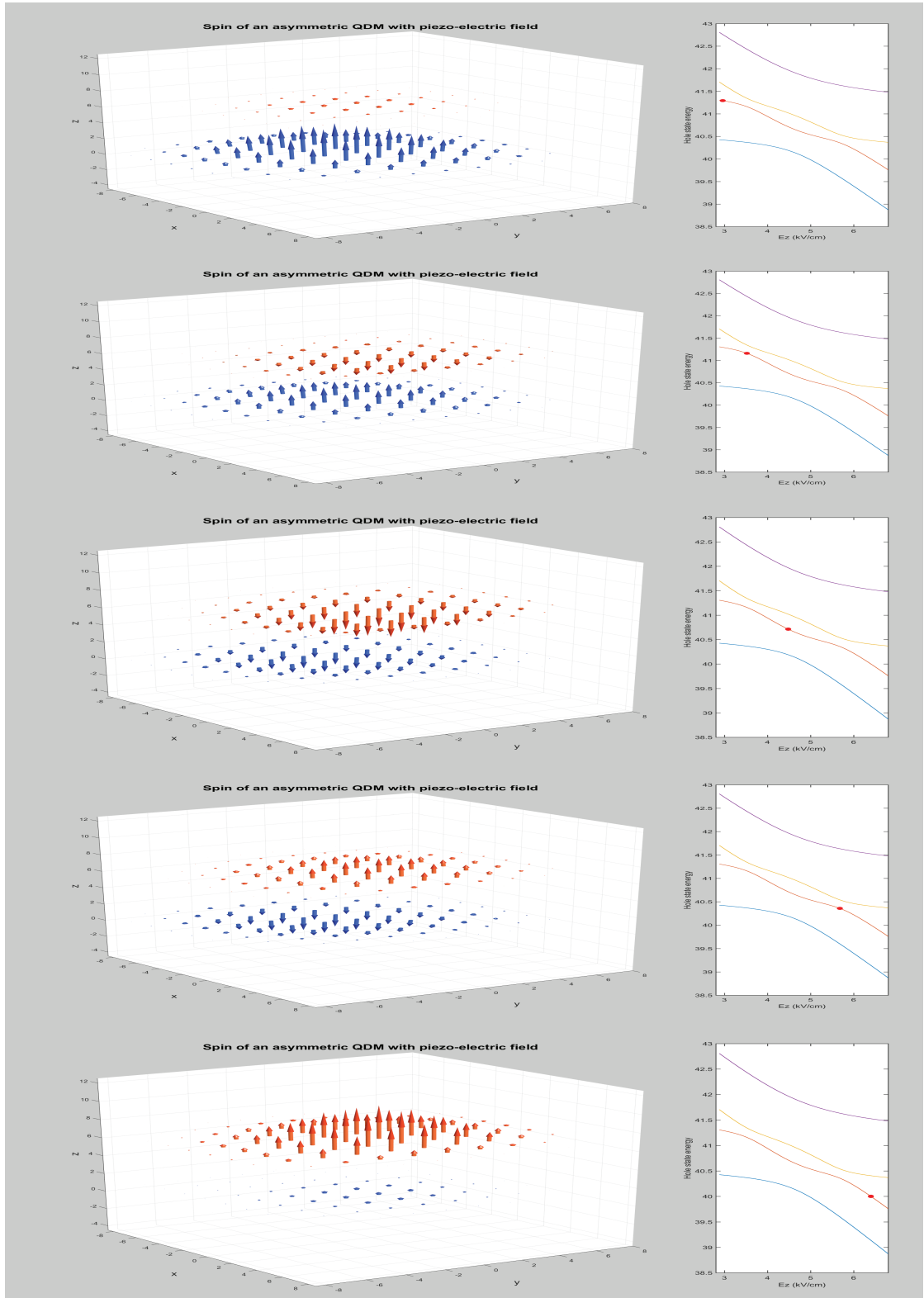
Figure 5.7: Asymmetric QDM with different vertical electric field and 0 lateral electric field. Hole spin mixing effect is clearly shown around 0.5kV/cm and -1kV/cm
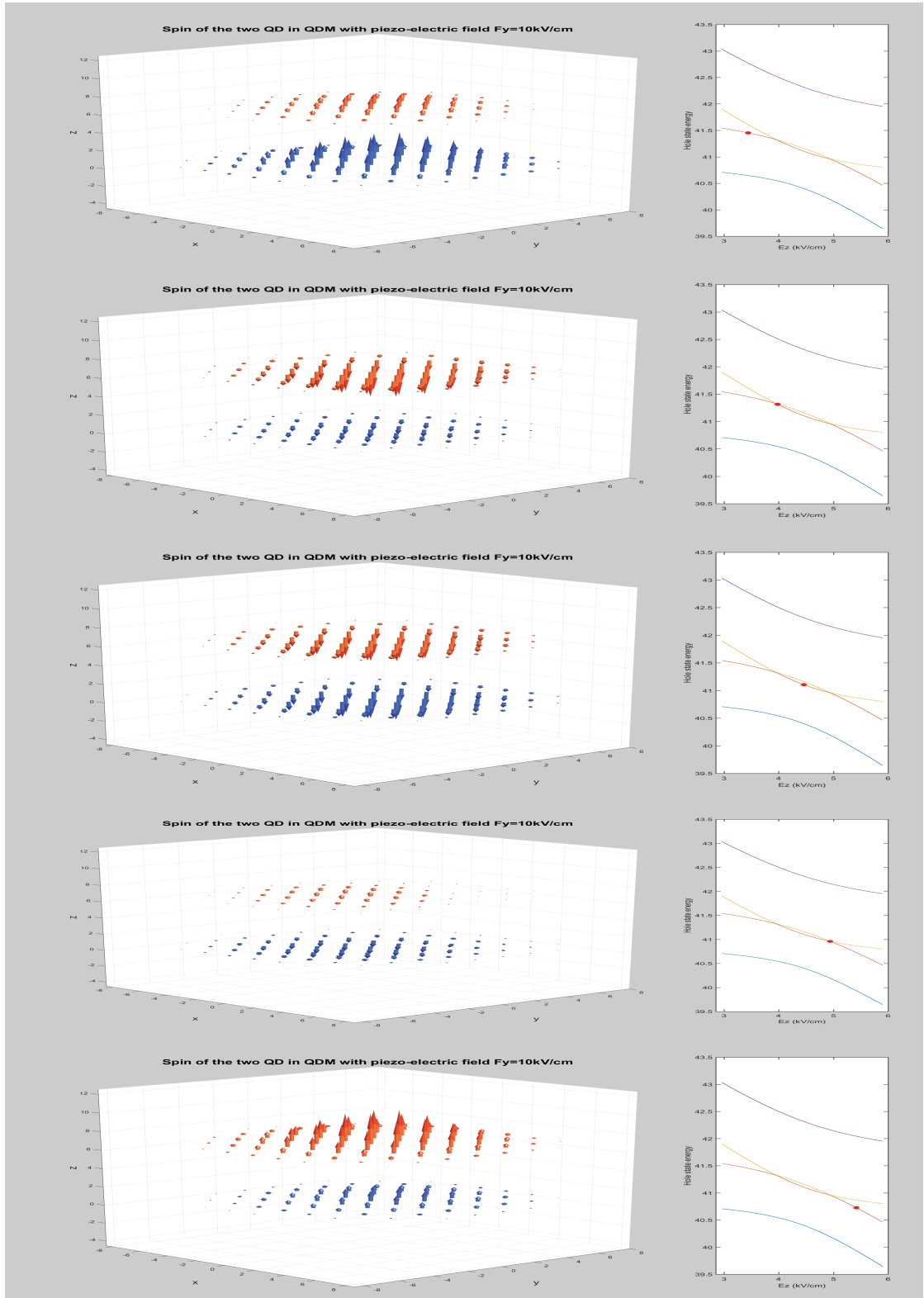
Figure 5.8: Symmetric QDM with different vertical electric field and a constatn 10kV/cm lateral electric field.
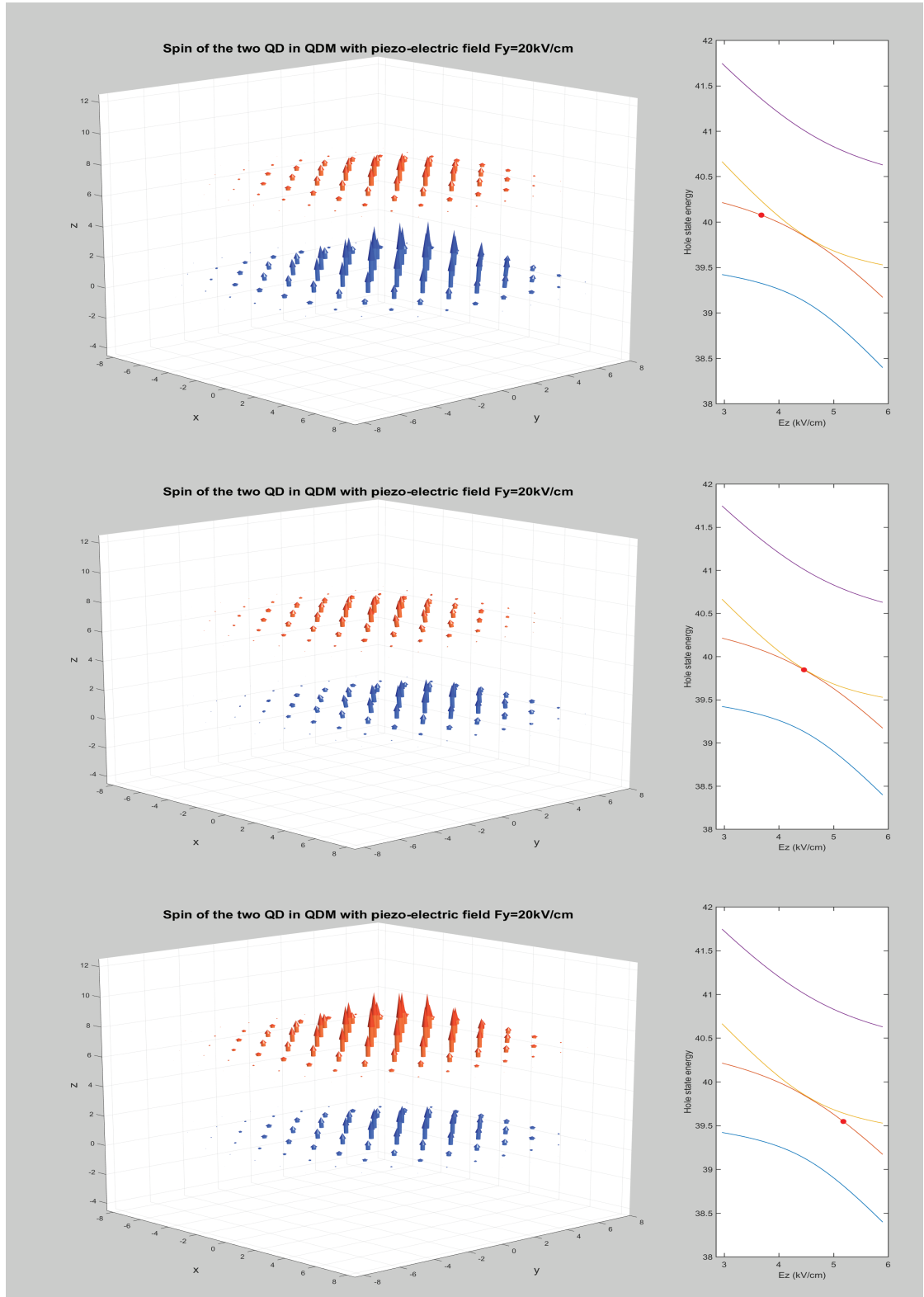
Figure 5.9: Symmetric QDM with different vertical electric field and a constatn 20kV/cm lateral electric field.
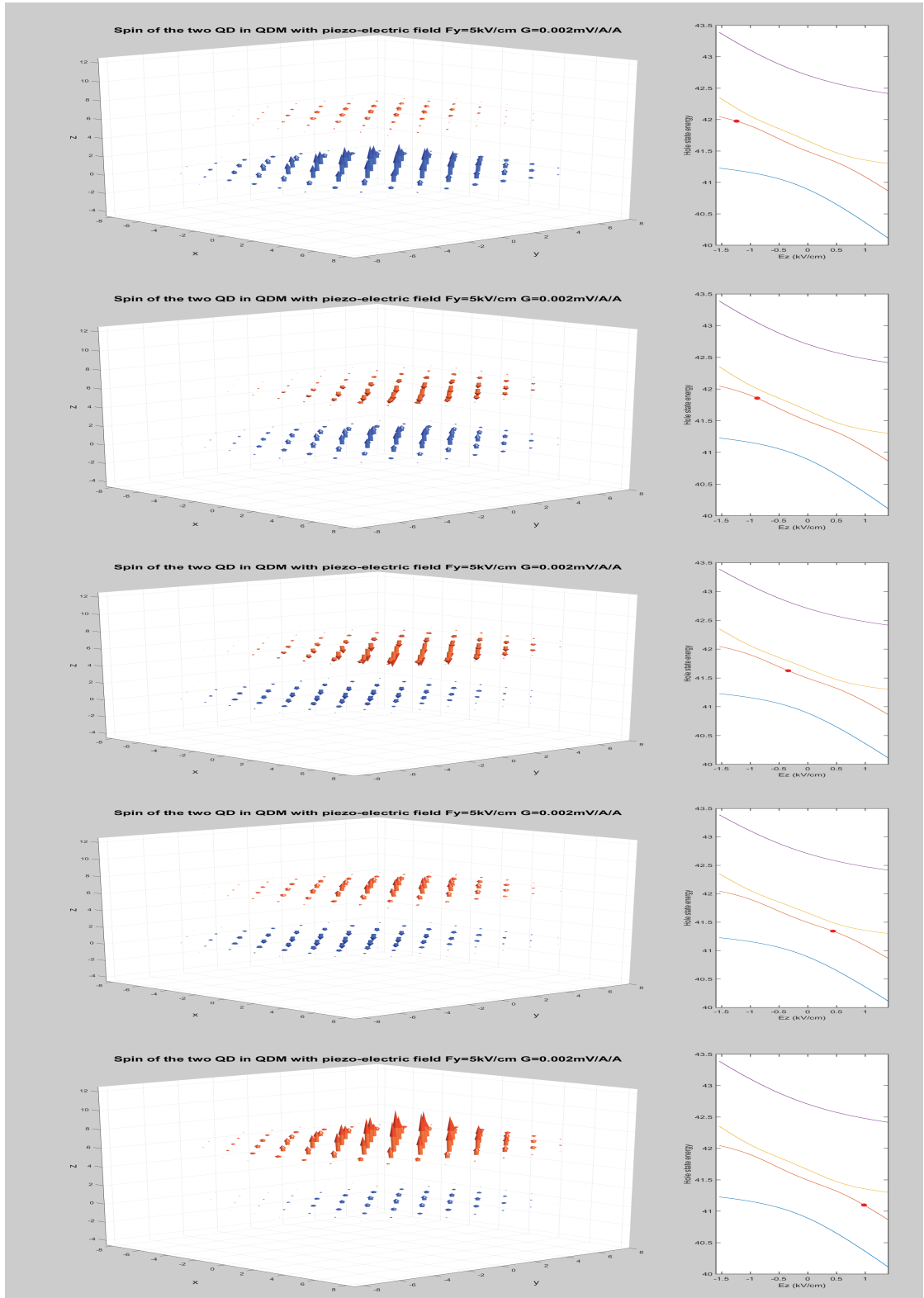
Figure 5.10: Symmetric QDM with different vertical electric field and a gradient lateral electric field. Hole spin mixing effect just like asymmetric QDM is shown.
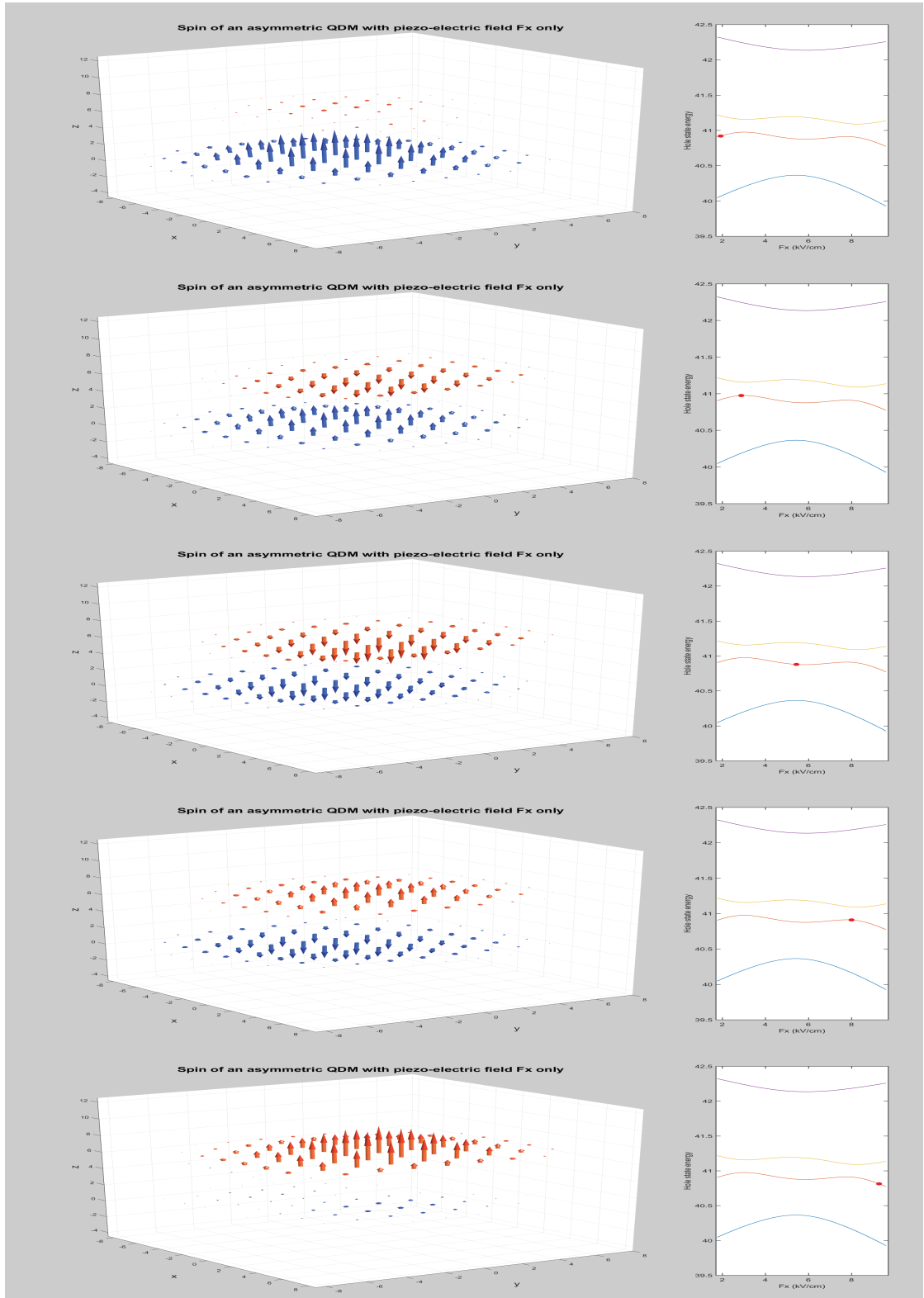
Figure 5.11: Asymmetric QDM with different x direction lateral electric field.

Chapter 6

2-D ELECTRIC FIELD DEVICE DESIGN

6.1 Background

Applying 2-D electric fields in a vacuum system is critical for applications such as ion traps[24], and has wide applications in mass spectrometry.[119] However, it has not been demonstrated in a solid-state system. Traditional devices such as metal oxide semiconductor field effect transistors(MOSFETs), while using multiple electrodes to control the current flow, does not focus on applying arbitrary direction electric fields at the quantum level. Moreover, the low-temperature conditions for InAs QDs also changes how semiconductors devices perform. Thus, new device geometries have to be invented to apply a 2-D electric field in an III-V QD system.

Zhou et al. have proposed a 4-electrode device to charge a lateral quantum dot molecule (LQDM) using a vertical electric field while simultaneously applying a uniform lateral electric field.[120] The device structure is shown in Figure 6.1. This device uses an n-doped GaAs substrate with a back Ohmic metal contact. QDs are embedded in intrinsic GaAs grown by MBE, 35nm away from the n-doped layer. A rectangular 1μm wide strip mesa is etched and two over-the-top lateral electrodes are deposited on the side of the mesa. The two lateral electrodes are insulated from the bottom doped layer by 20nm of Al_2O_3. The top electrode, separated from the mesa by 300nm of SiO_2 insulation layer, covers the device and has micron-sized apertures for optical measurements.

Zhou et al. also show that by applying different voltages to the 4 electrodes, a uniform vertical electric field can be generated in the entire mesa. In some cases, uniform lateral electric fields in an 80nm-wide region can be formed at a specific location
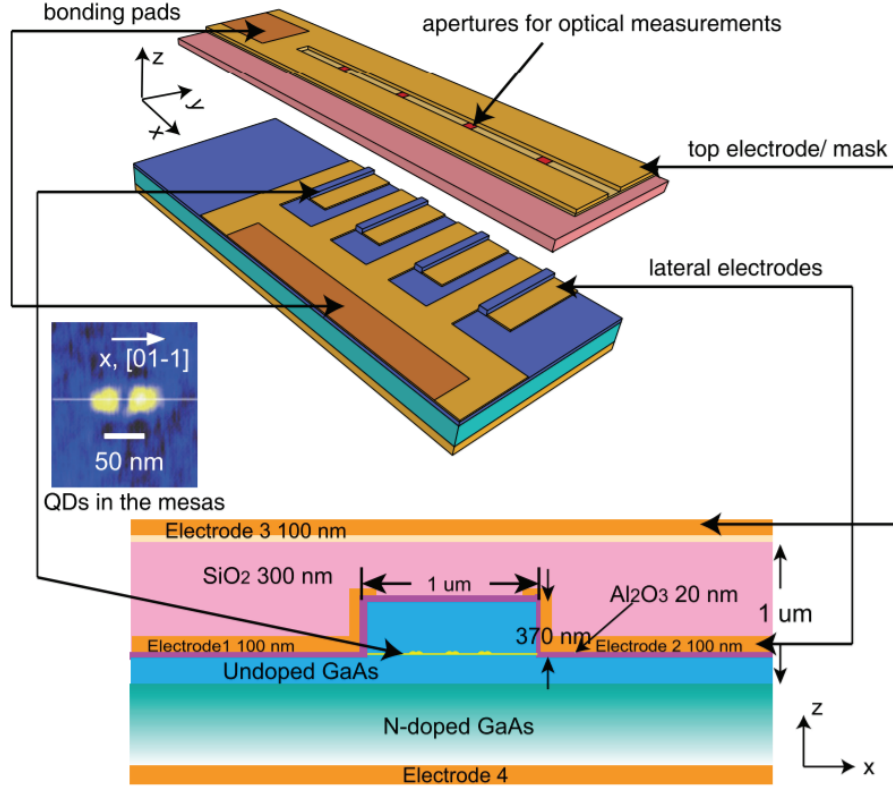
Figure 6.1: Schematic of 4-electrode device designed by Xinran Zhou et al. [120]

of the mesa. The electric field profile is calculated with COMSOL simulations using the AC-DC module. This simulation model calculates the electric field profile using Maxwell's equations and treats different materials with different dielectric constant. However, the results can be inaccurate when specific semiconductor parameters are not taken into accounts.

6.2 COMSOL Simulation with the Semiconductor Module

To address the shortcomings of the previous COMSOL modeling and design a device that can apply uniform 2-D electric fields in a GaAs matrix, we develop a COMSOL model using the semiconductor module. This module treats all materials with their semiconductor properties, and compute the electric potential φ using the
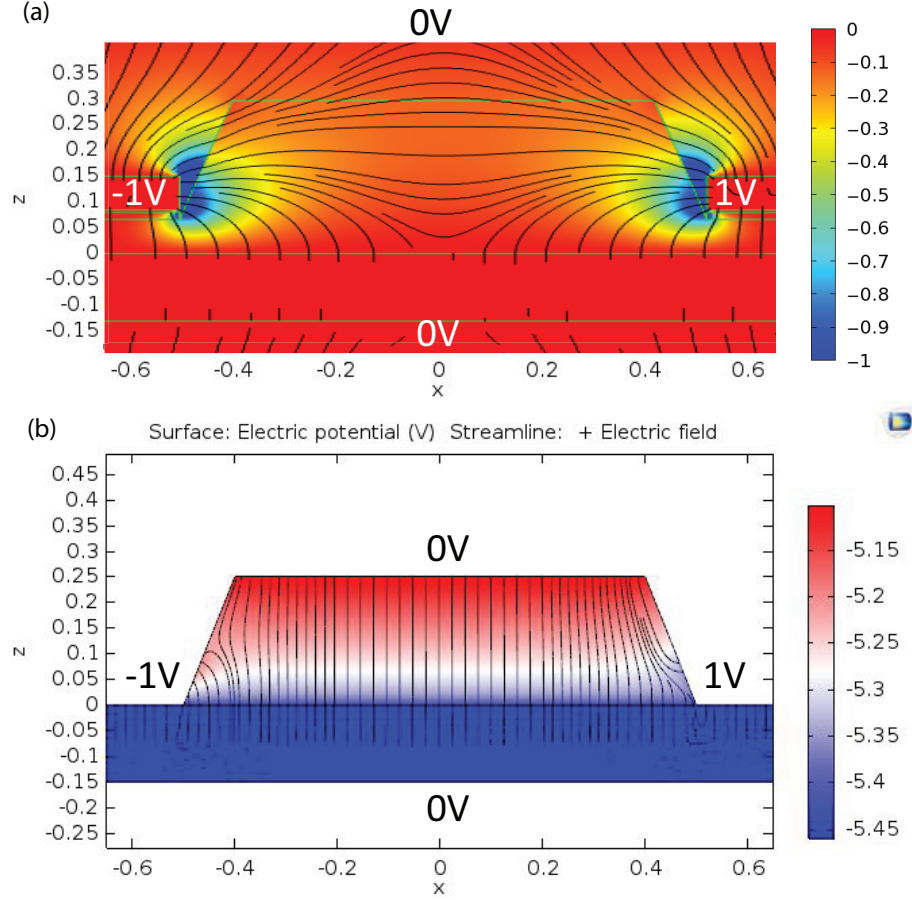
Figure 6.2: Direct comparison between an ACDC model and a semiconductor model, based on the device geometry designed by Zhou et al.

Poisson equation:

$$\nabla^2 \varphi = \frac{\epsilon}{q}(n - p + N_A^- - N_D^+). \tag{6.1}$$

Here ϵ is the permmitivity, q is the charge of an electron, n and p are electron and hole densities respectively, N_A^- is the ionized acceptor density and N_D^+ is the ionized donor density.

A direct comparison between the AC-DC model and the semiconductor model simulation using COMSOL is shown in Figure 6.2. We adopt the design parameters from Zhou [120] and calculate the electric field profile using either the AC-DC module

or the semiconductor module. We apply $\pm 1V$ on the two lateral electrodes and ground the top and bottom electrodes. The surface map shows the relative electric potential, and the streamline shows the direction of the electric field. In the AC-DC calculation, as shown in (a), a semi-uniform lateral electric field can be formed at the center of the mesa, as indicated by the horizontal electric field streamlines.

The AC-DC module does not take into account the doping level or the depletion width of the semiconductor. This is important because MBE grown GaAs usually have a background doping in the range between $1E14/cm^3$ to $1E16/cm^3$. This level of doping could affect the depletion width, therefore the profile of the electric field. Using the same geometry and voltage setup, we calculate the electrical profile in the presence of a background doping of $1E15/cm^3$ in the intrinsic GaAs grown by MBE. The result is shown in Figure 6.2(b). Electric fields in the mesa are almost solely along the vertical direction, instead of lateral. The contrast between the AC-DC module's calculation and the semiconductor module's calculation is evident. A qualitative explanation is that the background doping changes the depletion width of the material, so that effectively shielding the lateral electric fields at the metal-insulator-semiconductor interface. This shows that new device designs and a deeper understanding of the device performance are needed, and should be validated by simulations that take the semiconductor effects into account.

6.3   Improved Device Design

6.3.1   3-electrode Design in an Intrinsic GaAs Matrix

We first design a device that can apply 2-D vector electric fields without charging the QD. The overall pattern layout is similar to what Zhou et al. proposed, with the difference of eliminating the bottom doped layer and SiO_2 insulation. The key difference is that we shrink the mesa size down to 550nm, rather than 1μm. Figure 6.3 (a) shows the side view of the 3-electrode device. QDs are grown on an intrinsic GaAs wafer and embedded in unintentionally doped GaAs grown by MBE. The mesa
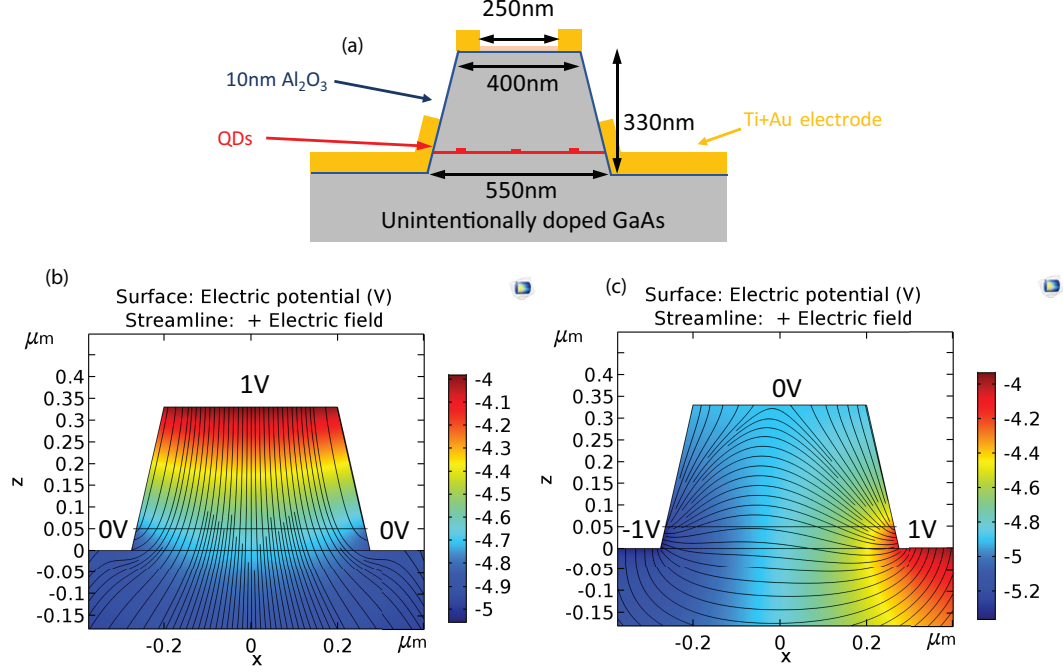
Figure 6.3: Improved 3-electrode device geometry and simulation result for both the vertical and the lateral electric field. (a) The geometry of the 3-electrode device (b) and (c) The surface potential map and electric field streamline calculated using the semiconductor module

height that contains the QDs is 330nm. A 10nm Al_2O_3 layer covers the mesa conformally, creating insulations between the three electrodes. A 400nm wide top electrode consisting of Ti and Au is deposited on top of the mesa, with a 250nm wide square aperture (not shown here) for top-down optical access. The bottom of the mesa is 550nm, resulting in a 15° angle on the sidewall. The two lateral electrodes are placed at the bottom of the mesa, with partial sidewall coverage.

Figure 6.3(b) and (c) shows the electric field profile of two different voltage configurations simulated using the COMSOL semiconductor module. We choose a moderate unintentionally doping of $1E15/cm^3$ for the MBE grown GaAs and calculate the electric potential at room temperature. The QDs are located at the z=0.05 line. When we ground the two lateral electrodes and apply 1V to the top electrode, as shown in (b), a pure vertical electric field is formed with little lateral components. When we

ground the top electrode and apply equal and opposite voltages to the two lateral electrodes, as shown in (c), an almost uniform lateral electric field can be formed with little vertical components. Having a uniform lateral electric field across the entire mesa is exceptionally advantageous in device characterizations because the location of a QD could be anywhere in the mesa. However, with every electrode insulated from the mesa, electrical charging is not probable.

6.3.2 4-electrode Design in a n-i-p Vertical Diode
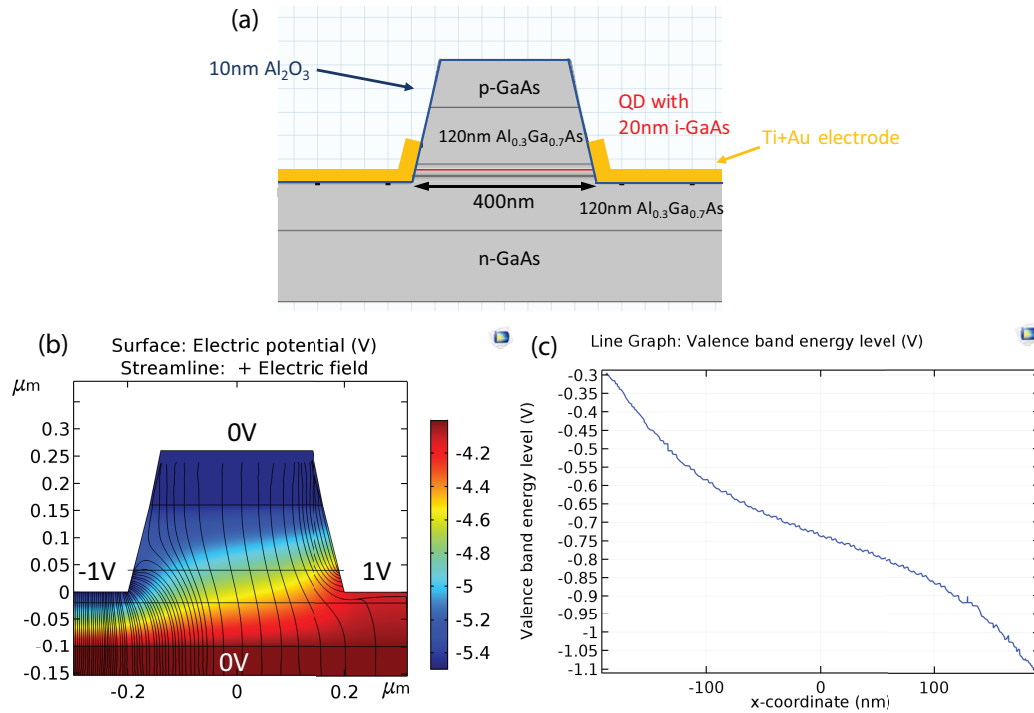
Figure 6.4: The design of the 4-electrode device (a) The cross-section geometry of the device (b) The electric field profile (Surface: Electric potential; Line: Electric field direction) with equal and opposite voltage on the two lateral electrodes, while grounding the top and bottom electrodes. (c) The band structure along the lateral cut-line (red line in (a)) where QDs are located.

In order to include the ability to charge a single QD electrically, an n-i-p diode structure in the vertical direction is needed. We design a 4-electrode device that can charge a single QD using vertical electric fields and simultaneously apply lateral electric

fields. The cross-section of the device structure is displayed in Figure 6.4 (a). The sample is grown on an n-doped substrate with back Ohmic contact (bottom electrode). We grow 120nm of $Al_{0.3}Ga_{0.7}As$ as a charge tunneling barrier and grow QDs on top of the AlGaAs. We then grow another 120nm of $Al_{0.3}Ga_{0.7}As$ and cap the sample with heavily p-doped GaAs. The p-doped layer is connected to a bonding pad far away from the QD location so that we have top-down optical access. Similar to the 3-electrode design, we create a 400nm wide mesa structure with a slight angle, and with the etched depth just below the QD level. After coating the mesa with a 10nm Al_2O_3 insulation layer, we can deposit the two lateral electrodes near the mesa sidewall using Ti and Au.

Figure 6.4(b) shows the electric potential (surface map) and electric field (line) in the device when we apply -1V on the left electrode, 1V on the right electrode, and ground the top and bottom electrodes. The natural n-i-p structure in the device creates a built-in field around 0.7V, resulting in the almost strictly vertical electric field lines across the mesa. To resolve the lateral electric field component, we plot the band-structure along the QD level as a function of x coordinates in Figure 6.4(c). An almost linear band-tilting of around 0.8eV across the mesa shows the formation of a uniform lateral electric field with the magnitude around 20kV/cm.

It is worth noting that this device design should still work if the $Al_{0.3}Ga_{0.7}As$ is replaced with intrinsic GaAs, although the strength of the lateral electric field might vary. The $Al_{0.3}Ga_{0.7}As$ is used to form an electron charging blockade so that a single hole can be deterministically charged into the QD. The advantage of using a p-doped layer on top of the mesa, rather than Ti/Au metal electrodes, is that the p-doped GaAs is conductive while transparent to NIR laser light. Therefore, a large number of interconnected mesa structures with optical apertures are much easier to pattern and fabricate.

6.4 Important Device Parameters

Choosing the proper device parameters is extremely important for applying a uniform lateral electric field across the entire mesa. Here, we will briefly discuss the device performance due to the influence of the background doping level, mesa size, and lateral electrode sidewall coverage. Primarily, we will focus on the strength and uniformity of the lateral electric fields.

6.4.1 Background Doping Level

Having background doping in MBE-grown intrinsic GaAs is common. The level of the background doping affects the Fermi level, the depletion width, and the band-bending significantly. To create a device with a uniform electric field across the mesa, we want to minimize the level of the background doping in intrinsic GaAs so that the intrinsic GaAs behaves like an insulator.
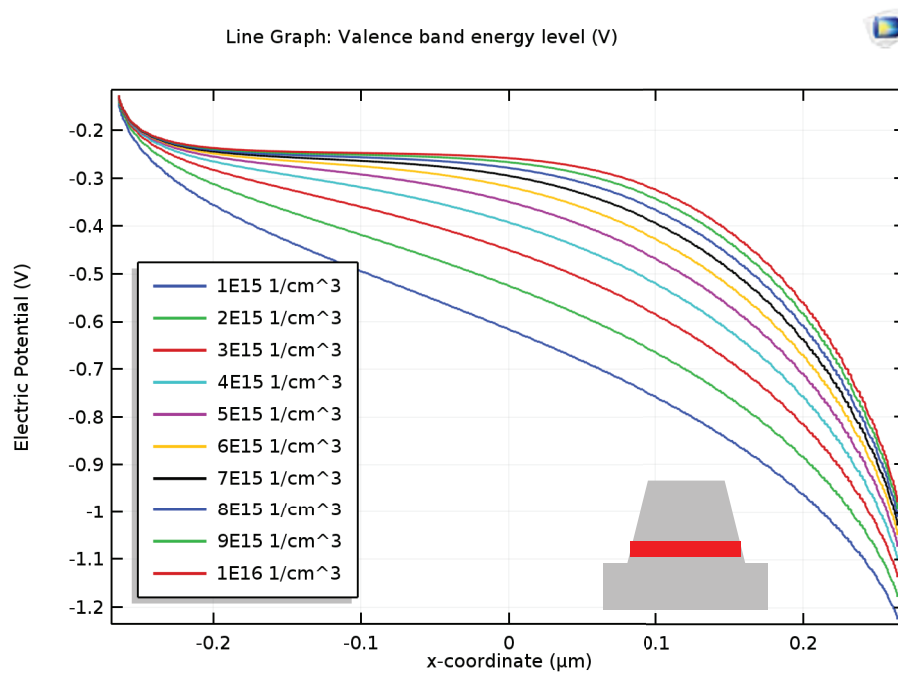
Figure 6.5: Band-bending across the cutline (insert) under lateral bias as a function of the background doping level.

To understand the potential consequences of unintentional doping, we use the 3-Electrode model and calculate the electric potential of the device with different unintentional p-type background doping. We apply -1V to the left electrode, +1V to the right electrode, and ground the top electrode to create a lateral bias. Figure 6.5 shows the band structure along the lateral cut-line of the mesa, where the QDs are grown. At a background doping level of $10^{15}/cm^3$, there is minimum band-bending across the mesa and the band-structure roughly follows a straight line, implying the desired semi-uniform lateral electric field. As the doping concentration increases from $10^{15}/cm^3$ (blue) to $10^{16}/cm^3$ (red), the band-bending becomes more and more significant. At $10^{16}/cm^3$, there is almost no electric field on the left side of the mesa, and the electric fields are mostly concentrated on the right side near the electrode. A similar result can be expected in the 4-electrode design. A qualitative explanation is that higher doping decreases the depletion width of the material, thus inhibiting the penetration depth of the electric field. Higher doping also pushes the Fermi-level closer to the conduction band edge or the valence band edge, thus changing the band alignment in the metal-insulator-semiconductor interface. In most cases, a low doping of order $10^{15}/cm^3$ is required to apply uniform lateral electric fields.

6.4.2 Lateral Electrode Side Wall Coverage

Another important parameter that impacts the strength of the lateral electric field is the coverage of the lateral electrode on the mesa sidewall. We compared two device models: 1. The mesa side-wall is partially covered by the lateral electrodes, 20nm above the QD level. 2. There is a 50nm gap between the mesa sidewall and the two lateral electrodes. The models are shown in Figure 6.6(a) and (b), respectively.

Similar to previous studies, we apply -1V on the left electrode, +1V on the right electrode and ground the top electrode in both models. We then calculate the lateral electric field strength along the lateral cut-line at the QD level. The device with lateral electrodes covering the mesa sidewall shows a lateral electric field around $1.5 \times 10^6 V/m$, as shown in Figure 6.6(c). In contrast, as shown in Figure 6.6(d), the
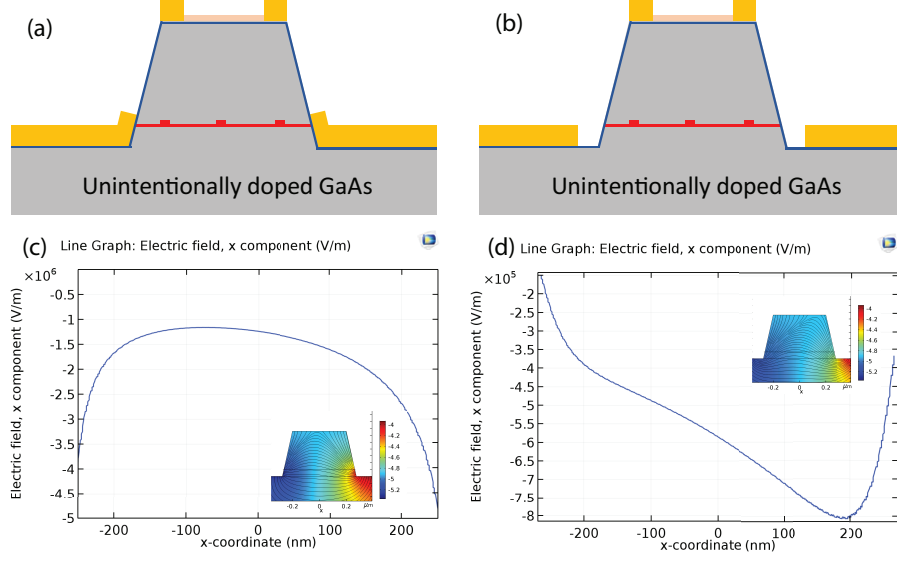
Figure 6.6: Device models with different lateral electrode profile. (a) lateral electrodes covers the bottom of the mesa sidewall. (b) Device with a 50nm gap between the lateral electrodes and the mesa sidewall. (c) and (d) The lateral electric field in model (a) and (b) while applying a lateral bias and grounding the top electrode, respectively. The insert of (c) and (d) shows the electric potential surface map in these two models.

device in which lateral electrodes do not cover the sidewall has a lateral electric field around $5 \times 10^5 V/m$, 2 to 3 times smaller than the former case.

Although it imposes additional constraints during device fabrication, having sidewall coverage of the two lateral electrodes is worth exploring if we want to apply large lateral electric fields. However, it is not hard to imagine the downside of covering the entire mesa sidewall with lateral electrodes. Such coverage would significantly increase the probability of short circuits between the two lateral electrodes and the top electrode, and would also impact the magnitude of the vertical electric field we can apply. Hence, partial sidewall coverage is optimal for the 2-D field applications. In our simulations, we find that device models with lateral electrodes covering to just above the QD level give the best performance in applying both vertical and lateral electric fields.

6.4.3 Vertical Bias or Current
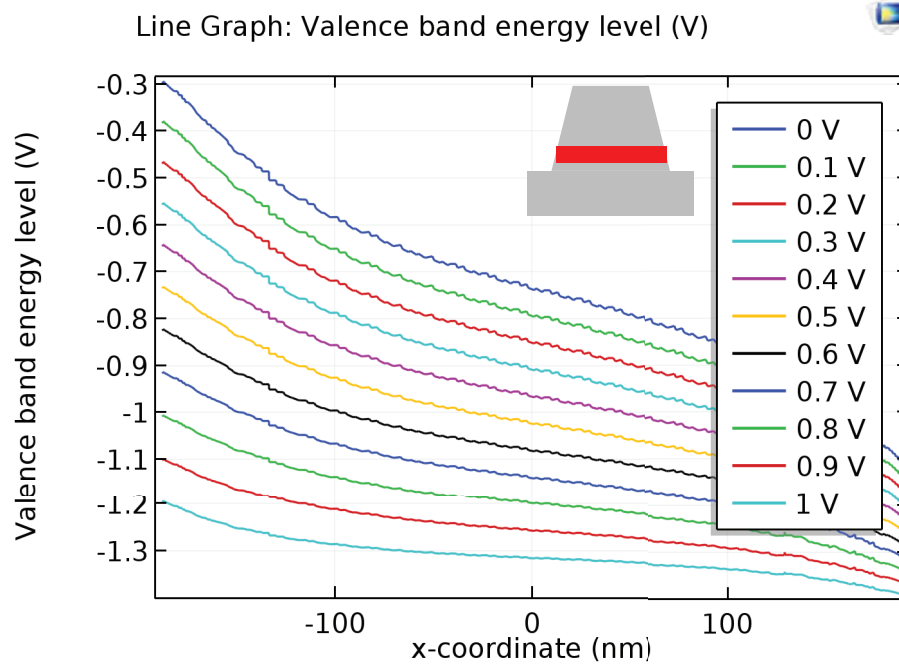
Figure 6.7: The valence band energy level along the QD cut-line (insert) in the 4-electrode device with a $\pm 1V$ lateral bias and different top electrode voltages, while grounding the bottom electrode

Last but not least, the vertical bias or current also affects the formation of the lateral electric field. Although this is not obvious in the 3-electrode device, it significantly impacts the device performance in the 4-electrode device. To understand this effect, we calculate the band structure of the 4-electrode device when we ground the bottom electrode, apply -1V on the left electrode, +1V on the right electrode, and a variety of positive voltages on the top electrode. We plot the valence band energy level along the QD lateral cut-line in Figure 6.7, as a function of the lateral coordinate x. As the top bias increases from 0V to 1V, the band-tilting becomes smaller and smaller, indicating a decrease in the lateral electric field.

A possible explanation for this effect is that the increase of vertical current, as we increase the vertical bias, changes the carrier concentration in the mesa. At 0V vertical bias, the current is at a minimum, as a result of the built-in bias from the n-i-p

diode structure. As we increase the vertical bias, the vertical band-structure becomes closer to a flat band and eventually reverses so that electrons can easily move from the n-doped layer to the p-doped layer. The extra electrons in the intrinsic layer change the charge concentration and thus the depletion width and band-bending along the lateral direction. Therefore, to observe the 2-D electric field effect in the 4-electrode device, we will need to keep the vertical bias as low as possible.

6.5 Conclusions and Discussions

In this chapter, we presented 2 device designs in an InAs QD system that can apply both vertical and lateral electric field. The first one contains 3 electrodes, patterned on an unintentionally doped GaAs matrix; the second one contains 4 electrodes, patterned on a vertical n-i-p structure. Both of them are able to apply uniform vertical electric field around 30kV/cm and semi-uniform lateral electric field around 20kV/cm under moderate biases. We further discussed how the strength and uniformity of lateral electric field changes with a variety of device parameters. Ideally, we'd like to have a device fabricated on a low $10^{15}/cm^3$ unintentionally doped GaAs matrix, with moderate sidewall coverage of the mesa and operate the device under the reverse vertical bias (low current) condition.

Chapter 7

NANOFABRICATION METHODS

To properly fabricate the devices designed by our COMSOL simulation, we need tools that help us generate sub-micrometer-scale lithography patterns with alignment errors for each lithographic step less than 50nm. We also need proper pattern transfer techniques that define the electrodes and the mesa structure. Furthermore, we need proper packaging techniques that accommodate our characterization instrument (cryostat). In this chapter, I will briefly describe some of the important techniques we use in our device fabrication.

7.1 E-beam Lithography

Lithography techniques, which define the pattern on the resist, are the most important part of the nanofabrication because all the sequential pattern-transfer steps (etching, deposition) depend on the properties of the resist. The accuracy of the lithography determines the critical dimension of the device pattern, and many techniques have been deployed in the industry to reduce the critical dimension to a quantum scale. Although mask-aligner photolithography generates very high throughput and is easy to use once a good recipe is established, achieving alignment precision that's better than 500nm is almost impossible. Furthermore, modifying the pattern design requires new masks to be fabricated, making photolithography costly and less versatile if the engineering process requires multiple device design iterations. Therefore, we will use e-beam lithography for our resist patterning because of its high alignment precision (+-5nm) and versatility of pattern definition.

We will introduce three aspects of e-beam lithography: 1. The e-beam lithography tool. 2. The pattern data preparation and job preparation. 3. The resist process techniques.

The e-beam lithography tool at the University of Delaware nanofabrication center can generate electron beams with 100kV acceleration voltage and maintain a beam diameter as small as several nanometers. This offers substantial advantage over other e-beam lithography tools which is modified from a scanning electron microscope, which usually have a maximum acceleration voltage of 30kV. High energy electron beams will penetrate resist (carbon based polymer) deeper (almost undeflected) than low energy e-beams, which results in an exposed e-beam resist with almost straight side walls. This resist profile has many advantages in the pattern transfer process. For instance, it can be used to create etching patterns with extremely high step contrast. During the writing, the electron beam is deflected using magnetic fields generated from electron optics. The maximum area the electron beam can be deflected is called the main-field. After finish writing on a main-field, the stage will move to the next one and the pattern will be stitched together. Properly managing the main-field writing and stage movements is very important to achieve a high writing precision.

To properly execute an e-beam lithography job, the pattern has to go through multiple preparation steps so that the e-beam tool can recognize it. The first step is the data preparation. It includes: 1) Pattern healing and extraction, which defines pattern sizes and removes overlaps, bad spots, sometimes even adding bias/subtractions; 2) Proximity effect correction, which gives the pattern proper dose factors according to its shape, in order to compensate for the back-scattered electrons from the substrate; 3) Fracturing, which reduces the shape of the pattern to rectangles and trapezoids, because these are the only two shapes the e-beam tool accepts. Fracturing also calculates how the e-beam/wafer should travel when writing a pattern. This step is very important when writing sub 300nm features that have curves, for instance photonic crystals. The second step is the job preparation, in which the prepared data file is sent

90

to the machine and the parameters of the lithography are calculated. These parameters include wafer locations, heights, alignment markers, base doses, and repetition of patterns.

A good e-beam lithography process also needs a reliable wafer process flow. This flow includes wafer preparation, resist coating, baking, and development. The process usually starts with cleaning the wafer using low-power O_2 plasma. Depending on the resist and wafer type, applying adhesion layers might be necessary before the resist coating. Then the resist will be uniformly spun on the wafer using spin-coating. As an estimation, the resist thickness is inversely proportional to the square root of the spin speed. After the e-beam writing, the resist needs to be developed to form the pattern. The developing time for each resist and pattern can vary. And it is a common practice to over develop the resist to guarantee clearing the exposed (unexposed) area for positive (negative) resist. Many parameters can affect the entire processing outcome, such as temperature, time, resist adhesion, etc. One thing to emphasize is that there are likely more than one set of parameters that will make the process work, but a good process parameter set should leave large room for error. For example, a 10s development time process is much harder to control compared to a 60s development time process.

7.2   ICP-etching

Etching is a pattern transfer technique that removes materials on the wafer that's not covered by resist. There are two types of etching commonly used in nanofabrication: wet-etch and dry-etch. Wet-etch uses liquid-phase chemicals (acid, base, organic solvent) to react with the wafer and dry-etch uses plasma phase chemicals instead. Among dry etching techniques, reactive-ion etching (RIE) and inductively coupled plasma (ICP) etching are two commonly used techniques. We will focus on introducing ICP etching in this section.

ICP etching uses inductively coupled plasma to chemically and physically remove materials on the wafer. Compared to RIE etching, ICP etching generates higher

density plasma with significantly reduced ion bombardment, which reduces the polymer by-product after the etching process. The key difference between ICP etching and RIE etching is the separate ICP RF power source connected to the cathode which generates a DC bias and attracts ions to the wafer. This decouples the ion current and ion energy applied to the wafer, broadening the process window.

A typical ICP etching process contains both chemical etching and physical etching (ion bombardment). For example, to etch GaAs, Cl based gases (BCl_3 or Cl_2) are used to react with the substrate and inert gases such as Ar are used to provide ion bombardments. The chemistry of the reaction is shown in equation below:

$$GaAs + BCl_3 \rightarrow GaCl + B_2 + As_2 + As_4 \tag{7.1}$$
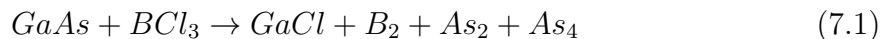
With proper chemistry, good selectivity can be achieved between different materials such as SiO_2 and GaAs. Besides choosing the etchant that's appropriate for the material system, there are many other parameters that affect the result of the etch. For instance, plasma power during the ICP etching defines the ion density and therefore the etch rate. The extra DC bias power that drives ions to the wafer can significantly influence the side wall profile of the etched product. Other parameters such as the chamber pressure, the sample temperature and the chemistry etching/physical etching ratio also influence the process to a certain degree.

In addition to carefully fine tuning machine parameters during the ICP etching, resist selection is equally important in creating reliable etching recipes. Resists, which serve as the pattern transfer layer, protect the sample underneath from being damaged by the ICP. Because resists also get damaged by the ICP, choosing the right thickness of resist is crucial. If the resist is too thin, surfaces and side walls of the sample might get exposed to the etchant, leading to undesired etched shapes. However, if the resist is too thick, the etch gases might not be able to reach the sample completely, which results in incomplete etching. The resist also needs to be removed from the sample after the ICP etching. This is a common problem for many polymer-based resists. As a result of intensive Ion bombardments and chemistry reactions, some processes could

create polymer by-products that adhere to the surface (sidewall, top) of the sample. High-power Oxygen plasma or other removal agents are required if the polymer cannot be removed completely by tradition removal solvents such as aceton or NMP. Another way to avoid polymer-removal is by using a hard mask instead of a resist mask. For example, we can use patterned SiO_2 as the mask to etch GaAs. The SiO_2 can then be removed by HF solution, which does not etch GaAs.

7.3   E-beam Metal Deposition Tool

Metal deposition is another key aspect of nanofabrication. Metals are commonly used as electrodes, optical apertures (metals are optically opaque), and etching masks. Metal deposition is usually done in a high-vacuum chamber, using an electron beam metal deposition tool or a thermal deposition tool. The e-beam metal deposition tool uses accelerated electron beams to heat metal sources and evaporate them onto the sample. The electron beam is usually accelerated to several 10kV to bombard the source metal. The high kinetic energy from the electron beam is converted to thermal energy and causes the metal to melt or sublimate. Electron beam sources are typically ramped up(down) slowly to make sure the heating(cooling) process does not damage the metal crucible. Usually, circular or elliptical shaped electron beam scanning patterns are used to insure the metal melts or sublimates uniformly.

The evaporation process from a metal source covers a wide angle and thus the entire chamber will be coated during the deposition. That being said, the deposition process for electron beam evaporation is still highly directional, because the distance between the sample and the source is far. The angle of the deposition can be changed by changing the tilt and rotation angle of the wafer with respect to the metal source. Angled e-beam deposition is commonly used in many fabrication processes, and we will continue our discussion on this topic later in the device fabrication chapter.

7.4 Dielectric Deposition Tool (PECVD,ALD)

All integrated circuit fabrication requires proper insulating layer depositions. Typical insulating materials, such as SiO_2, Si_3N_4, Al_2O_3, are dielectrics with a high resistivity. They are usually deposited on the wafer using chemical reactions. We will introduce two commonly used dielectric deposition methods: Plasma enhanced chemical vaper deposition (PECVD) and atomic layer deposition (ALD).

PECVD uses plasma induced chemical reactions for dielectric depositions. Si based dielectric is usually deposited by PECVD. Using SiH_4 and N_2O, the chemical reaction to form SiO_2 can be written as:

$$SiH_4 + N_2O \rightarrow SiO_x + H_2 + N_2 \qquad (7.2)$$
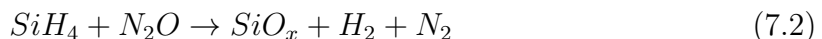
With proper gas compositions, the deposited SiOx can have almost perfect stoichiometric ratio and serves as a great dielectric insulator. However, because the reaction of SiO_2 deposition happens in the chamber and not on the surface of the sample, the coating is usually not 100% conformal. Moreover, defects in SiO_2 deposited by PECVD, such as pin-holes, result in low breakdown voltages less than 1MV/cm that degrade the performance of the device. Therefore, hundreds of nm thick SiO_2 films are required to provide good insulation.

ALD uses gas phased chemical precursors to react with the surface of the material one at a time in a sequential self-limiting manner. Unlike PECVD where all reacting chemicals are present in the chamber at the same time, precursors in ALD are introduced into the chamber separately. Once all the reactive sites on the surface are consumed, the reaction stops and precursors are purged away before the next precursor is added. Therefore, the material is deposited on the surface one atomic layer at a time, resulting in a high precision, uniform thin film coatings on the substrate. The Al_2O_3 deposited by ALD usually has breakdown voltage exceeding 5MV/cm, much better than the PECVD grown dielectrics.

In our research work, we also use plasma enhanced ALD rather instead of conventional thermal ALD. In conventional thermal ALD, the energy required for chemical reaction on the surface is provided only by the heated substrate. In plasma enhanced ALD, energy required for chemical reactions can be provided by the plasma, resulting in a much lower process temperature. Additionally, plasma enhanced ALD usually results in better films and more conformal coating of the surface.[121]

Chapter 8

DEVICE FABRICATION

In this chapter, I will first briefly introduce the fabrication recipe development efforts we made before the device design change. I will then describe the fabrication recipes for the 3-electrode device without insulator. I will discuss additionally recipes that can be used in the insulator fabrication and the 4-electrodes device.

8.1 Background

We started our device fabrication on VGF grown GaAs samples and QD samples using the device structure designed by Xinran Zhou et al.[120]. However, we were unable to observe any Stark shift or charging effect in either lateral or vertical voltage configuration. We then progressed through several interations of device fabrications before the design change. Unfortunately, none of them gave us any reliable result that shows the control of 2-D electric field. These setbacks pushed the new design simulations using the semiconductor module, and narrowed down our design parameters as discussed in the previous chapter.

Some key fabrication processes of the previously designed sample are shown in Fig8.1. After we grow the QD sample on a p-doped substrate using MBE, we deposited NiGeAu alloy on the back of the sample, and anneal it using RTP to form the backside Ohmic contact. We then etch a cylindrical-shaped mesa on top of the sample, using Cl_2 ICP and a PECVD grown SiO_2 mask. Then we grow another 100nm of SiO_2 using PECVD, to form the insulation layer. Then two lateral electrodes are deposited next to the mesa using e-beam metal evaporation. After that, another 300nm thick SiO_2 layer is deposited on top of the device using PECVD, to protect the lateral electrodes.
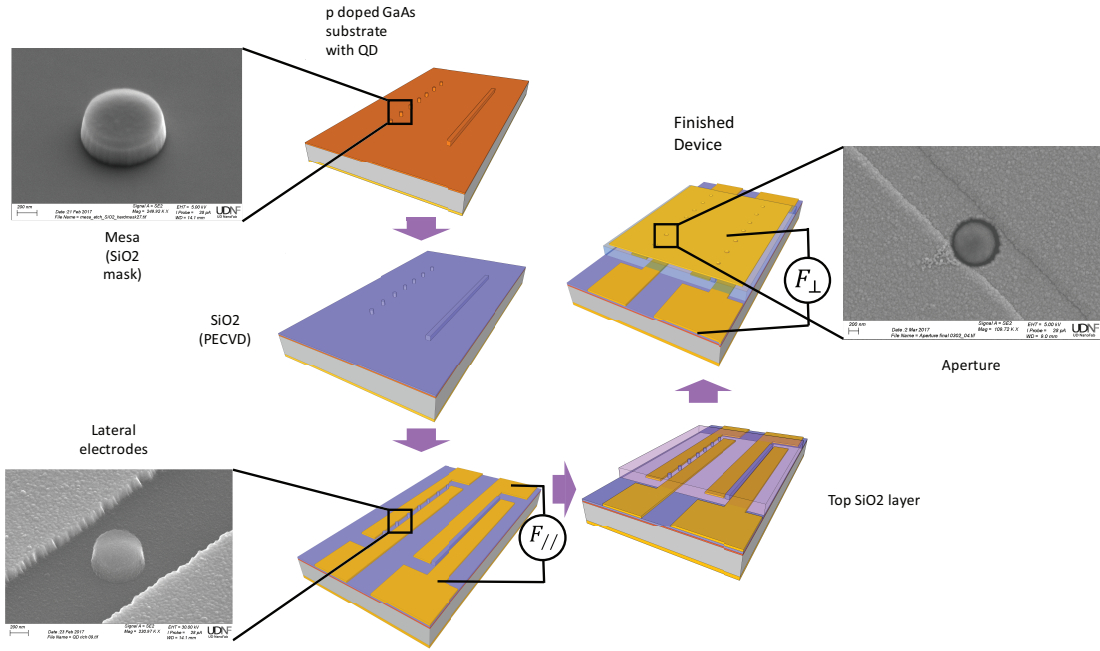
Figure 8.1: Fabrication process of a 4-electrodes device with the device structure similar to Xinran's structure[120].

To finish the device, we deposit Au electrodes with um size optical apertures that align with the mesa.

The initial characterization of this device shown no Stark shift or charging of a single QD in any bias configurations. To make things better, we fabricated devices using the same geometry with several improvements: 1) Replacing the SiO_2 layer with Si_3N_4 due to its higher dielectric constant and better conformal coating; 2) Reducing the insulator thickness covering the mesa to 20nm, and eliminating the top insulation layer and deposit apertures on top of the mesa. Although we did observe vertical stark shifts using improvement 2), unfortunately, we didn't observe any photoluminescence features that correspond to lateral electric fields control in a single QDs.

The upside of this experience is that we were able to establish many nanofabrication processes that can be directly transferred or modified for future device fabrication. For example, we established different ICP recipes that can be used in GaAs etching,

SiO_2 or Si_3N_4 etching. We also developed by-layer resist lift-off recipes that can handle up to 250nm-thick metal lift-offs. These efforts turned out to be very useful in all of our future recipe developments.

8.2 3-electrodes Fabrication in an Intrinsic GaAs Matrix

In this section, I will describe our fabrication process for the 3-electrode InAs QD/QDM device whose design was described in the previous chapter. I will focus on the 3-electrode InAs QD/QDM device with Schottky metal contacts, as a first step device to validate our simulation model. I will then introduce additional fabrication recipes for the insulator-gated device and the 4-electrode InAs QD/QDM device.

8.2.1 Sample Growth

The sample was grown on a 500um GaAs (001) intrinsic substrate using the OSEMI NextGEN solid source MBE equipped with effusion cells of In, Ga, and a two-zone valved As cracker source. Beam equivalent pressure (BEP) of Ga, In, and As2 is monitored by an ionization gauge. The growth temperature is measured by band edge thermometry (BET). We wait until the desorption of the native oxide on the GaAs wafer with substrate rotation under 1E-5 Torr As2, and over-pressure at $620°C$ for 10 min until a clear and a streaky 2x4 RHEED reconstruction was observed. Then the substrate temperature was lowered to $550°C$ and a layer of 600nm unintentional doped GaAs was grown at 1.9557 Å/s. The growth was then interrupted with the substrate rotation being stopped, in order to achieve a non-uniformly distributed QDs density. Additionally, the substrate temperature was lowered to $520°C$ and the As2 BEP was cut by half. Once the growth temperature and As2 BEP are stabilized, approximately 1.72 ML InAs was deposited at 0.035 ML/s, followed by the deposition of 2.7nm GaAs partial capping layer to set the truncation height of the InAs QDs. Afterward, the As2 BEP was increased to 1E-5 Torr again and the sample was annealed at 580 °C for 70s to evaporate the exposed In atoms beyond the truncation height. Finally, a 250nm unintentionally doped GaAs layer was grown.

We performed Hall effect measurements to study the film's resistivity, doping type, doping concentration, and carrier mobility. The as-grown film has a p-doping density of 5.28E16 cm^{-3}. The bulk resistivity is 2.635 $\Omega \cdot cm$ and the mobility is 44.84 cm^2/Vs. We also performed low-temperature PL on the whole film before device fabrication and confirmed the successful growth of InAs QDs with the desired height: sharp peaks were observed in the wavelength range of 940nm to 960nm in PL spectroscopy. The QD density is close to 10 to $100/\mu m^2$, and we are able to isolate single QDs by using ebeam lithography to pattern apertures as small as 200nm.

8.2.2 Alignment Marker
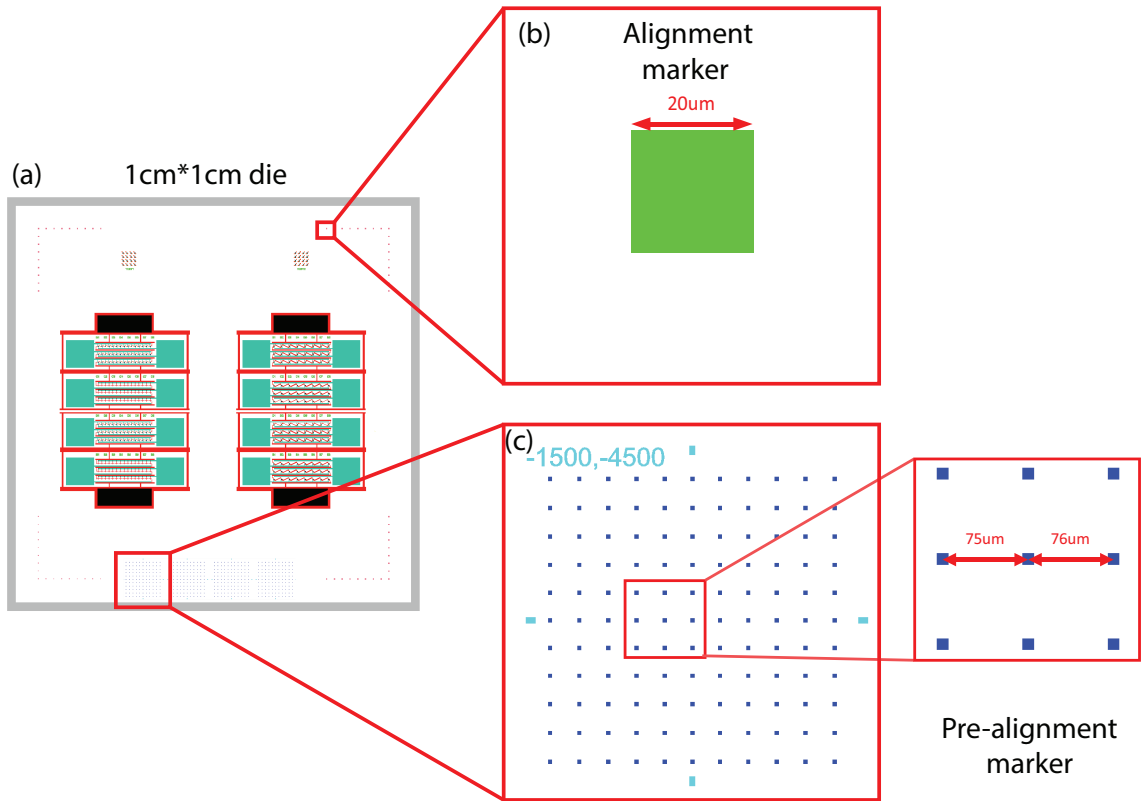
Figure 8.2: Top electrodes deposition process for 3-electrodes device. (a) Schematic of E-beam deposition using PMMA/MMA bi-layer resist. (b) Top view image of a deposited top electrodes using SEM.

Reliable alignment markers have to be fabricated prior to device fabrication,

so that each device layer can be aligned with nanometer precision. The marker pattern design that works with our e-beam lithography tool is shown in Figure 8.2. As shown in Figure 8.2(a), the device pattern is located at the center of the 1cm*1cm die. 20um*20um size alignment markers are patterned on the four corners of the die. Additionally, four blocks of pre-alignment markers are positioned at the bottom of the wafer. The pre-alignment marker arrays are composed of 10um*10um squares that are separated by a distance that depends on their relative location in the array. The e-beam tool will locate five cross-patterned pre-alignment markers and calculate their relative distance. Using this data, the e-beam tool can extrapolate the position of the markers in the pre-alignment array. Then the e-beam tool will move to the alignment markers' position near the corner of the wafer and start the alignment calibration.

The electron beam tool uses back-scattered electrons to determine marker positions, so creating good back-scattered electron contrast between the marker and the wafer is essential in fabricating high precision markers. Typical e-beam markers are composed of either metal materials with high-atomic numbers or deep-etched pits. In our device, we use a lift-off process to fabricate Au metal markers. The exact fabrication process is the same as the top-electrode lift-off process, which we will introduce in section 8.2.4.1.

8.2.3 Pattern Layout

The device pattern is designed to accommodate our device packaging holder, optical characterization setup and the cryostat. As shown in Figure 8.3(a), each 1cm*1cm die has two 3mm*5mm big blocks. Each block consists of four segments with eight lateral electrodes (green) and two vertical electrodes (red and black). The enhanced view of the top two segments on the left block is shown in Figure 8.3(b). In each segment, there are 45 3-electrodes device units as shown in Figure 8.3(c)(d)(e). The top electrodes (orange and dark green) are threaded through the entire segment in series and connected to the bonding pad through wired areas (red). The lateral electrodes (purple) are structured around the top-electrodes and connected to the bonding pad
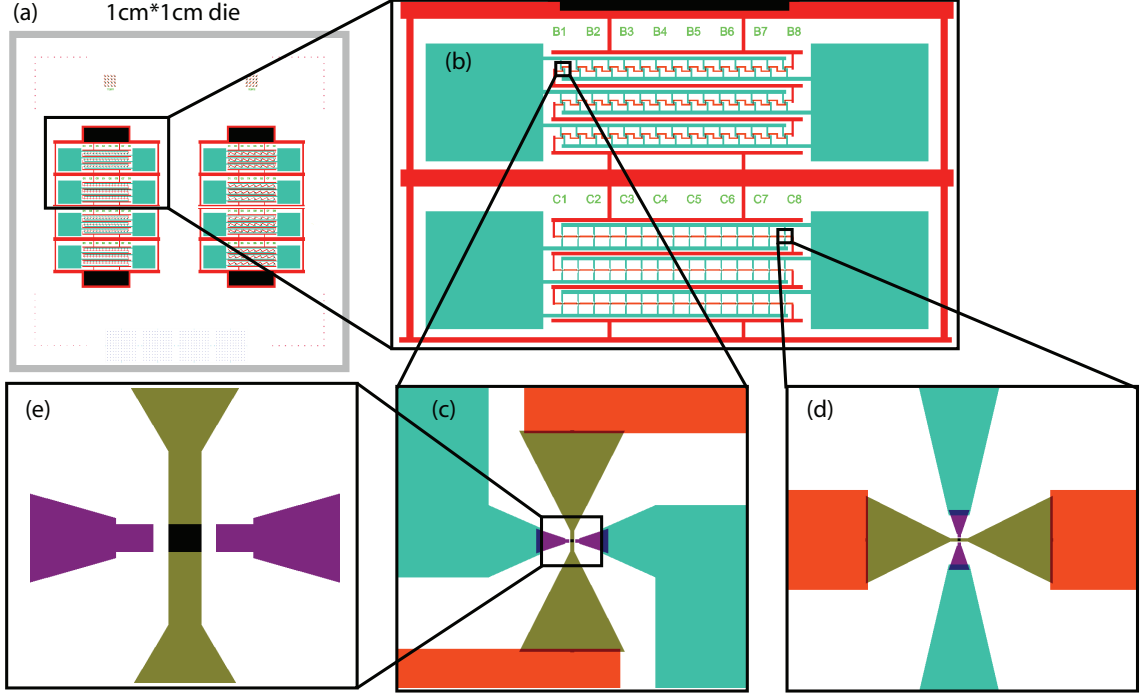
Figure 8.3: Top electrodes deposition process for 3-electrodes device. (a) Schematic of E-beam deposition using PMMA/MMA bi-layer resist. (b) Top view image of a deposited top electrodes using SEM.

in parallel. An optical aperture (black in (e)) can be fabricated on the top electrode for out-of-plane optical access. The size of the pattern is adjusted throughout the fabrication and should match the simulation model.

8.2.4 Top Electrodes with the Aperture

8.2.4.1 E-beam Deposition

After the marker fabrication, the wafer is cleaned using low power oxygen plasma ashing for 5 minutes. We use a lift-off process to fabricate the top electrodes, as sketched in Figure 8.4(a). The wafer is first spin-coated with 15 nm of adhesion promoter AR300-80 at 4000rpm and baked on a hot plate at 170°C. Then 250nm MMA resist is spun at 6000rpm and baked for 2 minutes at 170°C, followed by 180nm of PMMA resist spun at 6000rpm, and baked for another 2 minutes at 170°C. Because

the MMA copolymer develops faster than PMMA, this process forms an undercut bi-layer resist structure. This structure helps create a gap between the deposition metal layer and lift-off layer, reducing lift-off edge defects such as flagging or incomplete lift-off. The resist is then exposed with the electron beam at a base dose of $330\mu J/cm^2$. We use MIBK:IPA 1:1 solution and develop the resist for 90s at room temperature.

The patterned resist structure is characterized using the optical microscope and the SEM to make sure the dimension is within our tolerance, and the exposed area is clean. The average exposed top-electrodes pattern width is around 400nm, which is close to the pattern size.

The wafer is then cleaned with low power oxygen plasma for 10s before E-beam metal deposition. We first deposit 15nm of Ti at 4Å/s as an adhesion layer, then deposit 110nm of Au at 5Å/s. Next, we soak the sample in NMP solution at $80°C$ for 20 minutes to strip the resist. The sample is then cleaned with ultrasonic and IPA before taken out of the solution and blow-dry with Nitrogen gas. The thickness of deposited metal is measured using a profilometer and found to be $125nm \pm 5nm$. The SEM picture of a 400nm wide lift-off top electrodes is shown in Figure 8.4(b), with a dimension close to our pattern size. The texture on the metal contact is a result of the Au's grain size, which is typically around 20nm to 50nm.
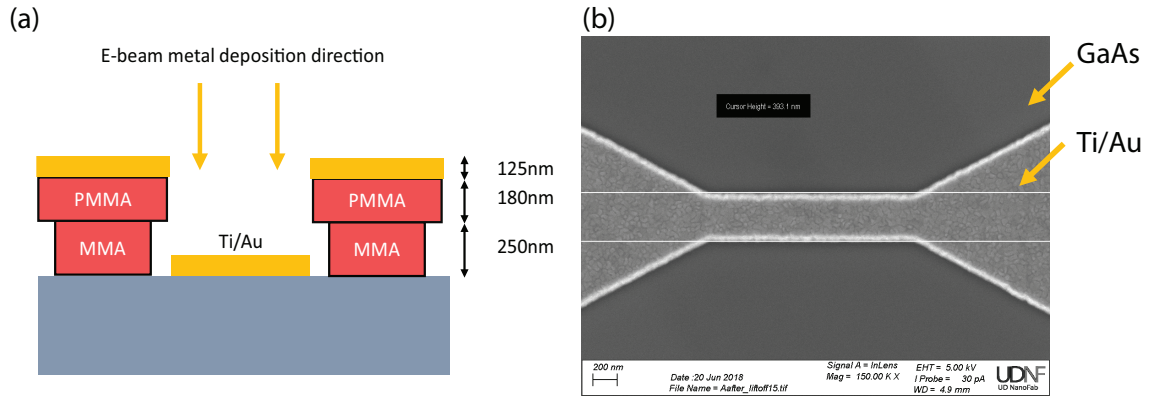
Figure 8.4: Top electrodes deposition process for 3-electrodes device. (a) Schematic of E-beam deposition using PMMA/MMA bi-layer resist. (b) Top view image of a deposited top electrodes using SEM.

8.2.4.2   Ion mill Aperture

To etch the aperture on the top metal electrodes, we used an Ion mill etching process that has a high contrast in etch rate between Au and Ti.[122] The resist we use is a ZEP520 type positive resist due to its high dry etch resistance comparing to PMMA. The wafer is first cleaned with oxygen plasma and coated with a thin layer of adhesion promoter. Then AR6200.09(CSAR) resist is spin-coated at 4000rpm and baked at 170∘C on a hot plate for 5 minutes. The thickness of the resist is 180nm. After resist coating, we exposed the resist with the aperture pattern at a base dose of $160\mu C/cm^2$. The resist is then developed with AR600-546 for 90s and rinsed in IPA for 30s before blow-drying with nitrogen.

We used two different Ion Mill Ar etching recipes to etch the metal and form the top aperture. The fast etch recipe uses 400V beam voltage and 55mA beam current to generate Ar plasma and 80V acceleration voltage for directional etch. The slow etch recipe uses 200V beam voltage and 22mA beam current with an acceleration voltage of 40V. The Au etch rate for the fast etch recipe and slow etch recipe is 30nm/mins and 5nm/mins, respectively. The erosion rate of CSAR resist with the fast etch recipe is around 10nm/min, calibrated using a scratch test. Based on the relative power of the two recipes, the erosion rate of the slow etch recipe is estimated to be less than 1nm/min. To etch away most of the Au without drilling into GaAs, the sample is first etched with fast etch recipe for 3 minutes and 20s, then slow etched for 2 minutes and 30s. Because of the high etch-rate difference between Au and Ti, the etching will slow down drastically or stop when all the Au is etched away. The GaAs underneath will be protected by the thin Ti layer.

The post-etched sample is then soaked in NMP at 80∘C for more than 5 hours and cleaned in an ultrasonic bath for 30 minutes. After rinsing in IPA and nitrogen blow dry, the etched aperture is characterized by SEM, as shown in Figure 8.5(b). The sidewall around the aperture guarantees the electrical continuity, and the depth of the aperture in angled view indicates an almost clear aperture without Au metal.
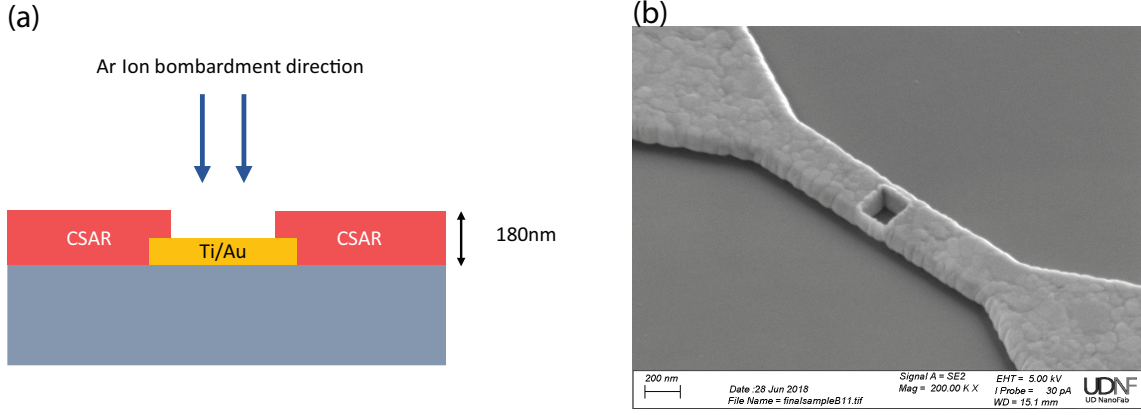
Figure 8.5: Top aperture fabrication process for 3-electrodes device. (a) Schematic Ion mill using CSAR (ZEP520) resist. (b) Angled view of one top aperture after fabrication.

8.2.5 Mesa Etching

We use ICP dry-etch with a resist mask to etch the mesa. The mesa etching schematic is illustrated in Figure 8.6(a). The wafer is first cleaned and coated with a thin layer of adhesion promoter, AR300-80. Then E-beam negative resist AR-7520.18 is spun at 4000rpm, followed by 60s hot plate baking at 85°C. The mesa pattern size is designed to be 20nm wider than the top-electrodes width so that the top-electrodes are protected from the ICP etching. The wafer is then exposed with electron-beam lithography at a base dose of $736\mu C/cm^2$. We used an AR300-47 4:1 H_2O solution to develop the resist at room temperature for 240s. The sample is then cleaned with oxygen plasma (descum) for 10s.

To create an etching profile with a slope for lateral electrodes deposition, we used 500W ICP power, 100W bias, 10sccm BCl_3 and 25sccm Ar. The etch rate for MBE grown GaAs is calibrated at 300nm/min and the erosion rate for ARN7520 resist is 100nm/min. The sample is etched for 68s to create a mesa height of 325nm. After that, the sample is soaked in an NMP solution at 80°C for 8 hours to strip the resist, including a 30mins ultrasonic cleaning time. The result from SEM characterization in Figure 8.6(b) shows a smooth sidewall etching profile, free of polymer by-products. The sidewall angle is measured in SEM to be around 15°. (see appendix)
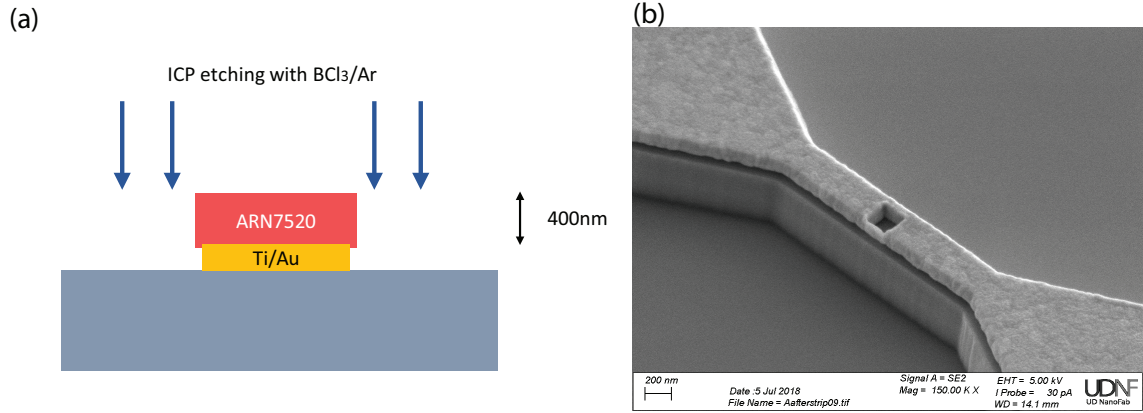
Figure 8.6: Mesa fabrication process for 3-electrodes device. (a) Schematic of ICP etching using BCl_3 and Ar (b) Angled view of one etched mesa using SEM

8.2.6 Lateral Electrode Deposition

The most critical part of the side gate fabrication is to have metal contact on the lower part of the mesa sidewall. The mesa has a slope of around 15°, and the sidewall width is 72nm on each side. Aiming for coverage between 1/5 to 1/3 of the sidewall, as designed, requires the e-beam lithography to have less than ±6nm writing and alignment accuracy. Although not impossible, this is extremely challenging and requires a long time for process engineering and calibration. Instead, we used angle metal deposition as sketched in Figure 8.7(a). The resist structure is a LOR undercut layer plus CSAR e-beam positive resist. The LOR's developer is an alkaline solution, other than solvent, allowing us to engineer each resist layer individually. The concept is to form an undercut bi-layer structure that's slightly wider than the base of the mesa (around 555nm). Using SEM, we can characterize the resist size and calculate exactly the angle that gives us the best sidewall coverage. This fabrication process requires much less rigorous resist writing procedure and can guarantee sidewall coverage of lateral electrodes if the SEM characterization and calculation is done accurately.

The fabrication process starts with sample cleaning using oxygen plasma and coating it with the adhesion promoter. Then, LOR 3A is spin-coated on the sample

at 6000rpm and baked at 200°C on a hot plate for 5 minutes. CSAR09 is then spin-coated at 2000rpm and baked at 170° for 5 minutes. The resulting resist thickness is around 150nm of LOR plus 250nm of CSAR. The sample is then exposed using EBL at a base dose of $190\mu C/cm^2$. The developing procedure is separated into two steps: 1) Develop CSAR with the AR600-546 developer for 60s, rinse with IPA and N_2 blow dry; 2) Develop the LOR layer using AR300-47 for 35s. This specific LOR recipe gives an undercut rate that's similar to the vertical developing rate, therefore resulting in an undercut resist profile of 150nm on each side, as indicated in Figure 8.7(a) (not to scale).
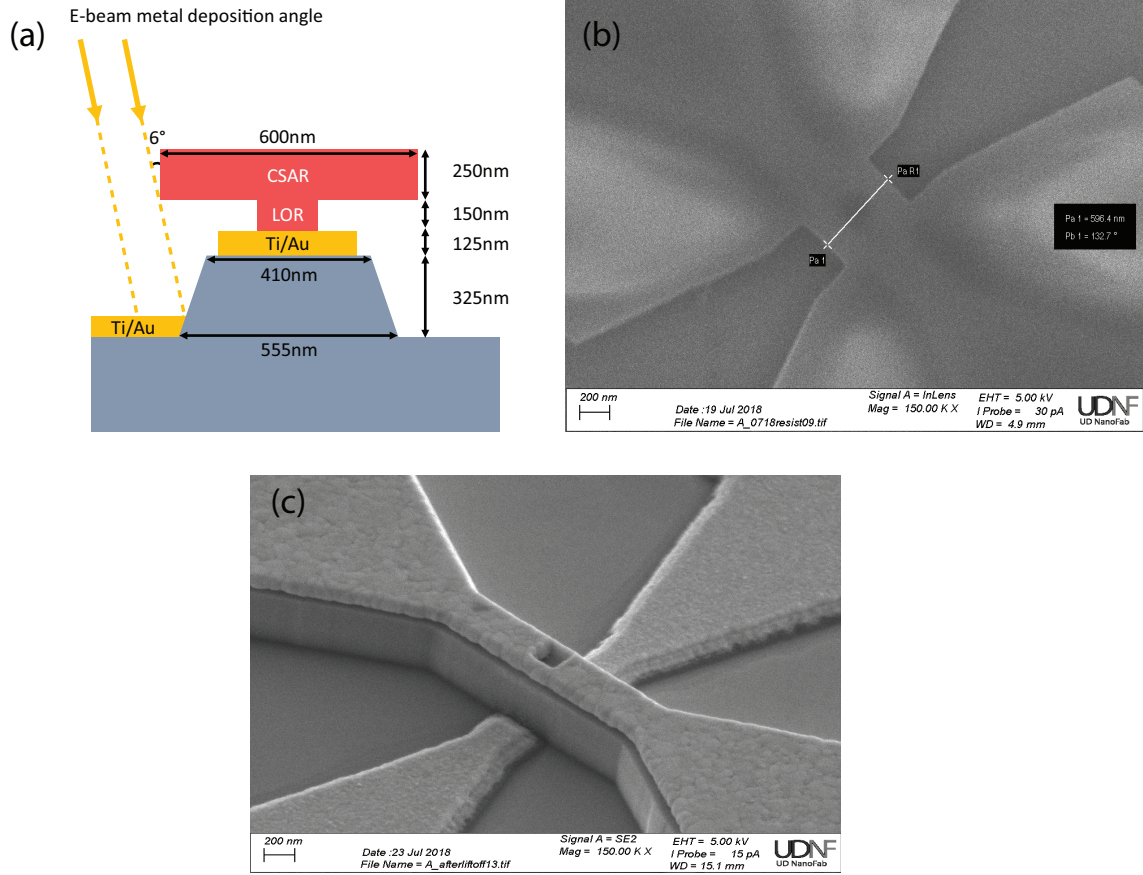
Figure 8.7: Lateral electrodes fabrication process for 3-electrodes device. (a) Schematic of angled metal deposition for sidewall coverage of the lateral electrodes. (b) Resist calibration shows CSAR width is 596nm. (c) the full lateral electrodes structure after lift-off.

The SEM calibration in Figure 8.7(b) shows that the CSAR width is around 600nm. Based on the geometry of the structure, we derived the angle that provides 1/4 sidewall coverage is 5.8°. However, the tilting precision of our e-beam metal deposition tool is 1°, which is why we use 6° in our actual fabrication. Based on this structure, a 0.2° variation could result in ±3nm variation in sidewall coverage, which is within our tolerance.

On a single device, we design lateral electrodes that are oriented in four different directions: (100),(010),(110),(-110). One pair of lateral electrodes in each orientation requires two separate angled depositions with 180° sample rotation. Therefore, a total of eight 6° angle depositions with different rotation angle are needed to fabricate one device. To avoid metal piling up, we deposit 10nm of Ti at 8 different rotation angles, then deposit 40nm of Au with the sample rotated at $40°/s$. The resulting structure has 120nm bulk lateral electrodes with 10nm Ti to cover the sidewall. Although the actual metal thickness on the sidewall is less than 10nm due to the non-orthogonal deposition angle on the sidewall, it should at the very worst put the lateral electrodes position in contact with the edge of the mesa. Figure 8.7(c) shows an SEM angled view of a pair of lateral electrodes after the lift-off, with a visible sidewall coverage at the bottom of the mesa.

8.2.7 Wire-Bonding and Packaging

After the side-gate metal deposition, the sample is diced into 3mm*5mm pieces and mounted on an integrated circuit die. We use thermal and electrical silver epoxy to bond the sample on the die and then cure it at 80° for 30 mins. We then bond the contact pad to the IC die using wire-bonding. The finished sample is shown in Figure 8.8. The sample is then mounted in the cryostat and ready for optical measurement.

8.3 Additional Fabrication Steps

In the previous section, we discussed the fabrication steps for the 3-electrode device when all 3 electrodes have Schottky contacts. We also fabricated a 3-electrode
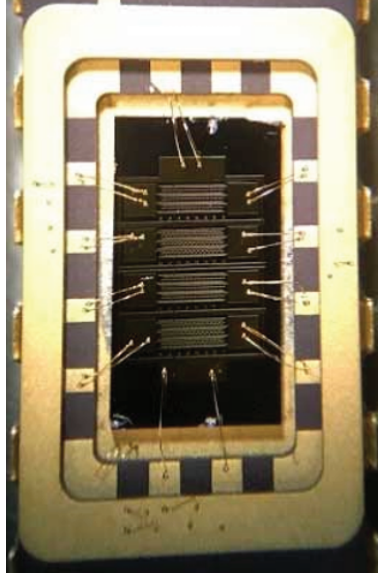
Figure 8.8: A post-nanofabrication 3-electrode sample mounted on an IC die, with Au wire bonded between the contact pad.

device with Al_2O_3 insulators between the two lateral electrodes and GaAs. The purpose of using the insulator is to prevent Fermi pinning and inhibit charging from the two lateral electrodes. To successfully include Al_2O_3 in the device, we introduce two additional fabrication steps:

1. 20nm of Al_2O_3 is deposited right after the mesa etching. We use plasma enhanced ALD for Al_2O_3 deposition since it allows low temperature processing instead of traditional ALD. We use Trimethylaluminium(TMA) as the Al precursor and O_2 plasma as the O_2 precursor. The deposition is carried out at 300°C with a deposition rate of 1nm per 9 cycles.

2. Because ALD deposition will coat Al_2O_3 conformally around the sample, the excessive Al_2O_3 on top of the bonding pad needs to be removed to allow wire-bonding. We spin 280nm of CSAR at 2000rpm and use e-beam lithography to define the pattern. Then we etch the Al_2O_3 away using Cl2 ICP etching. We use 700W ICP power with 20sccm of Cl2, 30sccm of Ar and 100W RF bias. The etch rate for Al_2O_3 is 33nm/min and erosion rate for CSAR is 220nm/min. The Al_2O_3 is clean after 45s of ICP etching

and the resist is stripped using hot NMP and Oxygen plasma ashing.

In the previous chapter, we also discussed a 4-electrode device that uses a back Ohmic contact. To fabricate the Ohmic contact, we use NiGeAu alloy with the thickness of 17nm/33nm/120nm. After e-beam evaporation, we use Rapid Thermal Process tool to anneal the contact at 410°C for 60s. This is an established Ohmic contact recipe created by previous group members. Other than this change, the process for fabricating the device with Ohmic contacts remains the same as that described here.

8.4 Discussion

We have discussed our fabrication process for the device presented in the previous chapter. However, the current process is not perfect. Several issues affect the yield of our fabrication, although they are not severe enough to cause device-level breakdown:

1. We are experiencing unusual alignment errors. We discover these alignment issues at the aperture etching stage when the aperture and the top electrodes are misaligned. We find the majority of the alignment error to be systematic across the sample, which is that the pattern is shifted by 50nm in the +x and 10nm in the +y direction. Moreover, the alignment error maintains its direction and magnitude through the entire fabrication. This indicates that the alignment error occurs at the top electrode fabrication step. Our hypothesis is that the error occurs because of metal migrating on GaAs due to poor adhesion and thermal processing. It is likely the migration happened to one of the markers used for aligning the top-electrode layer, which is why all the sequential steps are misaligned by the same amount. Luckily, after we identified the systematic alignment error, we were able to reduce the error significantly by shifting our pattern accordingly. The result is not perfect since we can't correct all the unsystematic errors. However, we are able to reduce the alignment error low enough so that it doesn't cause any device-level breakdown.

2. We also find that bonding to Ti/Au metal pad on oxide surfaces is much harder than on GaAs surfaces. This is a well-known issue because the adhesion of Ti

to oxide is not as strong as Ti to GaAs. The solution is to find the bonding parameter threshold just in between ripping off the bonding pad and leaving zero marks on the bonding pad. We find this parameter set usually requires lower temperature (70°), almost zero ultrasonic strength and medium force. Another way to solve this problem is to use silver epoxy. Although bonding a 5mm*5mm pad with epoxy is extremely hard by hand, it's not impossible with enough practice.

3. Another common problem with our process is the base developer for PMGI and UV5 resist, such as LOR and AR7520. We find that the base developer tends to react with GaAs and etches its surface. Although the etch rate is extremely slow, it will cause damage to the GaAs substrate and affect the quality of deposited metal markers. It will also react with AlGaAs layers much faster than GaAs substrate. Therefore, a different resist needs to be used to fabricate GaAs samples with AlGaAs.

Chapter 9

OPTICAL CHARACTERIZATION METHODS

9.1 Wafer Imaging

The lowest QDs density achievable during the MBE growth is around $1\ \text{QD}/\mu m^2$, as limited by the QD nucleation threshold. During the MBE growth of the QDs, the wafer rotation can be stopped temporarily so that the QDs nucleate with a density gradient. In this case, part of the wafer where the density is too low for QDs to nucleate will have no photoluminescence (PL) from the QDs. Finding the threshold of QDs photoluminescence on the wafer can help us locate the part of the wafer that has a low QD density suitable for device fabrication. We use the wafer imaging technique to find the PL threshold.
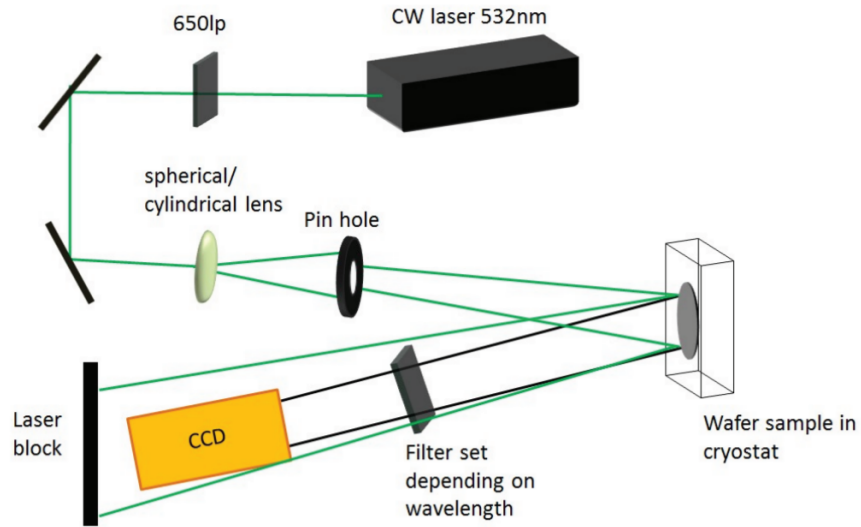
Figure 9.1: Wafer-imaging schematics

The schematic of the wafer imaging optical set-up is illustrated in Figure9.1. The wafer is mounted on a open-cycle cryostat that can be cooled to 77K using liquid nitrogen. A 532nm continuous wave (CW) laser with a maximum power of 5W is used to excite the wafer. A 650nm long pass filter is placed in front of the laser to block any long-wavelength components from the laser. After that, the laser beam is expanded using a cylindrical convex lens and projected onto the wafer. A pin hole (iris) is used to confine the laser beam expansion and to reduce the scattered light. Finally, photoluminescence emitted from the wafer is collected using a CCD facing the wafer. The photoluminescence is filtered by different short pass filters, depending on which PL component we are interested in. At 77K, GaAs photoluminescence is around 830nm, InAs wetting layer photoluminescence is around 870nm, and QD's photoluminescence is longer than 900nm.
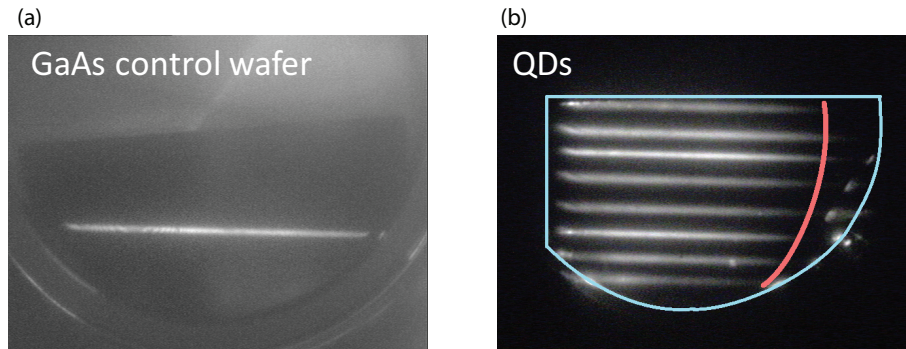
Figure 9.2: Photoluminescence collected using the wafer imaging setup, from (1) a GaAs control sample, (2) a sample with a QD gradient. The PL threshold of the QDs is indicated by the blue line.

It is important to maintain the laser intensity at a high value, so that the PL signal from QDs are strong enough to be detected by the camera. It is also important to create a uniform excitation source across the entire wafer, so that the intensity of the PL can directly infer the density of QDs. Therefore, the selection of the beam expanding lens is crucial. We use a cylindrical lens, because the line-shaped laser that it produces has higher intensity per area than the equivalent circular-shaped laser produced from a spherical lens. The 532nm laser beam has a Gaussian spatial intensity distribution,

and this distribution is maintained with any beam expanding optical elements. To gain almost uniform illumination of the sample, the lens is placed 30cm away from the wafer, and is aligned to direct light from the edge of the Gaussian intensity distribution.

Figure 9.2 shows the PL collected using the wafer imaging setup with a cylindrical lens. A GaAs wafer without QDs is used to calibrate the laser intensity in a horizontal line, as shown in Figure 9.2(a). An almost uniform PL line across the cleaved wafer is observed, indicating semi-uniform illumination. The PL from QDs in a wafer with a QD density gradient in the horizontal direction is shown in Figure 9.2(b). Multiple line scan across the wafer (blue frame) indicates a PL threshold towards the right side of the wafer, as indicated by the red line. This shows that the QDs density near the red line is 1 QD/μm^2.

9.2 Micro-photoluminescence

To study the photoluminescence of a single quantum dot, we use a micro-photoluminescence setup that contains both microscopy and spectrocopy functions. A schematic of our micro-photoluminescence setup is shown in Figure9.3. This diagram contains two micro-PL setups with two cryostats: one closed-cycle cryostat on the right and one magneto-optical cryostat on the left. We will first focus on the right side of the diagram with the closed-cycled cryostat.

9.2.1 Closed-cycle Cryostat

The sample can be cooled to 7K using the ARS closed-cycle cryostat. The entire cryostat is mounted on a translation stage with μm accuracy, so that the location of the sample is adjustable. A collimated LED light is used to illuminate the sample for microscopy analysis, and the image is collected using a CMOS camera. After locating and position the aperture at the center of the screen, the LED source can be turned off.

A tunable Ti-sapphire laser is used to excite the quantum dot for spectroscopy analysis. The laser can be tuned from 780nm to 870nm, and can operate in either
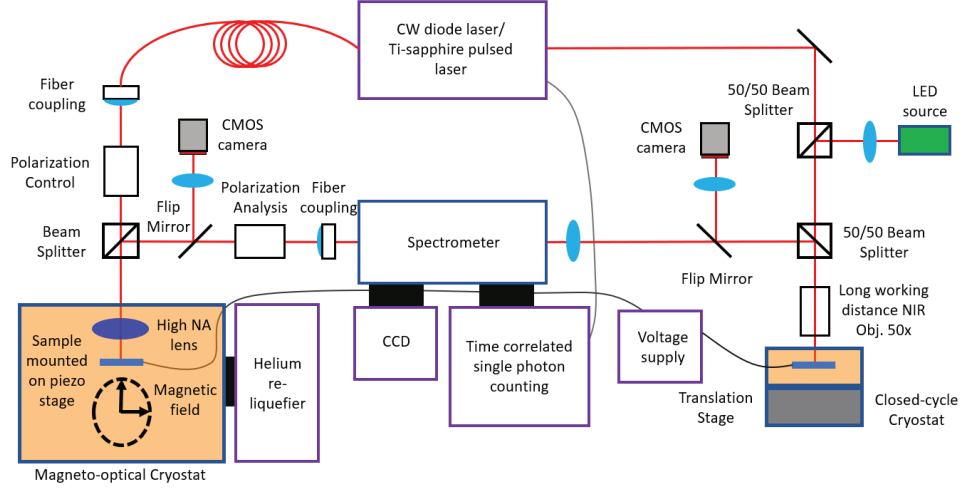
Figure 9.3: Micro-photoluminescence set-up schematic with a closed-cycle cryostat and magneto-optical cryostat

CW mode or pulsed mode. The 780nm laser can excite the GaAs substrate, the InAs wetting layer, and the quantum dot. But the single QD PL can be overshadowed by the GaAs PL. Using excitation around 870nm which is below the GaAs and the wetting layer bandgap can avoid this problem and only excite carriers in the QD. After passing through the two 50/50 beamsplitters, the laser is focused on the sample with a spot size approaching the diffraction limit using a NIR objective. Photoluminescence from the sample can be collected using the CMOS camera or the spectrometer. The output from the spectrometer can go either to a liquid nitrogen cooled CCD for spectral analysis or to a time-correlated photon counting module (TCSPC) for temporal analysis.

Many filters that are used in the micro-PL setup are not shown in the diagram. A 950nm short-pass filter is placed in front of the laser, in order to filter out the excitation light that might be mixed with the QDs signal. The laser intensity can also be reduced using neutral-density filters if the PL is too bright and exceeds the detection limit of the CCD. Because both the laser light and the PL will be reflected by the beamsplitter, filters are placed in front of the spectrometer to screen the laser. To analyze the GaAs PL, two OD5 800nm long-pass filters are placed in front of the spectrometer. GaAs PL is commonly used for alignment because it is much brighter

than the QDs PL. To analyze the QDs PL, two OD5 900nm long-pass filters are placed in front of the spectrometer. These filters can also be placed in front of the CMOS camera, if one wants to use the camera to locate a single aperture with QDs.

Additionally, power supplies are connected to the sample through the cryostat to apply voltages during the PL experiment. For multi-electrode devices, we use a Keithley 2230 multi-channel power supply to apply voltages to different electrodes independently. The Keithley 2230 model has 3 channels that can apply voltages from 0 to 30 V, with a compliance current up to 1.5 A. The resolution of the power supply is 1 mV and 1 mA, which is sufficient for our experiments.

9.2.2 Magneto-optical Cryostat

The magneto-optical cryostat setup on the left side of Figure 9.3 uses a similar operation mechanism. The laser is guided to the sample through a similar optical path, and the photoluminescence is collected using either a CMOS camera or a CCD with a spectrometer. There are several differences: 1) Up to 8T magnetic field in either the vertical or the lateral direction can be generated by the heavy superconducting coils located at the bottom of the cryostat. 2) The sample can be cooled to 4K because liquid helium is used to cool down both the superconducting magnet and the cryostat. A helium reliquefier is used to conserve the helium and prolong experimental run time. 3) A high numerical aperture lens is mounted in the cryostat, serving as the objective lens, instead of a long working distance objective. 4) Because the cryostat is too tall and heavy to be mounted on an optical table, excitation and luminescence photons are guided through fiber. This results in a 50% loss of the observed photoluminescence due to the fiber's coupling efficiency.

While the magneto-optical cryostat can apply magnetic field, and can operate at a lower temperature, the cost to maintain its operation is much higher compared to the closed-cycle cryostat. In our experiment, we will only use the closed-cycle cryostat for optical analysis without an applied magnetic field.

Chapter 10

DEVICE CHARACTERIZATION

After the 3-electrode device fabrication, we test the device performance both electrically and optically. In this chapter I will go through the results of the all-Schottky-contact 3-electrode device. I will also present COMSOL simulations that support the physical phenomenon we observe.

10.1 Electrical Characterization

10.1.1 Hall effect measurement

Before the fabrication, we measure the carrier concentration in the unintentionally doped GaAs region using Hall effect measurements. The results show a sheet carrier concentration around $1.46 \times 10^{12}/cm^2$, which corresponds to a bulk carrier concentration around $5 \times 10^{16}/cm^2$. The carrier dopant type is p-type, likely due to carbon contamination in the chamber during growth. These carbon defects also act as recombination centers that leads to non-radiative recombination pathways for excited carriers, leading to reduced PL.

10.1.2 I-V curve

To confirm the contact type of the three metal electrodes, we measure the I-V curve of the device at room temperature after fabrication. The measurement is conducted using a multi-channel voltage source Keithley 2230. When we apply $\pm 1V$ on the top electrode and ground the two lateral electrodes, the measured current is below the detection limit of our voltage source (0.02mA). Similar results are obtained under the lateral bias geometry. This indicates that all three electrodes have Schottky contacts with Schottky barriers preventing large current flow. We observe a significant

current increase around ± 3 to ± 5V, implying a device breakdown field around 100 to 150kV/cm.

10.2 Optical Charaterization

10.2.1 Micro-photoluminescence with Bias

We mount the device in an ARS-DMX20 cryostat for micro-photoluminescence study at 8K. We use an LED light to locate each aperture and a 5uW 780nm continuous-wave (CW) laser to excite the quantum dot. We generate the 780nm CW excitation using a MIRA-900 Ti:sapphire laser; both the power and the wavelength of the excitation are tunable. We focus the laser light down to the diffraction limit using a NIR objective so that only a single aperture is excited at one time. We measure the photo-luminescence with a liquid-nitrogen-cooled CCD, filtered by two ND5 900nm long-pass filters and spectrally-resolved by a NIR spectrometer with a resolution of 30μeV. We use a Keithley 2230 multi-channel voltage source to apply voltages to the device.

We first survey all the apertures to find the ones that contain a single QD, then apply voltages to those selected apertures. Figure 10.1 shows the photoluminescence intensity graph from 4 different apertures (QDs) as a function of applied voltages. We collect all PL spectroscopy data with a device current smaller than 50μA, close to our detection limit.

For the data presented in the left column in Figure 10.1, we ground the two lateral electrodes and apply a voltage V to the top electrode. We will name this bias configuration the vertical bias. Under these conditions we can see an asymmetric charging PL map centered at 0V in all 4 QDs presented here. For example, in QD (a), the positively charged state (X^+) with energy 1317.8meV occurs at -0.3V, indicated by the dashed line. The neutral exciton state (X) with energy 1314.3meV disappears at the same voltage. However, the same charged state does not occur when we apply a positive voltage to the top electrode, though the neutral exciton state disappears.

We identify the X, XX, and X+ states in the optical spectra from QD(a) (top row of Figure 10.1) through several complementary observations. First, we observe that the
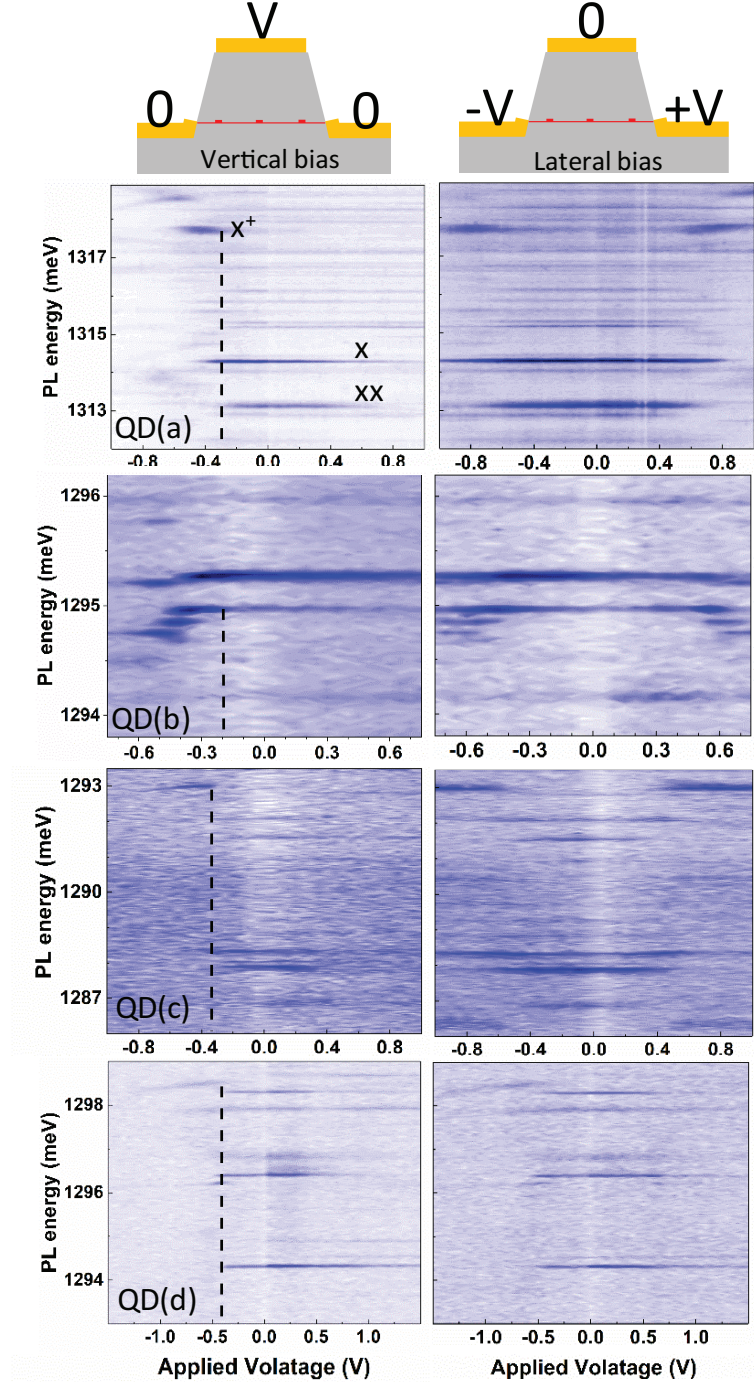
Figure 10.1: Micro-photoluminescence of four different QDs from 4 different apertures on the 3-electrode device. The bias configuration of each PL column is indicated at the top. The lateral axis represents the applied voltage V in each case and the vertical axis represents the PL energy from a single aperture.

two lines labelled as X and XX coexist over a wide range of applied voltages, which is tyipcal for the neutral and biexciton states.[39, 71] Second, excitation-power-dependent measurements show that the line identified as X dominates under low excitation fluence conditions. Third, the observed blue shift of the X+ PL line relative to the X PL line (by 3.5eV) is consistent with previous measurements of the energy shift associated with X+ states.[39]

We observe similar photoluminescence features in QD (b), (c), and (d). The energy differences between the neutral exciton state and the positively charged state vary between different dots. This is likely due to the different electron-hole interaction strength as a result of variations in QD size and composition.

For the data presented in the right column, we apply equal and opposite voltages to the two lateral electrodes while grounding the top electrode. We will name this voltage configuration the lateral bias. The magnitude of the voltage applied is the same as the vertical bias configuration. Under these conditions we observe the same charging sequence in each QD, just as the left column. The difference is the symmetry. For example: in QD (a), the positively charged exciton emerges symmetrically at V=0.6V and V=-0.6V. The same symmetric charging PL map can be seen in QD (b) and (c). This symmetric feature is characteristic of the majority of the apertures that we surveyed. Very occasionally, we could observe asymmetric charging features similar to those obtained under the vertical bias, as shown in QD (d). The faint charged line around 1288.5meV shows up only on one side of the PL bias map, in contrast to the symmetric charging pattern observed in apertures a, b, and c.

10.2.2 Power Dependence

The charging observed in Figure 10.1. could come from either electrical injections of a single charge carrier or from optical generations of an electron-hole pair followed by the escape of one of the carriers by tunneling. In the case of electrical injection, it is possible for the resident charge to escape the QD, but it is likely that an additional carrier will then tunnel into the QD because the Fermi level is at or below
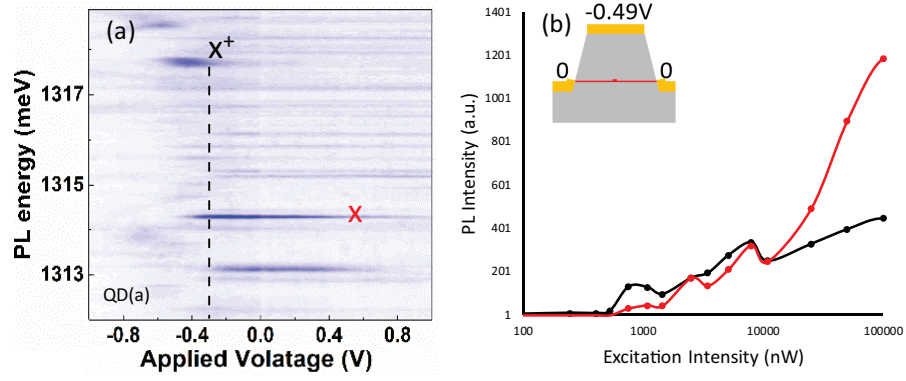
Figure 10.2: Power dependence study of the charged states. (a) the vertical bias PL map of QD (a). (b) The PL intensity of the neutral exciton state (red X) and positively charged states (black X^+) with different excitation intensity. The top voltage is fixed at -0.49V. (dashed line in (a))

the energy level of the QD. As a result, under electrical charging conditions the charged and neutral states typically co-exist over a relatively small range of applied voltages. When a QD is charged with a single carrier through optical charging, subsequent PL recombination events will take place in the presence of that excess charge, emitting PL associated with the charged exciton state, until the second (resident) charge escapes through tunneling or non-radiative relaxation. Once the resident charge has escaped, neutral exciton emission can be observed until one of the optically generated charges again escapes to leave a resident charge. As a result, neutral and charged exciton PL can both be observed over a relatively large range of applied bias voltages. Moreover, the ratio of neutral to charged exciton PL depends more sensitively on excitation power because two optical excitation events must occur faster than the loss rate of the resident charge in order for emission from an optical charged exciton state to be observed.

To distinguish electrical and optical charging in our devices we first note that the charged state turns on relatively sharply as a function of applied bias voltage, at approximately -0.3V for QD (a) as shown in Figure 10.1(a). The charged state coexists with the neutral exciton state for only a small range of applied voltage. Next, we measure the PL under a negative vertical bias with different excitation powers. We

choose the voltage where the charged state is bright and the neutral exciton almost disappears, as indicated by the dashed line in Figure 10.2(a). Figure 10.2(b) shows the PL intensity of the neutral state (red) and the charged state (black) as a function of the excitation laser intensity. The neutral exciton's intensity is close to zero when the excitation power is low, and it remains smaller than the charged exciton intensity when the excitation power is smaller than 10μW. When the excitation power is higher than 10μW, the neutral exciton's intensity increases drastically, which results in a much higher PL intensity than the charged state. Together these data show that charging comes from electrically-injected holes rather than optical charging. The fact that our sample and substrate are both lightly p-doped provides furher evidence that the charged state is generated by an electrically-injected hole.

10.2.3 Wavelength Dependence
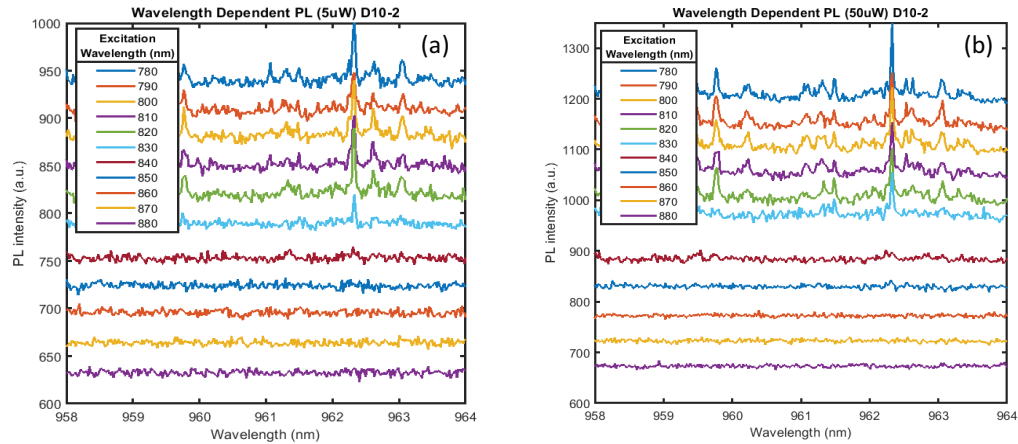
Figure 10.3: Wavelength dependent study of a single QD PL. The same wavelength threshold for QD PL is found in measurement with 5uW (a) and 50uW (b) excitation powers.

To further investigate this charging effect, we conduct wavelength-dependent micro-PL measurement on these QDs. The PL of QD(c) as a function of excitation wavelength is shown in Figure 10.3. The PL intensity begins to drop significantly when the excitation wavelength increases from 820nm to 830nm, and reaches zero

for excitation wavelengths longer than 830 nm. This indicates that carriers involved in PL emission are generated by excitation across the GaAs bandgap, with weaker generation through near-band-gap impurity states that typically emit at around 830 nm. This excitation wavelength threshold does not change with different excitation powers, as compared in Figure 10.3(a) and (b). This threshold also remains the same for different QDs, as shown in the appendix. The fact that we do not observe PL emission for excitation wavelengths longer than 830 nm indicates that the Fermi level of the device at 8K is close to the valence band-edge. Because the Schottky barriers height of the metal contacts are close to the mid-band of GaAs, there is a significant amount of band-bending near the metal contacts. Moreover, the close-to-band-edge Fermi level also reduces the depletion width of the substrate. As a result, the exact electric field applied to these QDs cannot be simply calculated by a linear function of the applied voltages.

10.3   COMSOL simulation

The mechanism of these charging effects can be qualitatively explained by the band-bendings as a function of bias by using COMSOL simulations with the semiconductor model. We build the device model with a geometry mimicking the device structures in the SEM picture. For non-polar semiconductors like GaAs, we use 0.8V as the Schottky barrier height for Ti/Au metal contact. We use a Fermi level that's close to what we deducted from the wavelength-dependent measurement for all simulations. The electric potential and the band diagram in the device are shown in Figure 10.4 and Figure 10.5.

10.3.1   Vertical Bias

The colored surface map in Figure 10.4 (a) shows the electric potential of the 3-electrode device with -1V applied to the top electrode and two grounded lateral electrodes. The bias forms a large potential gradient near the two lateral electrodes, while the rest of the mesa's potential remains relatively flat. A more direct view is
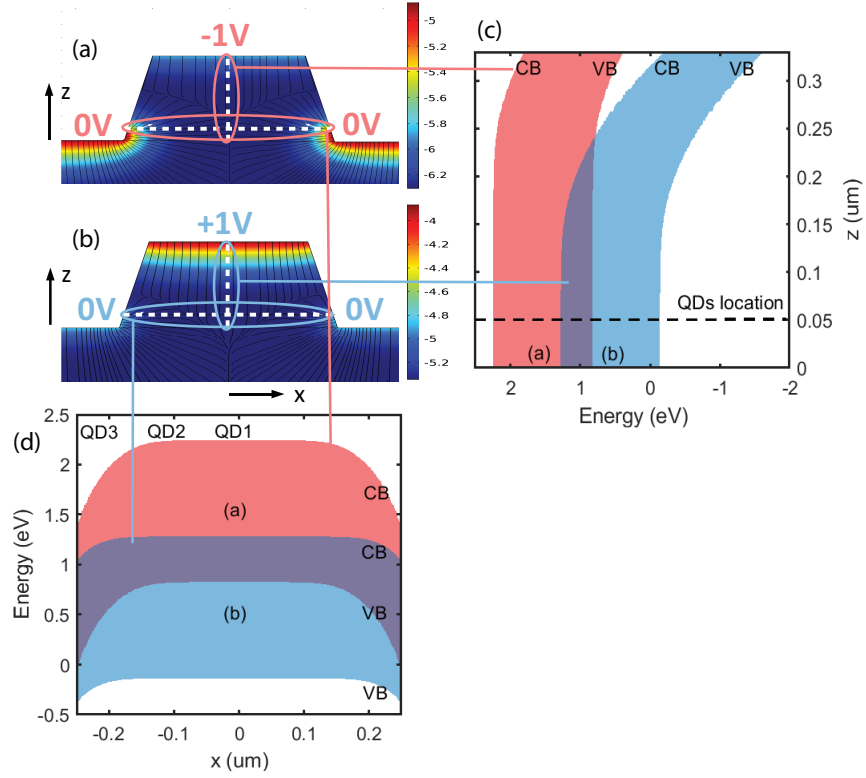
Figure 10.4: COMSOL simulation showing the device band-structure under (a) negative vertical bias and (b) positive vertical bias. The surface map shows the relative electric potential in the device. (c) and (d) shows the band structure along the vertical (c) and lateral (d) cut-lines in the mesa, corresponding to the bias applied.

presented in the band diagrams in (c) and (d). The vertical white line in Figure 10.4 (a) follows the center of the mesa, and the horizontal white line represents the location of the QDs. The red curves in Figure 10.4 (c) and (d) show the 1-D band structure along the vertical and horizontal cut-lines, respectively. We can see that in the lateral direction, there is little electric field at the center of the mesa. Most of the electric field is concentrated at the outer 100nm edge of the mesa. In the vertical direction, the band remains relatively flat at all regions.

In contrast, the electrical potential when we apply +1V on the top electrode and ground the two lateral electrodes is shown in Figure 10.4 (b). We again show the band structures along the two white lines in (c), (d), this time with the blue curves.

Under these voltage conditions, the lateral band-bending is much smaller compared to (a) and the band-bending in the vertical direction becomes larger. We expect that the band bending could extend to the spatial location of the QDs if higher voltages were applied.

10.3.2 Lateral Bias
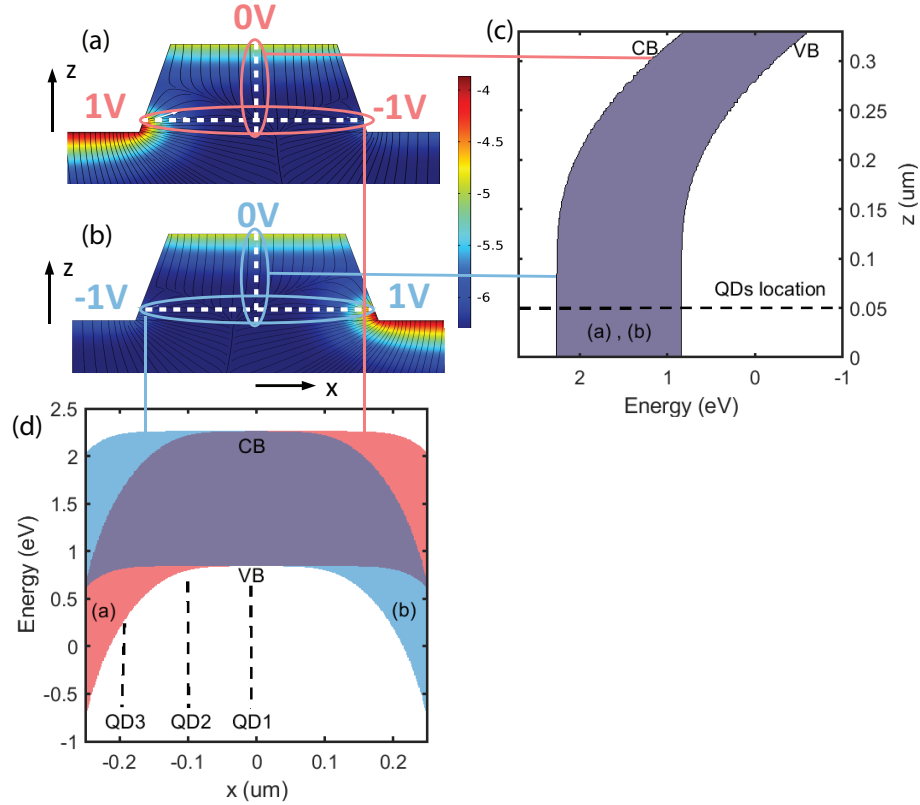
Figure 10.5: COMSOL simulation showing the device band-structure under (a) positive lateral bias and (b) negative lateral bias. The surface map shows the relative electric potential in the device. (c) and (d) shows the band structure along the vertical (c) and lateral (d) cut-lines in the mesa, corresponding to the bias applied.

The electric potential and band structures of the device under the lateral bias conditions is shown in Figure 10.5. The surface map in Figure 10.5(a) shows that when we apply 1V on the left electrode and -1V on the right electrode, a large potential

gradient is formed near the left electrode. This is obvious when we look at the band-structure at the QD-level horizontal cut-line shown in Figure 10.5(d) in red. If we flip the symmetry and apply positive voltage to the right electrodes, we observe that the band-structure in the lateral direction flips symmetrically as well, as indicated by the blue curve in (d). In both cases, there is a large band bending in the vertical direction, as shown by the band-structure in Figure 10.5(c).

10.3.3   Charging a QD using Lateral Electric Field

Considering the band-bending under these bias conditions and the location of the quantum dot, it's likely that the charging comes from the induced lateral electric field. At 8K, unintentionally p-doped carriers will freeze out, pushing the Fermi level close to the valence band edge. While these carriers are not able to escape to the GaAs valence band, they could form a carrier reservoir at the wetting layer. When the lateral electric field is high on either side, carrier to tunnelling into the QD from the wetting layer becomes possible. We stress that it is the changing lateral electric field profile that leads to the charging observed under BOTH lateral and vertical applied bias.

To understand the range of observed charging patterns, we now consider several illustrative potential locations for the QDs within the mesa. We will first analyze the case where the QDs are located near the center of the mesa, such as QD1 and QD2 drawn in Figure 10.4 and 10.5. Under a negative vertical bias, a large lateral electric field can be formed around the QD while the vertical electric field component is negligible. In this case holes can easily tunnel into the QD from either side of the mesa because of the induced lateral electric field. On the other hand, holes are not likely to be injected into the QD when the top electrode has a positive bias, because the lateral electric field component is small. The reduction in PL intensity, in this case, is likely due to the vertical electric field. Because the QDs are located near the center of the mesa, reversing the symmetry of the bias from the two lateral electrodes will result in charging from the opposite side, i.e. a symmetrical charging pattern centered around 0V. This is likely the case for QD (a), (b) and (c) in Figure 10.1.

In contrast, when the QD is located on the edge of the mesa, such as QD3 in Figure 10.4 and Figure 10.5, the charging under vertical bias will be similar to QD1 and QD2. However, because the band-bending is large when +1V is applied to the proximate electrode, but very small when -1V is applied, charging through lateral electric field is only expected for one of the two 'ends' of the lateral electric field range. As a result, the PL bias map should be asymmetrical. This is likely the case for QD (d) in Figure 10.1. We note that QDs from the edge of the mesa have a much smaller optical cross-section with the laser excitation, so the PL intensity is much lower. This is reflected in the PL intensity map and would prevent us from observing many QDs located near the extreme edges of the mesa.

10.4 Conclusion

In conclusion, the 3-electrode device we fabricated without any insulators shows interesting photoluminescence effects that indicate charging through a lateral electric field. We measure the photoluminescence under both vertical and lateral bias conditions, and observe changes in the symmetry of the PL bias map. We conduct power dependence PL experiments that reveal that the charging comes from electrically-injected holes. We then use the wavelength-dependent excitation experiment to probe the rough location of the Fermi level and calculate the band structure under different biases using COMSOL simulations. The simulations support our hypothesis of lateral electric field charging, due to the large band-bending near the Schottky contact.

It is likely that there is a 2-D electric field formed near the QD location under our bias conditions. However, quantitatively characterizing the magnitude and direction of this field is still challenging. Part of the uncertainty lies in the exact location of the Fermi level because the competition of photo-generated carriers and frozen carriers are hard to simulate at a low temperature. Moreover, the lack of Stark shifts in the PL bias map indicates that the magnitude of the electric field is small. To understand this result in more detail, a more systematic study of how III-V devices behave at extremely low temperature is needed.

Chapter 11

SUMMARY AND FUTURE WORKS

Hole spin states in QDs and QDMs have unique optical properties that can be used in a wide range of quantum information applications. In this work, we explored the properties of a single hole spin states under a 2-D electric field. Our main results can be summarized into two categories:

1. To precisely calculate the energy level of a single hole state, we developed a hybrid calculation architect that combined the atomistic tight-binding simulation with a finite matrix approximation. We also developed a data visualization algorithm using MATLAB that illustrated the spin texture of a single hole state. Using these computational methods, we discovered that lateral electric fields can polarize the hole spin in a single QD under a Voigt geometry magnetic field. Moreover, we can use 2-D electric fields to induce and control the hole spin mixing effect in a InAs/GaAs QDM.

2. To design the device that can apply 2-D electric fields to a InAs QD or QDM, we used COMSOL device simulation with the semiconductor module. We proposed a 3-electrode device design and a 4-electrode device design. We fabricated the 3-electrode device with an InAs QD sample in a semi-intrinsic GaAs matrix. We observed a shift in the symmetry of the charging PL diagram when we changed the vertical bias to the lateral bias. We explained the phenomenon by lateral field induced charging from the wetting layer, as supported by the COMSOL device simulation.

Our simulation results suggest the possibility of building qubit states with hole spin states controlled by a 2-D electric field. Our experimental results demonstrate charging a single QD using lateral electric field, and show our closest effort to engineer a device that can apply a 2-D electric field. Future research around this topic can include:

1. The spin texture concept presented in the simulation results can be explored in more detail in the future. For example, we could choose to analyze the cross-section plane of the QD and QDM, under a variety of electric field and magnetic field conditions. A more comprehensive study on the spin texture could reveal crucial information on hole spin decoherence, and prompt new device designs for future qubit applications.

2. The spin polarization effect also has not been observed experimentally yet. This effect can be resolved theoretically from the polarization of a neutral exciton in a QD, because only holes will polarize under parallel in-plane electric and magnetic fields. Specifically, as we rotate the in-plane magnetic field while keeping the in-plane electric field constant, we should see the ground polarization of a single QD rotates accordingly.

3. We need better simulations to guide the next generation device design. For example, including optical excitation effects under low-temperature conditions in these device simulations can improve the accuracy of our simulations. Based on these simulations, we could deduce the location of the QD in the mesa from its PL spectroscopy under different biases. Another example is combining the semiconductor device module with the FDTD module, and integrate the 3-electrode device or 4-electrode device with photonic structures such as a waveguide or a photonic crystal cavity.

4. To achieve 2-D electric field control, we need to grow better QD samples with a lower GaAs background doping level. We could also further reduce the size of the device to 200nm and use 4 to 6 electrodes to apply 3-D electric field on demand. The device can also be integrated in a photonic waveguide/cavity structure, for applications such as tunable single photon sources on chip and tunable spin qubits.

Bibliography

[1]   R. Van Meter and C. Horsman. "A blueprint for building a quantum computer". In: *Communications of the ACM* 56.10 (2013), pp. 84–93.

[2]   M. A. Nielsen and I. Chuang. "Quantum computation and quantum information". In: (2002).

[3]   D. Aharonov and M. Ben-Or. "Fault-tolerant quantum computation with constant error rate". In: *SIAM Journal on Computing* 38.4 (2008), pp. 1207–1282.

[4]   P. W. Shor. "Scheme for reducing decoherence in quantum computer memory". In: *Physical review A* 52.4 (1995), R2493.

[5]   A. R. Calderbank et al. "Quantum error correction via codes over GF (4)". In: *IEEE Transactions on Information Theory* 44.4 (1998), pp. 1369–1387.

[6]   R. Lafiamme et al. *Perfect quantum error correction code.* 1996.

[7]   A. G. Fowler et al. "Surface codes: Towards practical large-scale quantum computation". In: *Physical Review A* 86.3 (2012), p. 032324.

[8]   A. G. Fowler, A. M. Stephens, and P. Groszkowski. "High-threshold universal quantum computation on the surface code". In: *Physical Review A* 80.5 (2009), p. 052312.

[9]   M. Reagor et al. "Demonstration of universal parametric entangling gates on a multi-qubit lattice". In: *Science advances* 4.2 (2018), eaao3603.

[10] E. A. Martinez et al. "Real-time dynamics of lattice gauge theories with a few-qubit quantum computer". In: *Nature* 534.7608 (2016), pp. 516–519.

[11] D. M. Zajac et al. "Resonantly driven CNOT gate for electron spins". In: *Science* 359.6374 (2018), pp. 439–442.

[12] R. Barends et al. "Superconducting quantum circuits at the surface code threshold for fault tolerance". In: *Nature* 508.7497 (2014), p. 500.

[13] *IBM Q system announces 20qubit system ready to use, 50qubit system in development.* URL: https://www-03.ibm.com/press/us/en/pressrelease/53374.wss.

[14] N. M. Linke et al. "Experimental comparison of two quantum computing architectures". In: *Proceedings of the National Academy of Sciences* (2017), p. 201618020.

[15] V. Schäfer et al. "Fast quantum logic gates with trapped-ion qubits". In: *Nature* 555.7694 (2018), p. 75.

[16] J. Zhang et al. "Observation of a many-body dynamical phase transition with a 53-qubit quantum simulator". In: *Nature* 551.7682 (2017), p. 601.

[17] J. Yoneda et al. "A quantum-dot spin qubit with coherence limited by charge noise and fidelity higher than 99.9%". In: *Nature nanotechnology* 13.2 (2018), p. 102.

[18] K. Eng et al. "Isotopically enhanced triple-quantum-dot qubit". In: *Science Advances* 1.4 (2015), e1500214.

[19] A. Politi, J. C. Matthews, and J. L. O'brien. "Shor's quantum factoring algorithm on a photonic chip". In: *Science* 325.5945 (2009), pp. 1221–1221.

[20] J. L. O'Brien et al. "Demonstration of an all-optical quantum controlled-NOT gate". In: *Nature* 426.6964 (2003), p. 264.

[21] J. Schaibley et al. "Direct detection of time-resolved Rabi oscillations in a single quantum dot via resonance fluorescence". In: *Physical Review B* 87.11 (2013), p. 115311.

[22] B. Höfer et al. "Independent tuning of excitonic emission energy and decay time in single semiconductor quantum dots". In: *Applied Physics Letters* 110.15 (2017), p. 151102.

[23] D. Press et al. "Ultrafast optical spin echo in a single quantum dot". In: *Nature Photonics* 4.6 (2010), p. 367.

[24] B. Lekitsch et al. "Blueprint for a microwave trapped ion quantum computer". In: *Science Advances* 3.2 (2017), e1601540.

[25] D. Press et al. "Complete quantum control of a single quantum dot spin using ultrafast optical pulses". In: *Nature* 456.7219 (2008), p. 218.

[26] A. Kandala et al. "Hardware-efficient variational quantum eigensolver for small molecules and quantum magnets". In: *Nature* 549.7671 (2017), p. 242.

[27] D. Kim et al. "Ultrafast optical control of entanglement between two quantum-dot spins". In: *Nature Physics* 7.3 (2011), p. 223.

[28] M. Veldhorst et al. "Silicon CMOS architecture for a spin-based quantum computer". In: *Nature communications* 8.1 (2017), p. 1766.

[29] S. G. Carter et al. "Quantum control of a spin qubit coupled to a photonic crystal cavity". In: *Nature Photonics* 7.4 (2013), pp. 329–334.

[30] C. Schneider et al. "Microcavity enhanced single photon emission from an electrically driven site-controlled quantum dot". In: *Applied Physics Letters* 100.9 (2012), p. 091108.

[31] A. Greilich et al. "Optical control of one and two hole spins in interacting quantum dots". In: *Nature Photonics* 5.11 (2011), pp. 702–708.

[32] T. M. Godden et al. "Coherent optical control of the spin of a single hole in an InAs/GaAs quantum dot". In: *Physical review letters* 108.1 (2012), p. 017402.

[33] B. D. Gerardot et al. "Optical pumping of a single hole spin in a quantum dot". In: *Nature* 451.7177 (2008), p. 441.

[34] J. H. Prechtel et al. "Decoupling a hole spin qubit from the nuclear spins". In: *Nature materials* 15.9 (2016), p. 981.

[35] M. Doty et al. "Opportunities for single hole-spin control using delocalized states of quantum dot molecules". In: *Journal of Physics: Conference Series*. Vol. 245. 1. IOP Publishing. 2010, p. 012002.

[36] G. W. Bryant, N. Malkova, and J. Sims. "Mechanism for controlling exciton fine structure in quantum dots using electric fields: Manipulation of exciton orientation and exchange splitting at the atomic scale". In: *Physical Review B* 88 (2013), p. 161301.

[37] J. Lee et al. "Electrically driven and electrically tunable quantum light sources". In: *Applied Physics Letters* 110.7 (2017), p. 071102.

[38] D. Ellis et al. "Independent indistinguishable quantum light sources on a reconfigurable photonic integrated circuit". In: *Applied Physics Letters* 112.21 (2018), p. 211104.

[39] M. Doty et al. "Optical spectra of doubly charged quantum dot molecules in electric and magnetic fields". In: *Physical Review B* 78.11 (2008), p. 115316.

[40] E. Kawakami et al. "Electrical control of a long-lived spin qubit in a Si/SiGe quantum dot". In: *Nature nanotechnology* 9.9 (2014), p. 666.

[41] S. J. Angus et al. "Gate-defined quantum dots in intrinsic silicon". In: *Nano letters* 7.7 (2007), pp. 2051–2055.

[42] B. Mahler et al. "Towards non-blinking colloidal quantum dots". In: *Nature materials* 7.8 (2008), p. 659.

[43] E. Y. Chen et al. "CdSe (Te)/CdS/CdSe Rods Versus CdTe/CdS/CdSe Spheres: Morphology-Dependent Carrier Dynamics for Photon Upconversion". In: *IEEE Journal of Photovoltaics* 8.3 (2018), pp. 746–751.

[44] M. Möbius et al. "Photoluminescence quenching of InP/ZnS quantum dots by charge injection". In: *Quantum Sensing and Nanophotonic Devices XII*. Vol. 9370. International Society for Optics and Photonics. 2015, p. 93701X.

[45] X. Lin et al. "Electrically-driven single-photon sources based on colloidal quantum dots with near-optimal antibunching at room temperature". In: *Nature communications* 8.1 (2017), p. 1132.

[46] K. Yamaguchi, K. Yujobo, and T. Kaizu. "Stranski-Krastanov growth of InAs quantum dots with narrow size distribution". In: *Japanese journal of applied physics* 39.12A (2000), p. L1245.

[47] W. Heller, U. Bockelmann, and G. Abstreiter. "Electric-field effects on excitons in quantum dots". In: *Physical Review B* 57.11 (1998), p. 6270.

[48] D. Kim et al. "Optical spin initialization and nondestructive measurement in a quantum dot molecule". In: *Physical review letters* 101.23 (2008), p. 236804.

[49] X. Li et al. "An all-optical quantum gate in a semiconductor quantum dot". In: *Science* 301.5634 (2003), pp. 809–811.

[50] M. Doty et al. "Electrically tunable g factors in quantum dot molecular spin states". In: *Physical Review Letters* 97.19 (2006), p. 197202.

[51] M. F. Doty et al. "Hole-spin mixing in InAs quantum dot molecules". In: *Physical Review B* 81.3 (2010), p. 035308.

[52] O. Shchekin and D. Deppe. "1.3 μm InAs quantum dot laser with T o= 161 K from 0 to 80 C". In: *Applied Physics Letters* 80.18 (2002), pp. 3277–3279.

[53] J. Lott et al. "InAs-InGaAs quantum dot VCSELs on GaAs substrates emitting at 1.3 μm". In: *Electronics Letters* 36.16 (2000), pp. 1384–1385.

[54] Y. Okada et al. "Increase in photocurrent by optical transitions via intermediate quantum states in direct-doped InAs/GaNAs strain-compensated quantum dot solar cell". In: *Journal of Applied Physics* 109.2 (2011), p. 024301.

[55] S. Chen et al. "InAs/GaAs quantum-dot superluminescent light-emitting diode monolithically grown on a Si substrate". In: *ACS Photonics* 1.7 (2014), pp. 638–642.

[56] G. Yusa and H. Sakaki. "Trapping of photogenerated carriers by InAs quantum dots and persistent photoconductivity in novel GaAs/n-AlGaAs field-effect transistor structures". In: *Applied physics letters* 70.3 (1997), pp. 345–347.

[57] S. Krishna. "Quantum dots-in-a-well infrared photodetectors". In: *Journal of Physics D: Applied Physics* 38.13 (2005), p. 2142.

[58] P. Michler et al. "A quantum dot single-photon turnstile device". In: *science* 290.5500 (2000), pp. 2282–2285.

[59] H. Eisele et al. "Change of InAs/GaAs quantum dot shape and composition during capping". In: *Journal of Applied Physics* 104.12 (2008), p. 124301.

[60] N. Ledentsov et al. "Direct formation of vertically coupled quantum dots in Stranski-Krastanow growth". In: *Physical Review B* 54.12 (1996), p. 8743.

[61] H. Sasakura et al. "Effect of indium-flush method on the control of photoluminescence energy of highly uniform self-assembled InAs quantum dots by slow molecular beam epitaxy growth". In: *Journal of applied physics* 102.1 (2007), p. 013515.

[62] J.-Y. Marzin et al. "Photoluminescence of single InAs quantum dots obtained by self-organized growth on GaAs". In: *Physical review letters* 73.5 (1994), p. 716.

[63] Y.-J. Wei et al. "Deterministic and robust generation of single photons from a single quantum dot with 99.5% indistinguishability using adiabatic rapid passage". In: *Nano letters* 14.11 (2014), pp. 6515–6519.

[64] D. Gammon et al. "Fine structure splitting in the optical spectra of single GaAs quantum dots". In: *Physical review letters* 76.16 (1996), p. 3005.

[65] M. Bayer et al. "Fine structure of neutral and charged excitons in self-assembled In (Ga) As/(Al) GaAs quantum dots". In: *Physical Review B* 65.19 (2002), p. 195315.

[66] A. J. Brash et al. "High-fidelity initialization of long-lived quantum dot hole spin qubits by reduced fine-structure splitting". In: *Physical Review B* 92.12 (2015), p. 121301.

[67] J. Mar et al. "Electrical control of quantum-dot fine-structure splitting for high-fidelity hole spin initialization". In: *Physical Review B* 93.4 (2016), p. 045316.

[68] N. Somaschi et al. "Near-optimal single-photon sources in the solid state". In: *Nature Photonics* 10.5 (2016), p. 340.

[69] L. Hanschke et al. "Quantum dot single photon sources with ultra-low multi-photon probability". In: *arXiv preprint arXiv:1801.01672* (2018).

[70] N. Akopian et al. "Entangled photon pairs from semiconductor quantum dots". In: *Physical Review Letters* 96.13 (2006), p. 130501.

[71] R. J. Warburton. "Single spins in self-assembled quantum dots". In: *Nature materials* 12.6 (2013), p. 483.

[72] M. Doty et al. "Antibonding ground states in InAs quantum-dot molecules". In: *Physical Review Letters* 102.4 (2009), pp. 047401–1.

[73] B. Gerardot et al. "Manipulating exciton fine structure in quantum dots with a lateral electric field". In: *Applied Physics Letters* 90.4 (2007), p. 041101.

[74] M. Reimer et al. "Prepositioned single quantum dot in a lateral electric field". In: *Physical Review B* 78.19 (2008), p. 195301.

[75] K. Kowalik et al. "Influence of an in-plane electric field on exciton fine structure in InAs-GaAs self-assembled quantum dots". In: *Applied Physics Letters* 86.4 (2005), p. 041907.

[76] P. Fry et al. "Inverted electron-hole alignment in InAs-GaAs self-assembled quantum dots". In: *Physical review letters* 84.4 (2000), p. 733.

[77] G. Moody et al. "Electronic enhancement of the exciton coherence time in charged quantum dots". In: *Physical review letters* 116.3 (2016), p. 037402.

[78] X. Ma, G. W. Bryant, and M. F. Doty. "Hole spins in an InAs/GaAs quantum dot molecule subject to lateral electric fields". In: *Physical Review B* 93.24 (2016), p. 245402.

[79] H. Bluhm et al. "Dephasing time of GaAs electron-spin qubits coupled to a nuclear bath exceeding 200 μs". In: *Nature Physics* 7.2 (2011), p. 109.

[80] S. E. Economou et al. "Scalable qubit architecture based on holes in quantum dot molecules". In: *Physical Review B* 86.8 (2012), p. 085319.

[81] K. Hennessy et al. "Quantum nature of a strongly coupled single quantum dot–cavity system". In: *Nature* 445.7130 (2007), p. 896.

[82] X. Ding et al. "On-demand single photons with high extraction efficiency and near-unity indistinguishability from a resonantly driven quantum dot in a micropillar". In: *Physical review letters* 116.2 (2016), p. 020401.

[83] E. Peter et al. "Exciton-photon strong-coupling regime for a single quantum dot embedded in a microcavity". In: *Physical review letters* 95.6 (2005), p. 067401.

[84] M. Davanco et al. "Heterogeneous integration for on-chip quantum photonic circuits with single quantum dot devices". In: *Nature communications* 8.1 (2017), p. 889.

[85] C. Dory et al. "Complete coherent control of a quantum dot strongly coupled to a nanocavity". In: *Scientific reports* 6 (2016), p. 25172.

[86] P. M. Vora et al. "Spin–cavity interactions between a quantum dot molecule and a photonic crystal cavity". In: *Nature communications* 6 (2015), p. 7665.

[87] T. Yoshie et al. "Vacuum Rabi splitting with a single quantum dot in a photonic crystal nanocavity". In: *Nature* 432.7014 (2004), p. 200.

[88] J.-H. Kim et al. "Two-photon interference from the far-field emission of chip-integrated cavity-coupled emitters". In: *Nano letters* 16.11 (2016), pp. 7061–7066.

[89] Y.-M. He et al. "Deterministic implementation of a bright, on-demand single-photon source with near-unity indistinguishability via quantum dot imaging". In: *Optica* 4.7 (2017), pp. 802–808.

[90] S. Kiravittaya, H. Heidemeyer, and O. Schmidt. "Growth of three-dimensional quantum dot crystals on patterned GaAs (001) substrates". In: *Physica E: Low-dimensional Systems and Nanostructures* 23.3 (2004), pp. 253–259.

[91] C. Schneider et al. "Single site-controlled In (Ga) As/GaAs quantum dots: growth, properties and device integration". In: *Nanotechnology* 20.43 (2009), p. 434012.

[92] K. Jons et al. "Triggered indistinguishable single photons with narrow line widths from site-controlled quantum dots". In: *Nano letters* 13.1 (2012), pp. 126–130.

[93] M. K. Yakes et al. "Leveraging crystal anisotropy for deterministic growth of InAs quantum dots with narrow optical linewidths". In: *Nano letters* 13.10 (2013), pp. 4870–4875.

[94] J. P. Reithmaier et al. "Strong coupling in a single quantum dot–semiconductor microcavity system". In: *Nature* 432.7014 (2004), p. 197.

[95] C. Matthiesen et al. "Full counting statistics of quantum dot resonance fluorescence". In: *Scientific reports* 4 (2014), p. 4911.

[96] M. Zeeshan et al. "Quadrupole electric field for erasing the fine structure splitting in a single quantum dot". In: *arXiv preprint arXiv:1809.02538* (2018).

[97] P. Vogl, H. D. Hjalmarson, and J. D. Dow. "Semi-empirical tight-binding theory of the electronic structure of semiconductors". In: *Journal of the Physics and Chemistry of Solids* 44 (1983), pp. 365–377.

[98] G. W. Bryant et al. "Effect of mechanical strain on the optical properties of quantum dots: Controlling exciton shape, orientation and phase with a mechanical strain". In: *Physical Review Letters* 105 (2010), p. 067404.

[99] G. W. Bryant et al. "Controlling the optics of quantum dots with nanomechanical strain". In: *Physical Review B* 84 (2011), p. 235412.

[100] C. Pryor et al. "Comparison of two methods for describing the strain profiles in quantum dots". In: *Journal of Applied Physics* 83 (1998), pp. 2548–2554.

[101] T. B. Boykin et al. "Multiband tight-binding model for strained and bilayer graphene from DFT calculations". In: *Computational Electronics (IWCE), 2012 15th International Workshop on.* IEEE. 2012, pp. 1–4.

[102] M. Graf and P. Vogl. "Electromagnetic fields and dielectric response in empirical tight-binding theory". In: *Physical Review B* 51 (1995), pp. 4940–4948.

[103] D. J. Chadi. "Spin-orbit splitting in crystalline and compositionally disordered semiconductors". In: *Physical Review B* 16 (1977), pp. 790–795.

[104] K. C. Hass. "Electronic structure of $Hgt_{1-x}Cd_xTe$". In: *Physical Review B* 27 (1983), pp. 1088–1100.

[105] W. Jaskólski et al. "Strain effects on the electronic structure of strongly coupled self-assembled InAs/GaAs quantum dots: Tight-binding approach". In: *Physical Review B* 74 (2006), p. 195339.

[106] T. Saito and Y. Arakawa. "Electronic structure of piezoelectric $In_{0.2}Ga_{0.8}N$ quantum dots in GaN calculated using a tight-binding method". In: *Physica E (Amsterdam)* 15 (2002), pp. 169–181.

[107] S. Arseneau. *3D arrow plot from Mathworks.* URL: https://www.mathworks.com/matlabcentral/fileexchange/12274-3d-arrow-with-many-color-parameter-options.

[108] M. F. Doty et al. "Molecular engineering with artificial atoms: designing a material platform for scalable quantum spintronics and photonics". In: *Spintronics X.* Vol. 10357. International Society for Optics and Photonics. 2017, p. 1035739.

[109] J. Planelles, F. Rajadell, and J. I. Climente. "Symmetry-induced hole-spin mixing in quantum dot molecules". In: *Physical Review B* 92.4 (2015), p. 041302.

[110] W. Liu et al. "In situ tunable g factor for a single electron confined inside an InAs quantum dot". In: *Physical Review B* 84.12 (2011), p. 121304.

[111] W. Sheng. "Electrical tuning of exciton g factors in quantum dot molecules: Effect of hole localization". In: *Applied Physics Letters* 95 (2009), pp. 113103–113105.

[112] W. Sheng. "g-factor tuning in self-assembled quantum dots". In: *Applied Physics Letters* 96 (2010), pp. 133102–133103.

[113] J. van Bree et al. "Spin-Orbit-Induced Circulating Currents in a Semiconductor Nanostructure". In: *Physical Review Letters* 112.18 (2014), p. 187201.

[114] J. van Bree et al. "Geometric and compositional influences on spin-orbit induced circulating currents in nanostructures". In: *Physical Review B* 90.16 (2014), p. 165306.

[115] E. Zallo et al. "Strain-induced active tuning of the coherent tunneling in quantum dot molecules". In: *Physical Review B* 89.24 (2014), p. 241303.

[116] T. Andlauer and P. Vogl. "Electrically controllable g tensors in quantum dot molecules". In: *Physical Review B* 79.4 (2009), p. 045307.

[117] F. Rajadell, J. Climente, and J. Planelles. "Large hole spin anticrossings in InAs/GaAs double quantum dots". In: *Applied Physics Letters* 103.13 (2013), p. 132105.

[118] K. Gawarecki, P. Machnikowski, and T. Kuhn. "Electron states in a double quantum dot with broken axial symmetry". In: *Physical Review B* 90.8 (2014), p. 085437.

[119] R. E. March. "An introduction to quadrupole ion trap mass spectrometry". In: *Journal of mass spectrometry* 32.4 (1997), pp. 351–369.

[120] X. Zhou and M. Doty. "Design of 4-electrode optical device for application of vector electric fields to self-assembled quantum dot complexes". In: *Journal of Applied Physics* 116.16 (2014), p. 163101.

[121] H. Kim and I.-K. Oh. "Review of plasma-enhanced atomic layer deposition: Technical enabler of nanoscale device fabrication". In: *Japanese Journal of Applied Physics* 53.3S2 (2014), 03DA01.

[122] *Technics on Ion Mill Etch Rates.* URL: http://apps.mnc.umn.edu/pub/pdf/equipment/ionmill_rates.pdf.

[123] A. V. Kuhlmann et al. "A dark-field microscope for background-free detection of resonance fluorescence from single semiconductor quantum dots operating in a set-and-forget mode". In: *Review of scientific instruments* 84.7 (2013), p. 073905.

APPENDIX MATERIALS

A.1   A Simple S-band Model

An example of how tight-binding simulation works can be shown with a simple s-band model that includes a 1-D crystal of N atoms. For each atom's wavefunction, we will only consider the ground orbital state, i.e. s-band. The Bloch states of the system's Hamiltonian H can be constructed as a linear combination of atomic wavefunctions $|n\rangle$:

$$|k\rangle = \frac{1}{\sqrt{N}} \sum_{n=1}^{N} e^{ikna} |n\rangle \tag{A.1}$$

where a is the lattice constant of the crystal and k is the wave-vector in the first Brillion zone. The factor $\frac{1}{\sqrt{N}}$ is used to normalized the wavefunction. Considering only nearest neighbour interactions, the overlap of wavefunctions can be written as:

$$\langle n|n\rangle = 1 \; ; \langle n \pm 1|n\rangle = S; \tag{A.2}$$

Where S is the overlap between wavefunctions of adjacent atoms. The non-zero Hamiltonian terms are:

$$\langle n|H|n\rangle = E_0; \langle n \pm 1|H|n\rangle = E_{ij} \tag{A.3}$$

Here E_0 is the energy of atomic orbital s in an isolated atom. E_{ij} is the bond energy between atoms. This term is not calculated, but given or adjusted to match experiment.

Using these expressions we can derive the energy of the state $|k\rangle$:

$$\langle k|H|k\rangle = \frac{1}{N}\sum_{n,\,m}e^{ik(n-m)a}\langle m|H|n\rangle$$

$$= \frac{1}{N}\sum_n\langle n|H|n\rangle + \frac{1}{N}\sum_n\langle n-1|H|n\rangle e^{+ika} + \frac{1}{N}\sum_n\langle n+1|H|n\rangle e^{-ika} \quad \text{(A.4)}$$

$$= E_0 + 2E_{ij}\cos(ka)$$

$$\langle k|k\rangle = \frac{1}{N}\sum_n\langle n+1|n\rangle e^{-ika} + \frac{1}{N}\sum_n\langle n-1|n\rangle e^{+ika} + \frac{1}{N}\sum_n\langle n|n\rangle e^{+ika} = 1 + 2S\cos ka$$

$$\text{(A.5)}$$

$$E(k) = \frac{\langle k|H|k\rangle}{\langle k|k\rangle} = \frac{E_0 + 2E_{ij}\cos ka}{1 + 2S\cos ka} \quad \text{(A.6)}$$

A.2   QDM movie

1. symmetric QDM with piezo electric field

   - $2nd state(flip state at anti-crossing)$
     https://www.youtube.com/watch?v=k1xumckg3g0
   - $trace same state$
     https://www.youtube.com/watch?v=lZFljOwuf0o

2. symmetric QDM with lateral electric field

   - Fy=10kV/cm
     https://www.youtube.com/watch?v=nFIu7y1f4HQ
   - Fx with gradient
     https://www.youtube.com/watch?v=-4P-wsnSkGA

3. asymmetric QDM

   - QDM with vertical field only
     https://www.youtube.com/watch?v=m3zaWxGMUHU
   - QDM with Fx field (parallel to geometric offset) https://www.youtube.com/watch?v=0rcmLPcX_Gs
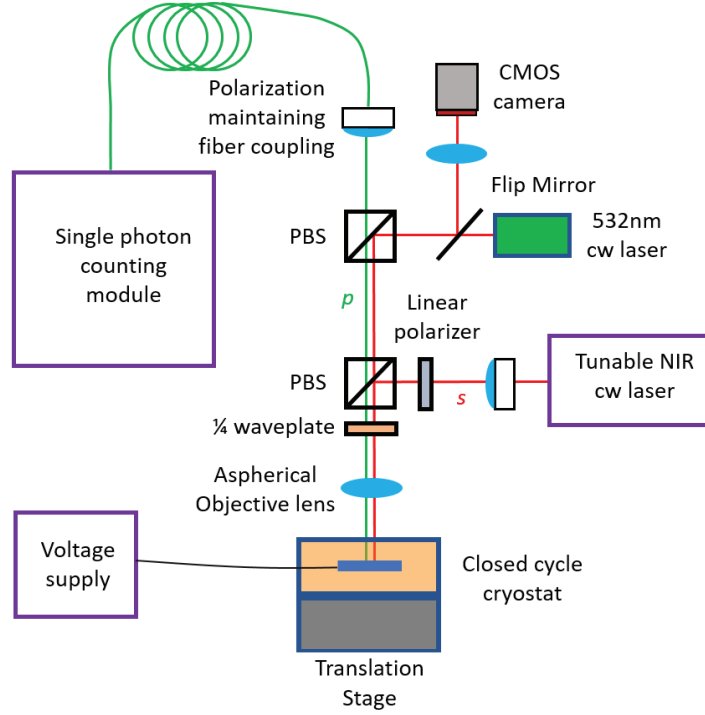
Figure A.1: A schematic of the resonance fluorescence setup

A.3 Resonance Fluorescence Setup

One of the techniques that can significantly enhance our spectroscopy resolution beyond the spectrometer's limit is resonance fluorescence (RF). The resonance fluorescence experiment uses a narrow line width wavelength-tunable laser to scan a single QD's emission. When the excitation wavelength is on resonance with the QD's emission wavelength, strong fluorescence will be emitted from the QD. Typical resonance fluorescence experiments use linear polarized light to excite the sample and detect the fluorescence in the crossed polarization while filtering out the reflected laser light. The resolution limit of this technique is the line-width of the laser and wavelength tunability. This could be in the range of hundreds of neV, which is two orders of magnitude smaller than the resolution of our spectrometer (30μeV at best).

Based on the setup illustrated by Kuhlmann et al. [123], we build a similar

resonance fluorescence setup as shown in Figure A.1. The tunable NIR CW laser has a highly linear polarization, and we name it "s". We will name the cross-linear polarized light "p". The fiber-coupled "s" polarized incident light (shown in red) is reflected by the polarizing beam-splitter, and focused by a NIR objective to excite the sample. A linear polarizer is used to filter out the unwanted "p" component before the polarizing beam splitter (PBS). A 1/4 waveplate is placed before the objective with a high precision rotation mount.

One of the functions of the 1/4 waveplate is to change the polarization of the reflected light. When the 1/4 waveplate is at a certain angle, the laser light maintains its polarization upon reflection from the sample and is thus reflected at the bottom PBS. However, because the PBS is not perfect, some "s" polarization light can leak through the bottom PBS to the top PBS and be reflected to the CMOS camera. This light-path can be used for microscopy imaging purposes. The fluorescence light will have both "s" and "p" component, so that part of the fluorescence will also reach the CMOS camera. The majority of the "p" polarization component of the fluorescence light will go through the two PBS, and be collected through a single mode fiber to a single photon counting device. The 1/4 waveplate can also tune the reflected laser light to "p" polarization. In this configuration, laser light can easily go through the two PBS, and can be used as an alignment guide for the detection fiber-coupling.

Although not mentioned by Kuhlmann, it is also very common to used a weak 532nm CW laser to saturate the defect states in GaAs and increase the signal to noise level, during a resonance fluorescence experiment. This is integrated with a flip mirror next to the top PBS. Once the location of the aperture that contains QD is detected using the camera, we can flip down the flip mirror and use an "s" polarized 532nm CW laser light to excite the sample along with the tunable laser source.

The laser extinction ratio, meaning the reflected laser light to the detector divided by the excitation laser intensity, is an indirect measure of the signal to noise ratio of the setup. Kuhlmann mentioned that accurately tuning the 1/4 waveplate can help clean up the ellipticity caused by the objective and the sample, which increases

144
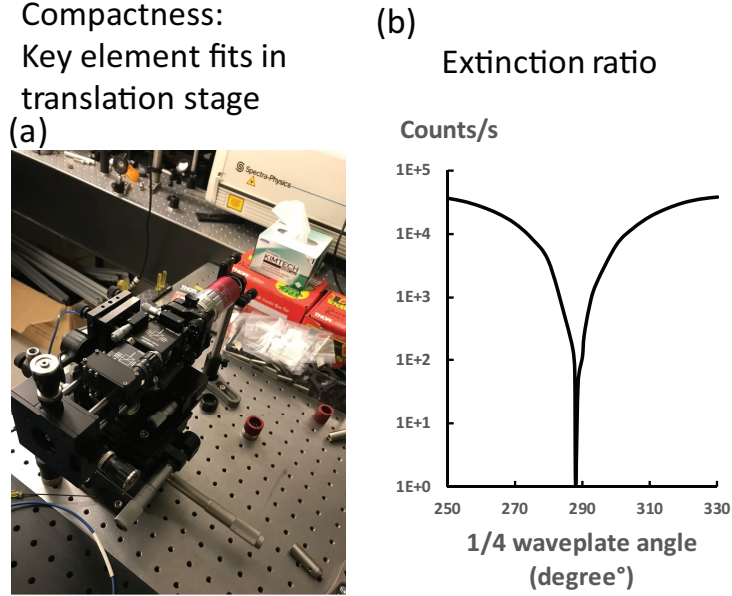
Figure A.2: Left: The resonance fluorescence setup build on a stage. Right: the extinction ratio tested with a reflected mirror

the laser extinction ratio from 10^5 to 10^8. Additionally, we discovered that switching the NIR long working distance objective lens to an aspheric objective lens can also improve the extinction ratio.

An ongoing effort towards building the RF setup is shown in Figure A.2(a). We integrated all the key optical elements of the RF setup shown before onto an x-z, tilt/yawn adjustable stage. We can easily switch our current micro-photoluminescence setup for this portable stage-based RF setup and adjust its position according to the sample's position/angle in the cryostat. We also measured the extinction ratio using a single photon counting module and our Sacher diode laser. We observed a maximum extinction ratio of 5×10^4 with the aspheric lens objective.

A.4 SEM Characterization of Resist for Side Wall Deposition

In chapter 8 we discussed characterizing the slope of the mesa. An SEM image viewing from the top of the mesa is shown in Figure A.3. We can found that the distance using a built-in function in the SEM that has an accuracy of around 15nm.
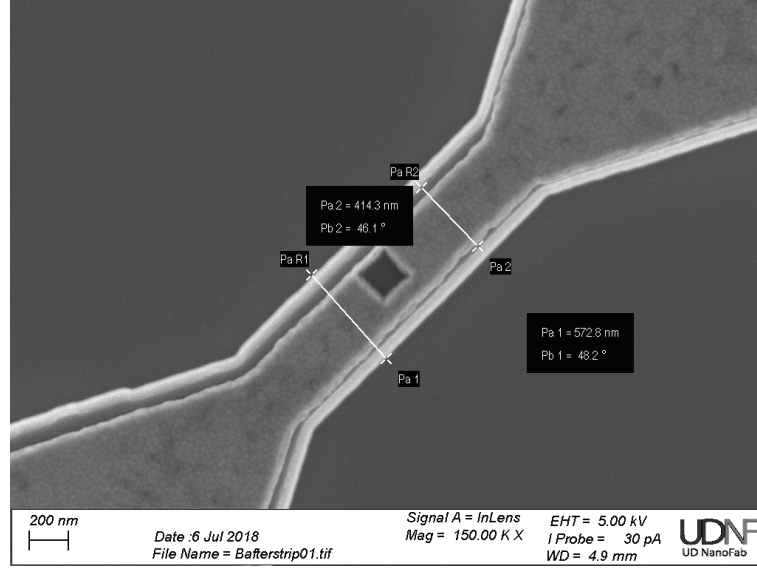
Figure A.3: A top down view of the mesa structure in the 3-electrode device

We surveyed through a series of these mesas on the device. We measured the top part of the mesa has an average width of 400nm $\pm$ 15nm and the bottom part of the mesa has an average width of 572nm $\pm$ 15nm. We also measured the height of the mesa using profilometer and found it to be around 330nm. The slope is deduced from these dimensions to be around $15° \pm 2°$.

A.5 Different QD Wavelength-dependent PL

In the characterization chapter, we mentioned using wavelength-dependent PL to test the Fermi level of the sample. Another QD's wavelength dependent data are shown in Figure A.4. The QD's emission peaks disappear when the excitation wavelength is higher than 830nm, similar to what we have shown before. However, we do see QD emissions at a different wavelength with a different fluence. This is likely due to the exciton defect interactions in the sample, as a result of a different level of saturation of the defects states under different excitation powers.
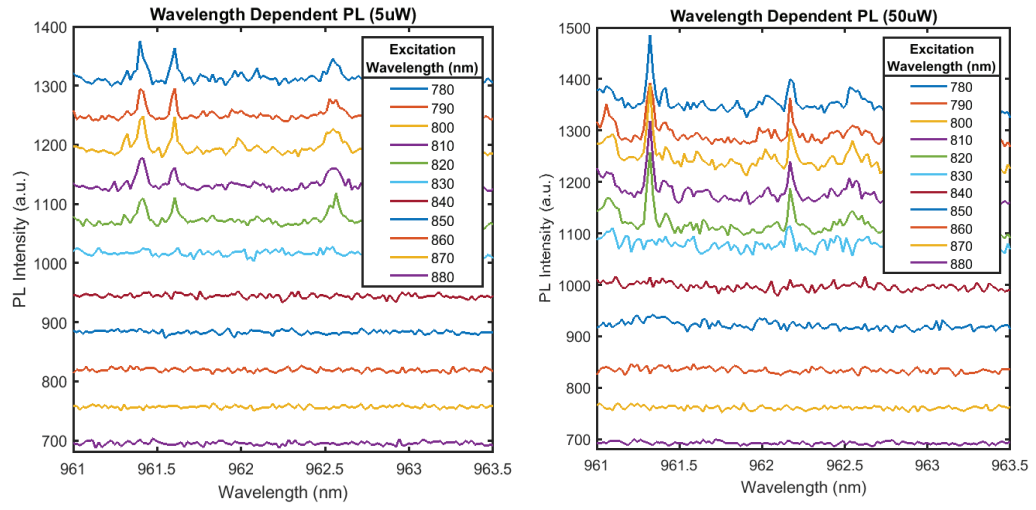
Figure A.4: A top down view of the mesa structure in the 3-electrode device

MATLAB CODE

Here we present the programs that calculate the finite matrix, stark shift, spin, and spin texture visualization.

B.1 Importdata

```matlab
1  % This file is used to import the hole states and electron
        states
2  % wavefunctions automatically from the tight-binding
        simulation. We
3  % will store the data in a matrix Hamiltomian "H". To
        maintain the
4  % calculation's accuracy, we will include 30 hole states and
        26 electron
5  % states.
6
7  title importdata
8  numfiles1 = 9;
9  numfiles2 = 20;
10 numfiles3=16;
11 H=zeros(56,550524,20);
12 j=20;
13
14 % The data file is arranged with names "holes_str.**" where
        the number in
```

```matlab
15  % the file name indicates the energy states. Because tight
       binding
16  % simulation treats holes as valence band electrons, there're
        no obvious
17  % difference in the file names between electron and hole
       states. The
18  % sequence of these energy states are determined by their
       corresponding
19  % energy level as indicated in "prob_cwc.holes_str" files.
       The general rule
20  % for file sequence is that each holes_str represent a block
       of hole states
21  % that's arranged in reverse order. It goes "holes_str" first
       , then "holes_str3"
22  % and then "holes_str2" in the order of energy. the top
       valence band hole states
23  % wavefunction is "holes_str.20" which corresponding to the
       energy of "61.7413meV".
24
25
26  for k = 1:numfiles1
27    holefilename = sprintf('holes_str.0%d',k);
28    holefile = importdata(holefilename,' ',1);
29    holefile=holefile.data;
30    holefile(:,1:4)=[];
31    H(j,:,:)=holefile;
32    j=j-1;
33  end
34
```

```matlab
for k = 10:numfiles2
    holefilename = sprintf('holes_str.%d', k);
    holefile = importdata(holefilename,' ',1);
    holefile=holefile.data;
    holefile(:,1:4)=[];
    H(j,:,:)=holefile;
    j=j-1;
end
j=20+numfiles2;

for k = 1:numfiles1
    holefilename = sprintf('holes_str3.0%d', k);
    holefile = importdata(holefilename,' ',1);
    holefile=holefile.data;
    holefile(:,1:4)=[];
    H(j,:,:)=holefile;
    j=j-1;
end

for k = 10:numfiles2
    holefilename = sprintf('holes_str3.%d', k);
    holefile = importdata(holefilename,' ',1);
    holefile=holefile.data;
    holefile(:,1:4)=[];
    H(j,:,:)=holefile;
    j=j-1;
end

j=40+numfiles3;
```

```matlab
for k = 1:numfiles1
    holefilename = sprintf('holes_str2.0%d', k);
    holefile = importdata(holefilename,' ',1);
    holefile=holefile.data;
    holefile(:,1:4)=[];
    H(j,:,:)=holefile;
    j=j-1;
end

for k = 10:numfiles3
    holefilename = sprintf('holes_str2.%d', k);
    holefile = importdata(holefilename,' ',1);
    holefile=holefile.data;
    holefile(:,1:4)=[];
    H(j,:,:)=holefile;
    j=j-1;
end

E0_1=importdata('prob_cwc.holes_str');
E0_2=importdata('prob_cwc.holes_str2');
E0_3=importdata('prob_cwc.holes_str3');

for i=1:16
    E0(i)=E0_2(i,2);
end
for i=17:36
    E0(i)=E0_3(i-16,2);
end
for i=37:56
```

```
93      E0(i)=E0_1(i−36,2);
94  end
95
96  % To sort the energy level so that the 1st energy is the
         lowest
97  E0=fliplr(E0);
98
99  % To convert the energy level to meV.
100  E0=E0*(1000);
101
102
103
104    Position=importdata('smallatoms25.3d');
105    PosScale=importdata('smallatoms25_scale.3d');
```

B.2   Finite matrix

```
1  % This is the calcuation of the finite matrix element for a
        number of hole
2  % states "Fstate" The calculation only has to be done once,
        which is why
3  % everything is quoted. The interaction terms are stored in
        VC for linear
4  % electric field, and GVC for gradient electric field.
5
6  Fstate=30;
7
8  %    WC=zeros(Fstate,Fstate,2,3);
9  %    VC=zeros(Fstate,Fstate,3);
10  %    GWC=zeros(Fstate,Fstate,2,3);
```

```matlab
11 %    GVC=zeros(Fstate,Fstate,3);
12 %
13 %       for m=1:Fstate
14 %            for n=1:Fstate
15 %                 for l=1:2
16 %                      for i=1:550524
17 %                      sump=0.0;
18 %                           for j=1:10
19 %                           sump=sump+H(m,i,2*j-1)*H(n,i,2*j-2+
    l)+H(m,i,2*j)*H(n,i,2*j-l+1)*((-1)^(l-1));
20 %                           end
21 %                           WC(m,n,l,1)=WC(m,n,l,1)+sump*PosScale(
    i,1);
22 %                           WC(m,n,l,2)=WC(m,n,l,2)+sump*PosScale(
    i,2);
23 %                           WC(m,n,l,3)=WC(m,n,l,3)+sump*PosScale(
    i,3);
24 %                           GWC(m,n,l,1)=GWC(m,n,l,1)+sump*
    PosScale(i,1)*PosScale(i,2);
25 %                           GWC(m,n,l,2)=GWC(m,n,l,2)+sump*
    PosScale(i,2)*PosScale(i,3);
26 %                           GWC(m,n,l,3)=GWC(m,n,l,3)+sump*
    PosScale(i,1)*PosScale(i,3);
27 %                      end
28 %                 end
29 %            VC(m,n,1)=complex(WC(m,n,1,1),WC(m,n,2,1));
30 %            VC(m,n,2)=complex(WC(m,n,1,2),WC(m,n,2,2));
31 %            VC(m,n,3)=complex(WC(m,n,1,3),WC(m,n,2,3));
```

```
32  %                           GVC(m,n,1)=complex(GWC(m,n,1,1),GWC(m,n,2,1))
        ;
33  %                           GVC(m,n,2)=complex(GWC(m,n,1,2),GWC(m,n,2,2))
        ;
34  %                           GVC(m,n,3)=complex(GWC(m,n,1,3),GWC(m,n,2,3))
        ;
35  %
36  %              end
37  %         end
38  %
```

B.3 Masterscript to calculate energies and spin wavefunctions with different electric field

```
1  % The following is used to generate hole wavefunctions with
       different
2  % electric field.
3
4  global Fstate;                % number of states that's included
        in the simulation
5  global Spindata;              % Matrix that contains the net
      spin value with different E field
6  global Energydata;            % Matrix that contains the energy
      value with different E field
7  global Enum;                  % The electric field index
8  global Enummax;               % The maximum number of electric
      field to include in the simulation
9  global Eper;                  % The matrix that contains the
      value of electric fields
```

```matlab
10  global Heigen;                    % The energy states wavefunction
        calculated with the finite matrix method
11  global NEK;                       % A matrix of energies of each
        eighen states with different electric field
12
13
14  Fstate=56;
15  Enummax=57;
16  Eper=zeros(1,Enummax);
17  imaster=1;
18
19  Spindata=zeros(Enummax,3);
20  Energydata=zeros(Enummax,4);
21  Heigen=zeros(Enummax,550524,20);         % Wavefunction
        after perturbation
22  NEK=zeros(Fstate,Enummax);
23
24  % Setting up the value of electric field and store it to
        matrix Eper
25
26  for Enum=1:19
27      Eper(Enum)=-200+10*(Enum-1);
28  end
29  for Enum=20:39
30      Eper(Enum)=-20+2*(Enum-19);
31  end
32  for Enum=40:Enummax
33      Eper(Enum)=Eper(39)+10*(Enum-39);
34  end
```

```matlab
35
36 % For each  electric  field ,  calculated  the  corresponding
       wavefunction  and
37 % energy  level .
38
39 for  Enum=1:Enummax
40 Perturbation ;
41 end
42
43 % The  following  code  is  used  to  determin  and  flip  the  ground
       hole  states
44 % and  second  lowest  hole  states ,  if  there 's  a  crossing/anti−
       crossing
45 % between  them .  This  happens  when  the  finite  matrix  can  not
       precisely
46 % predict  the  energy  level  of  the  hole  states  at  high
       electric  field
47 % (>100kV/cm)  and  the  bottom  two  states  flips  position .
       Usually  less  than  2
48 % flip  points  should  occur .  If  there 's  more  than  that ,  check
       the  previous
49 % code  for  correctness .
50
51 % DataStore ;
52 % imaster=1;
53
54 % Determine  the  number  of  switch  points  based  on  the  energy
       level
```

```
55  % difference. And store the crossing points to switchpoint
        matrix.
56
57  % for Enum=2:Enummax−1
58  %        if (( Energydata (1 ,Enum−1)−Energydata (2 ,Enum−1))>(
        Energydata (1 ,Enum)−Energydata (2 ,Enum)))
59  %              if (( Energydata (1 ,Enum)−Energydata (2 ,Enum))<(
        Energydata (1 ,Enum+1)−Energydata (2 ,Enum+1)))
60  %                   if ( abs ( Eper (Enum) ) > 20)
61  %                   Switchpoint ( imaster )=Enum;
62  %                   imaster=imaster +1;
63  %                   end
64  %              end
65  %        end
66  % end
67  % imaster=imaster −1;
68
69  % Flip the part with larger electric field if there's two
        switching points.
70  % The two switching points are usually symmetric and centered
         at 0 electric
71  % field. Recalculation the hole states wavefunction after the
        flip.
72
73  % if ( imaster == 2)
74  %          Heigencorrect=zeros (Enummax,550524 ,20);
75  %      for Enum=1:Enummax
76  %           if (Enum < Switchpoint (1) | Enum > Switchpoint (2))
77  %                Perturbation;
```

157

```matlab
78 %                    for j=1:Fstate
79 %                        for l=1:10
80 %                        Heigencorrect(Enum,:,2*l-1)=real(eigenV(j,
       eigenH(2,2)))*H(j,:,2*l-1)-imag(eigenV(j,eigenH(2,2)))*H(j
       ,:,2*l)+Heigencorrect(Enum,:,2*l-1);
81 %                        Heigencorrect(Enum,:,2*l)=imag(eigenV(j,
       eigenH(2,2)))*H(j,:,2*l-1)+real(eigenV(j,eigenH(2,2)))*H(j
       ,:,2*l)+Heigencorrect(Enum,:,2*l);
82 %                        end
83 %                    end
84 %                Heigen(Enum,:,:)=Heigencorrect(Enum,:,:);
85 %            end
86 %        end
87 % end
88
89 %Flip one side of the energy diagram if there's only one
90 %crossing/anti-crossing.
91
92
93 % if (imaster == 1)
94 %                Heigencorrect=zeros(Enummax,550524,20);
95 %        if (Eper(Switchpoint(1)) < 0)
96 %            for Enum=1:Switchpoint
97 %                Perturbation;
98 %                for j=1:Fstate
99 %                    for l=1:10
100 %                    Heigencorrect(Enum,:,2*l-1)=real(eigenV(j,
        eigenH(2,2)))*H(j,:,2*l-1)-imag(eigenV(j,eigenH(2,2)))*H(j
        ,:,2*l)+Heigencorrect(Enum,:,2*l-1);
```

```matlab
% 	                    Heigencorrect(Enum,:,2*l)=imag(eigenV(j,
% 	eigenH(2,2)))*H(j,:,2*l-1)+real(eigenV(j,eigenH(2,2)))*H(j
% 	,:,2*l)+Heigencorrect(Enum,:,2*l);
% 	                  end
% 	              end
% 	              Heigen(Enum,:,:)=Heigencorrect(Enum,:,:);
% 	          end
% 	      end
%
%       if (Eper(Switchpoint(1)) > 0)
% 	          for Enum=Switchpoint:Enummax
% 	              Perturbation;
% 	              for j=1:Fstate
% 	                  for l=1:10
% 	                  Heigencorrect(Enum,:,2*l-1)=real(eigenV(j,
% 	eigenH(2,2)))*H(j,:,2*l-1)-imag(eigenV(j,eigenH(2,2)))*H(j
% 	,:,2*l)+Heigencorrect(Enum,:,2*l-1);
% 	                  Heigencorrect(Enum,:,2*l)=imag(eigenV(j,
% 	eigenH(2,2)))*H(j,:,2*l-1)+real(eigenV(j,eigenH(2,2)))*H(j
% 	,:,2*l)+Heigencorrect(Enum,:,2*l);
% 	                  end
% 	              end
% 	              Heigen(Enum,:,:)=Heigencorrect(Enum,:,:);
% 	          end
% 	      end
% end
Spin;
```

B.4 Perturbation

```matlab
% This is the calcuation of the finite matrix element for a
    number of hole
% states "Fstate" The calculation only has to be done once,
    which is why
% everything is quoted. The interaction terms are stored in
    VC for linear
% electric field, and GVC for gradient electric field.

% Fstate=56;
%
%     WC=zeros(Fstate, Fstate, 2, 3);
%     VC=zeros(Fstate, Fstate, 3);
%     GWC=zeros(Fstate, Fstate, 2, 3);
%     GVC=zeros(Fstate, Fstate, 3);
%
%       for m=1:Fstate
%           for n=1:Fstate
%               for l=1:2
%                   for i=1:550524
%                   sump=0.0;
%                       for j=1:10
%                       sump=sump+H(m, i, 2*j-1)*H(n, i, 2*j-2+
    l)+H(m, i, 2*j)*H(n, i, 2*j-l+1)*((-1)^(l-1));
%                       end
%                   WC(m, n, l, 1)=WC(m, n, l, 1)+sump*PosScale(
    i, 1);
%                   WC(m, n, l, 2)=WC(m, n, l, 2)+sump*PosScale(
    i, 2);
```

160

```matlab
23 %                                 WC(m,n,l,3)=WC(m,n,l,3)+sump*PosScale(
       i,3);
24 %                                 GWC(m,n,l,1)=GWC(m,n,l,1)+sump*
       PosScale(i,1)*PosScale(i,2);
25 %                                 GWC(m,n,l,2)=GWC(m,n,l,2)+sump*
       PosScale(i,2)*PosScale(i,3);
26 %                                 GWC(m,n,l,3)=GWC(m,n,l,3)+sump*
       PosScale(i,1)*PosScale(i,3);
27 %                             end
28 %                        end
29 %                 VC(m,n,1)=complex(WC(m,n,1,1),WC(m,n,2,1));
30 %                 VC(m,n,2)=complex(WC(m,n,1,2),WC(m,n,2,2));
31 %                 VC(m,n,3)=complex(WC(m,n,1,3),WC(m,n,2,3));
32 %                 GVC(m,n,1)=complex(GWC(m,n,1,1),GWC(m,n,2,1))
       ;
33 %                 GVC(m,n,2)=complex(GWC(m,n,1,2),GWC(m,n,2,2))
       ;
34 %                 GVC(m,n,3)=complex(GWC(m,n,1,3),GWC(m,n,2,3))
       ;
35 %
36 %             end
37 %         end
38 %
39 %
40
41 F(1)=0.0;          % x direction E field   mV/Ans
42 F(2)=0.0;                % y direction mV/Ans
43 F(3)=0.01*Eper(Enum);              % z direction in   mV/Ans
44
```

161

```matlab
45      G=0.000;
46      G2=0;
47
48  % This is to calculate the potential at each individual
          atomic site. It's
49  % not required for finite matrix calculation.
50
51  for i=1:550524
52      PosScale(i,8)=((F(1)+G*PosScale(i,3)+G2*PosScale(i,1))*
          PosScale(i,1)+PosScale(i,2)*F(2)+PosScale(i,3)*(F(3)+G
          *(PosScale(i,1))-G2*(PosScale(i,3))));       % Potential
          at each point
53  end
54
55  V=zeros(Fstate,Fstate);
56
57      for m=1:Fstate
58          for n=1:Fstate
59              V(m,n)=VC(m,n,1)*F(1)+VC(m,n,2)*F(2)+VC(m,n,3)*F
                  (3)+2*G*GVC(m,n,3);
60          end
61      end
62
63  M2=V;
64
65  for i=1:Fstate
66      M2(i,i)=E0(i)+V(i,i);
67  end
68
```

```matlab
69  NE=sort(real(eig(M2)));
70  NEK(:,Enum)=NE(:);
71
72  eigenV=zeros(Fstate,Fstate);                    % eigenvector
        after perturbation
73  eigenD=zeros(Fstate,Fstate);                    % diagonalized
        matrix after perturbation
74  eigenH=zeros(Fstate,Fstate);
75
76
77  eigenH=eig(M2);
78  [eigenV,eigenD]=eig(M2);
79
80  eigenH(:,2)=[1:Fstate];
81  eigenH(:,1)=real(eigenH(:,1));
82  eigenH=sortrows(eigenH,[1]);
83  eigenH=flipud(eigenH);
84
85  for j=1:Fstate
86      for l=1:10
87          Heigen(Enum,:,2*l-1)=real(eigenV(j,eigenH(1,2)))*H(j,:,2*
                l-1)-imag(eigenV(j,eigenH(1,2)))*H(j,:,2*l)+Heigen(
                Enum,:,2*l-1);
88          Heigen(Enum,:,2*l)=imag(eigenV(j,eigenH(1,2)))*H(j,:,2*l
                -1)+real(eigenV(j,eigenH(1,2)))*H(j,:,2*l)+Heigen(Enum
                ,:,2*l);
89      end
90  end
```

B.5 Stark shift calculation

```matlab
1  % This script calculated the starkshift of an arbituary
       electric field
2  % given the finite matrix Hamiltonian.
3
4  Enummax=50;              % Define the number of electric fields
5  Eper=zeros(1,Enummax);     % Define the matrix that contains
       the electric field at each direction
6
7  for Enum=1:Enummax
8      Eper(Enum)=-100+(Enum-1)*4;  % Define Eper in kV/cm
9
10
11  F(1)=0.0;           % x direction E field  mV/Ans
12  F(2)=0.0;             % y direction mV/Ans
13  F(3)=0.01*Eper(Enum);            % z direction in  mV/Ans
14
15      G=0.000;
16      G2=0;
17  for i=1:550524
18      PosScale(i,8)=((F(1)+G*PosScale(i,3)+G2*PosScale(i,1))*
          PosScale(i,1)+PosScale(i,2)*F(2)+PosScale(i,3)*(F(3)+G
          *(PosScale(i,1))-G2*(PosScale(i,3))));     % Potential
          at each point
19  end
20
21
22  V=zeros(Fstate,Fstate);
```

```matlab
23
24
25      for m=1:Fstate
26          for n=1:Fstate
27              V(m,n)=VC(m,n,1)*F(1)+VC(m,n,2)*F(2)+VC(m,n,3)*F
                    (3)+2*G*GVC(m,n,3);
28          end
29      end
30
31  M2=V;
32
33  for i=1:Fstate
34      M2(i,i)=E0(i)+V(i,i);
35  end
36
37  NE=sort(real(eig(M2)));
38  NEK(:,Enum)=NE(:);
39
40  eigenV=zeros(Fstate,Fstate);                % eigenvector
        after perturbation
41  eigenD=zeros(Fstate,Fstate);                % eigen value
        after perturbation
42  eigenH=zeros(Fstate,Fstate);
43
44
45  eigenH=eig(M2);
46  [eigenV,eigenD]=eig(M2);
47
48  eigenH(:,2)=[1:Fstate];
```

165

```matlab
49  eigenH(:,1)=real(eigenH(:,1));
50  eigenH=sortrows(eigenH,[1]);
51  eigenH=flipud(eigenH);
52  end
53  StarkshiftE001=zeros(3,Enummax);
54
55  for i=1:Enummax
56      StarkshiftE001(1,i)= Eper(i);
57      StarkshiftE001(2,i)= NEK(56,i);
58      StarkshiftE001(3,i)= NEK(55,i);
59  end
```

B.6   Spin wavefunction calculation

```matlab
1  sumplus=zeros(1,Enummax);
2  summinus=zeros(1,Enummax);
3  k=1;
4
5  Sz1=zeros(550524,Enummax);
6  Sx1=zeros(550524,Enummax);
7  Sy1=zeros(550524,Enummax);
8
9  for k=1:Enummax
10   H30e=squeeze(Heigen(k,:,:));
11  % H30e=squeeze(H(k,:,:));
12  HP30=power(H30e,2);
13  PH30=sum(HP30,2);
14  FinalH30=[Position,PH30];
15
16
```

```matlab
17  for i=1:10
18      H30ezup(:,i)=H30e(:,i);
19      H30ezdown(:,i)=H30e(:,i+10);
20  end
21
22  Szup(:,k)=sum(power(H30ezup,2),2);
23  Szdown(:,k)=sum(power(H30ezdown,2),2);
24
25  for i=1:550524
26      for j=1:10
27      Sz1(i,k)=Sz1(i,k)+H30ezup(i,j)^2-H30ezdown(i,j)^2;
28      Sx1(i,k)=Sx1(i,k)+2*H30ezup(i,j)*H30ezdown(i,j);
29      end
30      for j=1:5
31      Sy1(i,k)=Sy1(i,k)-2*H30ezup(i,2*j)*H30ezdown(i,2*j-1)+2*
                H30ezup(i,2*j-1)*H30ezdown(i,2*j);
32      end
33  end
34
35
36
37  l=1;
38  j=1;
39  for i=1:550524
40      if(FinalH30(i,1)+FinalH30(i,2) > 0)
41          sumplus(k)=sumplus(k)+FinalH30(i,8);
42          Szupplus(k,l)=Szup(i,k);
43          Szdownplus(k,l)=Szdown(i,k);
44          l=l+1;
```

```
45        else
46            summinus(k)=summinus(k)+FinalH30(i,8);
47            Szupminus(k,j)=Szup(i,k);
48            Szdownminus(k,j)=Szdown(i,k);
49            j=j+1;
50        end
51    end
52
53    Sz1sum(k)=sum(Sz1(:,k));
54    Sx1sum(k)=sum(Sx1(:,k));
55    Sy1sum(k)=sum(Sy1(:,k));
56
57
58    end
59    %
60    % Szplus=sum(Szupplus,2)-sum(Szdownplus,2);
61    % Szminus=sum(Szupminus,2)-sum(Szdownminus,2);
```

B.7 Spin binning and integration

```
1    % This is the program that bins the atomic sites and
         summarize all spin in
2    % the quantum dot to a single plane. This programs works but
         there's a
3    % different way to solve this problem: Create a mesh matrix
         that contains the
4    % coordinates a (x,y) plane, where each mesh-grid covers one/
         several basis of
5    % Ga-As atomic site. Then search through the position file
         and allocate the
```

```matlab
6  % spin data accordingly to the grid. I suspect this will cost
         more time but
7  % I could be wrong.
8
9  Enum=29;
10 binfactor=2;                    % binfactor is related to numbers
         of atoms to bin
11 zlowlimit=-0.5;                 % lower bond of the single QD
12 zhighlimit=9.5;                 % higher bond of the single QD
13
14 % Addin the atomistic spin information into position matrix.
15
16 for i=1:550524
17      Position(i,8)=i;
18      Position(i,9)=Sx1(i,Enum);
19      Position(i,10)=Sy1(i,Enum);
20      Position(i,11)=Sz1(i,Enum);
21 end
22 j=1;
23
24 % Create a different position2 matrix that contains all the
         original
25 % information, while conbining the cation sites and anion
         sites into the
26 % same coordinate.
27
28 Position2=zeros(550524,11);
29 for i=1:length(Position(:,1))
```

```matlab
        if ( Position ( i ,7 )  ==  1 )
                                                                    % As sites
                Position2 ( j ,:)=Position ( i ,:) ;
                j=j +1;
        else
                Position2 ( j ,1:3)=Position ( i ,1:3) −0.25;
                                                    % Ga sites
                Position2 ( j ,4:11)=Position ( i ,4:11) ;
                j=j +1;
        end
    end

% Create the binned position/spin matrix and sort the matrix with different
% Z value .

binning=Position2 ;
binning=sortrows ( binning ,[3]) ;

% Select one of the z plane values and extract all the data into
% binningplot .

j =1;
Zp=−0.5;
for  i =1:length ( Position2 (: ,1) )
    if ( binning ( i ,3)  ==  Zp)
        binningplot ( j ,:)=binning ( i ,:) ;
        j=j +1;
```

```matlab
55         end
56     end
57
58  % Find the atomic site in Position2 where there x and y
         location matches
59  % the ones in binningplot, and integrate their spin data.
60
61  for i=1:550524
62      for j=1:length(binningplot(:,1))
63          if(Position(i,3) > zlowlimit && Position(i,3) <
                zhighlimit && Position2(i,1)==binningplot(j,1) &&
                Position2(i,2)==binningplot(j,2))
64              binningplot(j,9:11)=binningplot(j,9:11)+
                    Position2(i,9:11);
65          end
66      end
67  end
68
69  % further binning the data in (x,y) plane by 2.
70
71  for i=1:length(binningplot(:,1))
72      if(mod(binningplot(i,2),1) ~= 0)
73          binningplot(i,2)=binningplot(i,2)-0.5;
74      end
75      if(mod(binningplot(i,1),1) ~= 0)
76          binningplot(i,1)=binningplot(i,1)-0.5;
77      end
78  end
79  i=2;
```

```matlab
80   while ( i < length ( binningplot (: ,1) ) )
81       if (  binningplot ( i ,1) == binningplot ( i −1,1) &&
             binningplot ( i ,2) == binningplot ( i −1,2) )
82           binningplot ( i −1,9:11)=binningplot ( i −1,9:11)+
                 binningplot ( i ,9:11) ;
83           binningplot ( i ,:) =[];
84       else
85           i=i +1;
86       end
87   end
88
89   % At this point , binningplot should contains limit amount of
        x ,y site and
90   % their coordinate should be integer . each site should
         contain the
91   % information of the wavefunction/spin amplitude integral
         around that (x ,y) location .
92   % We would like to further reduce the x ,y sites to make the
         spin diagram
93   % more visually appealing .
94
95   % This following binning sequence is specifically written to
         accommodate
96   % the data structure of the x and y coordianates . The concept
          is to bin
97   % every y coordinates while maintaining the same x .  The data
         is then stored at
98   % matrix binningxbin .
99
```

172

```
100  binningplot=sortrows(binningplot,[1]);
101
102  binningxbin=zeros(round(length(binningplot(:,1))/(binfactor))
        +1,11);
103  j=1;
104  k=1;
105  for i=1:length(binningplot(:,1))-1
106      binningxbin(j,1)=binningplot(i,1);
107      binningxbin(j,2)=binningxbin(j,2)+binningplot(i,2);
108      binningxbin(j,3)=binningplot(i,3);
109      binningxbin(j,4:8)=binningplot(i,4:8);
110      binningxbin(j,9)=binningxbin(j,9)+binningplot(i,9);
111      binningxbin(j,10)=binningxbin(j,10)+binningplot(i,10);
112      binningxbin(j,11)=binningxbin(j,11)+binningplot(i,11);
113  if (mod(k,binfactor) ~= 0 && binningplot(i,1) ~= binningplot(
        i+1,1))
114          binningxbin(j,2)=binningxbin(j,2)/k;
115              k=1;
116              j=j+1;
117      elseif (mod(k,binfactor) ~= 0)
118              k=k+1;
119      elseif (mod(k,binfactor) == 0 && binningplot(i,1) ==
            binningplot(i-1,1))
120              binningxbin(j,2)=binningxbin(j,2)/binfactor;
121              k=1;
122              j=j+1;
123      end
124  end
125
```

```matlab
126  % This following code does a similar job except in a
         different direction.

127

128  binningxbin=sortrows(binningxbin,[2]);
129  binningxbinybin=zeros(round(length(binningxbin(:,1))/(
         binfactor-1))+1,11);
130  j=1;
131  k=1;
132  for i=1:length(binningxbin(:,1))-1
133      binningxbinybin(j,1)=binningxbinybin(j,1)+binningxbin(i
             ,1);
134      binningxbinybin(j,2)=binningxbin(i,2);
135      binningxbinybin(j,3)=binningxbin(i,3);
136      binningxbinybin(j,4:8)=binningxbin(i,4:8);
137      binningxbinybin(j,9)=binningxbinybin(j,9)+binningxbin(i
             ,9);
138      binningxbinybin(j,10)=binningxbinybin(j,10)+binningxbin(i
             ,10);
139      binningxbinybin(j,11)=binningxbinybin(j,11)+binningxbin(i
             ,11);
140      if (mod(k,binfactor) ~= 0 && binningxbin(i,2) ~=
             binningxbin(i+1,2))
141          binningxbinybin(j,1)=binningxbinybin(j,1)/k;
142          k=1;
143          j=j+1;
144      elseif (mod(k,binfactor) ~= 0)
145          k=k+1;
146      elseif (mod(k,binfactor) == 0 && binningxbin(i,2) ==
             binningxbin(i-1,2))
```

```matlab
147             binningxbinybin(j,1)=binningxbinybin(j,1)/
                   binfactor;
148             k=1;
149             j=j+1;
150       end
151       if i == length(binningxbin(:,1))-1
152             binningxbinybin(j,1)=round(binningxbinybin(j,1)/
                   binfactor);
153       end
154 end
155
156 % At the end, we will simplify the matrix binningxbinybin and
       eliminate all
157 % the emply elements.
158
159 k=1;
160 while (k < length(binningxbinybin(:,1)))
161     k=k+1;
162     if (binningxbinybin(k,7) == 0)
163         binningxbinybin(k,:) =[];
164         k=k-1;
165     end
166 end
167 %
168 % for i=1:length(binningxbinybin(:,2))
169 %     if mod(binningxbinybin(i,2),1) ~= 0
170 %         binningxbinybin(i,2)=binningxbinybin(i,2)+0.5;
171 %     end
172 %     if mod(binningxbinybin(i,1),1) ~= 0
```

```matlab
173 %              binningxbinybin(i,1)=binningxbinybin(i,1)+0.5;
174 %        end
175 % end
176 % %
177 % binningxbinybin=sortrows(binningxbinybin,[2,1]);
178 % binningxbinybin2=zeros(length(binningxbinybin(:,1)),11);
179 % j=1;
180 % for i=1:length(binningxbinybin(:,1))-1
181 %        binningxbinybin2(j,1)=binningxbinybin(i,1);
182 %        binningxbinybin2(j,2)=binningxbinybin(i,2);
183 %        binningxbinybin2(j,3)=binningxbinybin(i,3);
184 %        binningxbinybin2(j,4:8)=binningxbinybin(i,4:8);
185 %        binningxbinybin2(j,9)=binningxbinybin2(j,9)+
         binningxbinybin(i,9);
186 %        binningxbinybin2(j,10)=binningxbinybin2(j,10)+
         binningxbinybin(i,10);
187 %        binningxbinybin2(j,11)=binningxbinybin2(j,11)+
         binningxbinybin(i,11);
188 %        if binningxbinybin(i,1) ~= binningxbinybin(i+1,1)
189 %              j=j+1;
190 %        end
191 % end
192
193 % for k=1:length(binningxbinybin2(:,1))
194 %        if (binningxbinybin2(k,6) == 0)
195 %              binningxbinybin2(k:length(binningxbinybin2(:,1)),:)
         =[];
196 %              break;
197 %        end
```
176

```matlab
% end
%
%
% clear Xplane Xpos Yplane Ypos Zplane Zpos Sxplane Syplane
     Szplane;
% j=1;
% Xplane=zeros(length(binningxbinybin2(:,1)),1);
% Yplane=zeros(length(binningxbinybin2(:,1)),1);
% Zplane=zeros(length(binningxbinybin2(:,1)),1);
% Xpos=zeros(length(binningxbinybin2(:,1)),1);
% Ypos=zeros(length(binningxbinybin2(:,1)),1);
% Zpos=zeros(length(binningxbinybin2(:,1)),1);
% Sxplane=zeros(length(binningxbinybin2(:,1)),1);
% Syplane=zeros(length(binningxbinybin2(:,1)),1);
% Szplane=zeros(length(binningxbinybin2(:,1)),1);
% Zactual=zeros(length(binningxbinybin2(:,1)),1);
%
% for i=1:length(binningxbinybin2(:,1))
%           Xplane(j)=binningxbinybin2(i,1)*0.565;
%           Xpos(j)=binningxbinybin2(i,1);
%           Yplane(j)=binningxbinybin2(i,2)*0.565;
%           Ypos(j)=binningxbinybin2(i,1);
%           Zplane(j)=(zlowlimit+zhighlimit)*0.565/2;
%           Zpos(j)=Position(binningxbinybin2(i,8),3);
%           Zactual(j)=PosScale(binningxbinybin2(i,8),3)/10;
%           Sxplane(j)=binningxbinybin2(i,9);
%           Syplane(j)=binningxbinybin2(i,10);
%           Szplane(j)=binningxbinybin2(i,11);
%           j=j+1;
```

```matlab
226  % end
227  % for  i=1:length(Sxplane)
228  %        Sxplane(i)=Sxplane(i)*Magnification;
229  %        Syplane(i)=Syplane(i)*Magnification;
230  %        Szplane(i)=Szplane(i)*Magnification;
231  % end
```

B.8   Spin texture generation (1 graph)

```matlab
1   % Spin  distribution  in  z=0  plane
2    Zp=1; % Zplane  value
3   Enum=29;
4    Magnification=200;
5
6
7    clear  Xplane  Xpos  Yplane  Ypos  Zplane  Zpos  Sxplane  Syplane
         Szplane;
8    %
9    binningxyz;
10   j=1;
11   Xplane=zeros(length(binningxbinybin(:,1)));
12   Yplane=zeros(length(binningxbinybin(:,1)));
13   Zplane=zeros(length(binningxbinybin(:,1)));
14   Xpos=zeros(length(binningxbinybin(:,1)));
15   Ypos=zeros(length(binningxbinybin(:,1)));
16   Zpos=zeros(length(binningxbinybin(:,1)));
17   Sxplane=zeros(length(binningxbinybin(:,1)));
18   Syplane=zeros(length(binningxbinybin(:,1)));
19   Szplane=zeros(length(binningxbinybin(:,1)));
20   Zactual=zeros(length(binningxbinybin(:,1)));
```

```matlab
21

22

23

24  for i=1:length(binningxbinybin(:,1))
25          Xplane(j)=PosScale(binningxbinybin(i,8),1)/10;
26          Xpos(j)=Position(binningxbinybin(i,8),1);
27          Yplane(j)=PosScale(binningxbinybin(i,8),2)/10;
28          Ypos(j)=Position(binningxbinybin(i,8),2);
29          Zplane(j)=Zp*0.565;
30          Zpos(j)=Position(binningxbinybin(i,8),3);
31          Zactual(j)=PosScale(binningxbinybin(i,8),3)/10;
32          Sxplane(j)=binningxbinybin(i,9);
33          Syplane(j)=binningxbinybin(i,10);
34          Szplane(j)=binningxbinybin(i,11);
35          j=j+1;
36  end
37  for i=1:length(Sxplane)
38      Sxplane(i)=Sxplane(i)*Magnification;
39      Syplane(i)=Syplane(i)*Magnification;
40      Szplane(i)=Szplane(i)*Magnification;
41      Xplane(i)=Xplane(i)-1;
42      Yplane(i)=Yplane(i)-1;
43  end
44  figurespin=figure('units','normalized','position',[.1 .1 0.8
        0.8],'Color',[0.8 0.8 0.8],'Visible','on');
45  set(gca,'FontSize',16);

46

47

48  % ha_topdown=subplot(5,5,1);
```

```matlab
49  % % Dome;
50  %
51  % for i=1:length(Sxplane)
52  %       arrowhandle=arrow3Dmaxy([Xplane(i),Yplane(i),Zplane(i)
           ],[Sxplane(i),Syplane(i),Szplane(i)],'r',0.65);
53  %       set(arrowhandle(1), 'FaceColor', [0.2,0.4,0.9]);
54  %       set(arrowhandle(2), 'FaceColor', [0.9,0.2,0]);
55  %       arrowhandle(1, 1).AmbientStrength=0.7;
56  %       arrowhandle(1, 2).AmbientStrength=0.7;
57  %       arrowhandle(1, 2).DiffuseStrength=0.9;
58  %       hold on;
59  % end
60  % if (mod(Zp*4,2) == 0)
61  %       title(['all plane top down'], 'FontSize',18);
62  % else
63  %       title(['all plane top down'], 'FontSize',18);
64  % end
65  % xlabel('x','FontSize',16,'Position',[0,-10,-9.5]);
66  % ylabel('y','FontSize',16,'Position',[10,0.5,-9.5]);
67  % zlabel('z','FontSize',16,'Position',[-9.5,-9,0]);
68  % axis([-8.5 8.5 -8.5 8.5 -2 2]);
69  % ha_topdown.CameraPosition=[6.3457 , -27.0545 , 144.5780];
70  % ha_topdown.Projection='perspective';
71  % ha_topdown.Position=[0.0556  ,  0.4366 ,  0.2570 ,
           0.4786];
72  % ha_topdown.Color=[1,1,1];
73  % ha_topdown.GridColor
           =[0.313725490196078,0.313725490196078,0.313725490196078];
74  % lighting gouraud;
```

```matlab
75  % camlight right;
76
77  % ha_45=subplot(5,5,3);
78  % for i=1:length(Sxplane)
79  %      arrowhandle=arrow3Dmaxy([Xplane(i),Yplane(i),Zplane(i)
        ],[Sxplane(i),Syplane(i),Szplane(i)],'r',0.65);
80  %      set(arrowhandle(1), 'FaceColor', [0.2,0.4,0.9]);
81  %      set(arrowhandle(2), 'FaceColor', [0.9,0.2,0]);
82  %      arrowhandle(1, 1).AmbientStrength=0.7;
83  %      arrowhandle(1, 2).AmbientStrength=0.7;
84  %      arrowhandle(1, 2).DiffuseStrength=0.9;
85  %      hold on;
86  % end
87  % if (mod(Zp*4,2) == 0)
88  %      title(['all plane 45 degree'], 'FontSize',18);
89  % else
90  %      title(['all plane 45 degree'], 'FontSize',18);
91  % end
92  % xlabel('x','FontSize',16,'Position',[0,-10,-9.5]);
93  % ylabel('y','FontSize',16,'Position',[10,0.5,-9.5]);
94  % zlabel('z','FontSize',16,'Position',[-9.5,-9,0]);
95  % axis([-8.5 8.5 -8.5 8.5 -2 2]);
96  % ha_45.CameraPosition=[33.8820, -111.1006 , 34.7658];
97  % ha_45.Projection='perspective';
98  % ha_45.Position=[0.3806 , 0.4610 , 0.2500 , 0.40];
99  % ha_45.Color=[1,1,1];
100 % ha_45.GridColor
        =[0.313725490196078,0.313725490196078,0.313725490196078];
101 % lighting gouraud;
```

```matlab
102 % camlight right;
103
104 ha_flat=subplot(5,5,5);
105 for i=1:length(Sxplane)
106     arrowhandle=arrow3Dmaxy([Xplane(i),Yplane(i),Zplane(i)],[
            Sxplane(i),Syplane(i),Szplane(i)],'r',0.65);
107     set(arrowhandle(1), 'FaceColor', [0.2,0.4,0.9]);
108     set(arrowhandle(2), 'FaceColor', [0.9,0.2,0]);
109     arrowhandle(1, 1).AmbientStrength=0.7;
110     arrowhandle(1, 2).AmbientStrength=0.7;
111     arrowhandle(1, 2).DiffuseStrength=0.9;
112     hold on;
113 end
114 if (mod(Zp*4,2) == 0)
115     title(['all plane flat'], 'FontSize',18);
116 else
117     title(['all plane flat'], 'FontSize',18);
118 end
119 xlabel('x','FontSize',16,'Position',[0,-10,-9.5]);
120 ylabel('y','FontSize',16,'Position',[10,0.5,-9.5]);
121 zlabel('z','FontSize',16,'Position',[-9.5,-9,0]);
122 axis([-8.5 8.5 -8.5 8.5 -2 2]);
123 ha_flat.CameraPosition=[51.3208 ,-109.7842 ,    3.6881];
124 ha_flat.Projection='perspective';
125 ha_flat.Position=[0.71 ,    0.4679 ,    0.25,    0.4];
126 ha_flat.Color=[1,1,1];
127 ha_flat.GridColor
        =[0.313725490196078,0.313725490196078,0.313725490196078];
128 lighting gouraud;
```

```matlab
129  camlight right;

130

131

132

133

134

135  % hold on;
136  % hb=subplot(5,5,21);
137  % arrowhandle=arrow3Dmaxy4([0,0,0],[1/sqrt(2),1/sqrt(2),0],'r
         ',0.5);
138  %      set(arrowhandle(1), 'FaceColor', [0.6,0.4,0.9]);
139  %      set(arrowhandle(2), 'FaceColor', [0.5,0.2,0.8]);
140  %      arrowhandle(1, 1).AmbientStrength=0.7;
141  %      arrowhandle(1, 2).AmbientStrength=0.7;
142  %      arrowhandle(1, 2).DiffuseStrength=0.9;
143  % xlabel('Bx','FontSize',10,'Position',[0,-1.5,-0.65]);
144  % ylabel('By','FontSize',10,'Position',[1.5,0,-0.5]);
145  % zlabel('Bz','FontSize',10,'Position',[-1.2,-1.2,0]);
146  % title('Magnetic Field B(1,1,0) 1(T)','FontSize',10);
147  % axis([-1 1 -1 1 -0.5 0.5]);
148  % hb.CameraPosition=[   53.0738  ,-223.3648 ,   35.1549];
149  % % he.Parent.PlotBoxAspectRatio
         =[1,0.780025875322314,0.425423608921794];
150  % hb.Position=[0.0637 ,    0.0945  ,  0.1820  ,   0.1610];
151  % hb.Projection='perspective';
152  % hb.LineWidth=1;
153  % hb.GridColor
         =[0.313725490196078,0.313725490196078,0.313725490196078];
154  % hb.GridAlpha=0.2;
```

```matlab
155 % lighting gouraud;
156 % camlight right;
157
158 %
159 % hold on;
160 % hs=subplot(5,5,23);
161 %
162 % arrowhandle=arrow3Dmaxy4([0,0,0],[Sx1sum(Enum),Sy1sum(Enum)
        ,Sz1sum(Enum)],'r',0.5);
163 %     set(arrowhandle(1), 'FaceColor', [0.2,0.4,0.9]);
164 %     set(arrowhandle(2), 'FaceColor', [0.9,0.2,0]);
165 %     arrowhandle(1, 1).AmbientStrength=0.7;
166 %     arrowhandle(1, 2).AmbientStrength=0.7;
167 %     arrowhandle(1, 2).DiffuseStrength=0.9;
168 % xlabel('Sx','FontSize',10,'Position',[0,-1.2,-1.2]);
169 % ylabel('Sy','FontSize',10,'Position',[1.2,0,-1.2]);
170 % zlabel('Sz','FontSize',10,'Position',[-1.2,-1.2,0]);
171 % Stitle=sprintf('Net Spin Sx=%.1d, Sy=%.1d, Sz=%.1d',Sx1sum(
        Enum),Sy1sum(Enum),Sz1sum(Enum));
172 % title(Stitle,'Fontsize',13);
173 % axis([-1 1 -1 1 -1 1]);
174 % hs.CameraPosition=[5.1447 , -15.9800 ,   4.2626];
175 % hs.LineWidth=1;
176 % hs.Position=[0.4223 ,   0.0705 ,  0.1860 ,  0.2740];
177 % hs.Projection='perspective';
178 % hs.GridColor
        =[0.313725490196078,0.313725490196078,0.313725490196078];
179 % hs.GridAlpha=0.2;
180 % lighting gouraud;
```

184

```matlab
181  % camlight right;
182
183
184
185  % subplot(5,5,24);
186  % hs2=quiver(0,0,Sx1sum(Enum),Sy1sum(Enum));
187  % xlabel('Sx','FontSize',10);
188  % ylabel('Sy','FontSize',10);
189  % hs2.LineWidth=2;
190  % hs2.MaxHeadSize=2;
191  % hs2.Parent.Position=[0.6184 ,    0.1439    , 0.0582 ,
          0.0904];
192  % hs2.Parent.CameraUpVector=[−0.0411 ,    0.0912    ,        0]
193  % hs2.Color=[0.9,0.2,0.2];
194
195
196  %
197  % hold on;
198  % he=subplot(5,5,25);
199  % if (abs(Eper(Enum)) > 25)
200  % arrowhandle=arrow3Dmaxy3([0,0,0],[−Eper(Enum)/sqrt(2),Eper(
          Enum)/sqrt(2),0],'r',0.5);
201  %     set(arrowhandle(1), 'FaceColor', [0.1,0.8,0.2]);
202  %     set(arrowhandle(2), 'FaceColor', [0.1,0.8,0.5]);
203  %     arrowhandle(1, 1).AmbientStrength=0.7;
204  %     arrowhandle(1, 2).AmbientStrength=0.7;
205  %     arrowhandle(1, 2).DiffuseStrength=0.9;
206  %
207  % xlabel('Ex','FontSize',10,'Position',[0,−250,−230]);
```

```matlab
208 % ylabel('Ey','FontSize',10,'Position',[250,0,-180]);
209 % zlabel('Ez','FontSize',10,'Position',[-230,-230,0]);
210 % Etitle=sprintf('Electric Field (-1,1,0) %d(kV/cm)',Eper(
        Enum));
211 % title(Etitle,'Fontsize',10);
212 % axis([-180 180 -180 180 -180 180]);
213 % he.CameraPosition=[597.8 ,-2424.8, 1866.3];
214 % he.Projection='perspective';
215 % he.LineWidth=1;
216 % else
217 % arrowhandle=arrow3Dmaxy2([0,0,0],[-Eper(Enum)/sqrt(2),Eper(
        Enum)/sqrt(2),0],'r',0.5);
218 % set(arrowhandle(1), 'FaceColor', [0.1,0.8,0.2]);
219 % set(arrowhandle(2), 'FaceColor', [0.1,0.8,0.5]);
220 % arrowhandle(1, 1).AmbientStrength=0.7;
221 % arrowhandle(1, 2).AmbientStrength=0.7;
222 % arrowhandle(1, 2).DiffuseStrength=0.9;
223 % xlabel('Ex','FontSize',10,'Position',[0,-24,-4]);
224 % ylabel('Ey','FontSize',10,'Position',[24,0,-3.5]);
225 % zlabel('Ez','FontSize',10,'Position',[-23,-23,0]);
226 % axis([-18 18 -18 18 -3 3]);
227 % he.CameraPosition=[ 53.0738 ,-223.3648 , 35.1549];
228 % he.LineWidth=1;
229 % Etitle=sprintf('Electric Field (1,1,0) %d(kV/cm)',Eper(Enum
        ));
230 % title(Etitle,'Fontsize',10);
231 % he.Projection='perspective';
232 % end
233 % he.Position=[0.7733 , 0.1017 , 0.1876 , 0.1613];
```

```
234  % he . Projection='perspective ';
235  % he . GridColor
        =[0.313725490196078 ,0.313725490196078 ,0.313725490196078];
236  % he . GridAlpha=0.2;
237  % lighting gouraud ;
238  % camlight right ;
239
240  % figurespin . InvertHardcopy = 'off ';
241  %
242  % digits (2) ;
243  % filename=sprintf ('%d',Enum);
244  % % saveas ( figurespin , filename ,'jpeg ') ;
245  % saveas ( figurespin , filename ,' tiff ') ;
246  clear figurespin ;
247
248  clear Position2 binningplot binningxbin binningxbinybin ;
```

B.9 Spin movie generation

```
1   % Spin movie
2   SpinImage1=c e l l (57 ,1) ;
3   SpinImage2=c e l l (60 ,1) ;
4   SpinImage3=c e l l (22 ,1) ;
5
6   for  i =1:57
7         Imagefilename=sprintf ( '%d. tif ',i);
8   %        fullname=fullfile ('pictures cylinder ',Imagefilename);
9         SpinImage1{i}=imread ( Imagefilename ) ;
10        Imageperframe1=4;
11  end
```

```matlab
12
% for i=1:60
%         Imagefilename=sprintf('%d.tif',i);
%         fullname=fullfile('Camera rotation top down to flat',
     Imagefilename);
%         SpinImage2{i}=imread(fullname);
%         Imageperframe2=1;
% end
%
% for i=1:22
%         Imagefilename=sprintf('%d.tif',i);
%         fullname=fullfile('top down',Imagefilename);
%         SpinImage3{i}=imread(fullname);
%         Imageperframe3=4;
% end

 % create the video writer with 1 fps
 writerObj = VideoWriter('Spin animation all plane E(-1,1,0)
     3 angle');
 writerObj.FrameRate = 10;
%   writerObj.Quality=80;
 % open the video writer
 open(writerObj);
 for u=1:length(SpinImage1)
     for v=1:Imageperframe1
       writeVideo(writerObj, SpinImage1{u});
     end
 end

```

188

```matlab
39 %    for u=1:length(SpinImage2)
40 %        for v=1:Imageperframe2
41 %        writeVideo(writerObj, SpinImage2{u});
42 %        end
43 %  end
44 %
45 %    for u=1:length(SpinImage3)
46 %        for v=1:Imageperframe3
47 %        writeVideo(writerObj, SpinImage3{u});
48 %        end
49 %  end
50    close(writerObj);
```

B.10 Arrowplot modified from online sources

```matlab
1  function arrowHandle = arrow3Dmaxy(pos, deltaValues,
       colorCode, stemRatio)
2
3  % arrowHandle = arrow3D(pos, deltaValues, colorCode,
       stemRatio)
       %%%%%%%%%%%%%%%%%%%%%%%%%%%%%%%%%%%%%%%%%%%%%%%%%%%%%%%%%%%%%%%%%%%%%%%%%%%%%%%%%%%%%%

4  %
5  %    Used to plot a single 3D arrow with a cylindrical stem
       and cone arrowhead
6  %      pos = [X,Y,Z] - spatial location of the starting point
       of the arrow (end of stem)
7  %      deltaValues = [QX,QY,QZ] - delta parameters denoting
       the magnitude of the arrow along the x,y,z-axes (relative
       to 'pos')
```

189

```matlab
8  %       colorCode − Color parameters as per the 'surf' command.
       For example, 'r', 'red', [1 0 0] are all examples of a
      red−colored arrow
9  %       stemRatio − The ratio of the length of the stem in
       proportion to the arrowhead.  For example, a call of:
10 %                   arrow3D([0,0,0], [100,0,0] , 'r', 0.82)
       will produce a red arrow of magnitude 100, with the
       arrowstem spanning a distance
11 %                   of 82 (note 0.82 ratio of length 100) while
        the arrowhead (cone) spans 18.
12 %
13 %      Example:
14 %        arrow3D([0,0,0], [4,3,7]);  %—— arrow with default
       parameters
15 %         axis equal;
16 %
17 %    Author: Shawn Arseneau
18 %    Created: September 14, 2006
19 %    Updated: September 18, 2006
20 %
21 %
     %%%%%%%%%%%%%%%%%%%%%%%%%%%%%%%%%%%%%%%%%%%%%%%%%%%%%%%%%%%%%%%%%%%%%%%%%%%%%%%%%%%

22      if nargin<2 || nargin>4
23          error('Incorrect number of inputs to arrow3D');
24      end
25      if numel(pos)~=3 || numel(deltaValues)~=3
26          error('pos and/or deltaValues is incorrect dimensions
                (should be three)');
```

```matlab
27      end
28      if nargin<3
29          colorCode = 'interp';
30      end
31      if nargin<4
32          stemRatio = 0.75;
33      end
34
35      X = pos(1); %—— with this notation, there is no need to
            transpose if the user has chosen a row vs col vector
36      Y = pos(2);
37      Z = pos(3);
38
39      [sphi, stheta, srho] = cart2sph(deltaValues(1),
            deltaValues(2), deltaValues(3));
40
41      %********************************************* CYLINDER ==
            STEM *********************************************
42      cylinderRadius = 0.2*srho;
43      if (cylinderRadius > 0.08)
44          cylinderRadius = 0.08;
45      end
46      cylinderLength = srho*stemRatio;
47      [CX,CY,CZ] = cylinder(cylinderRadius);
48      CZ = CZ.*cylinderLength;     %—— lengthen
49
50      %—— ROTATE CYLINDER
51      [row, col] = size(CX);       %—— initial rotation to
            coincide with X—axis
```

```matlab
52
53      newEll = rotatePoints([0 0 -1], [CX(:), CY(:), CZ(:)]);
54      CX = reshape(newEll(:,1), row, col);
55      CY = reshape(newEll(:,2), row, col);
56      CZ = reshape(newEll(:,3), row, col);
57
58      [row, col] = size(CX);
59      newEll = rotatePoints(deltaValues, [CX(:), CY(:), CZ(:)])
            ;
60      stemX = reshape(newEll(:,1), row, col);
61      stemY = reshape(newEll(:,2), row, col);
62      stemZ = reshape(newEll(:,3), row, col);
63
64      %—— TRANSLATE CYLINDER
65      stemX = stemX + X;
66      stemY = stemY + Y;
67      stemZ = stemZ + Z;
68
69
70      %********************************************* CONE ==
            ARROWHEAD
            *********************************************
71      coneLength = srho*(1-stemRatio);
72      coneRadius = cylinderRadius*1.5;
73      incr = 8;  %—— Steps of cone increments
74      coneincr = coneRadius/incr;
75      [coneX, coneY, coneZ] = cylinder(cylinderRadius*1.5:-
            coneincr:0);  %————— CONE
76      coneZ = coneZ.*coneLength;
```

192

```matlab
77
78        %——— ROTATE CONE
79        [row, col] = size(coneX);
80        newEll = rotatePoints([0 0 -1], [coneX(:), coneY(:),
              coneZ(:)]);
81        coneX = reshape(newEll(:,1), row, col);
82        coneY = reshape(newEll(:,2), row, col);
83        coneZ = reshape(newEll(:,3), row, col);
84
85        newEll = rotatePoints(deltaValues, [coneX(:), coneY(:),
              coneZ(:)]);
86        headX = reshape(newEll(:,1), row, col);
87        headY = reshape(newEll(:,2), row, col);
88        headZ = reshape(newEll(:,3), row, col);
89
90        %—— TRANSLATE CONE
91        V = [0, 0, srho*stemRatio];     %—— centerline for
              cylinder: the multiplier is to set the cone 'on the
              rim' of the cylinder
92        Vp = rotatePoints([0 0 -1], V);
93        Vp = rotatePoints(deltaValues, Vp);
94        headX = headX + Vp(1) + X;
95        headY = headY + Vp(2) + Y;
96        headZ = headZ + Vp(3) + Z;
97        %
              *******************************************************
98        hStem = surf(stemX, stemY, stemZ, 'FaceColor', colorCode,
              'EdgeColor', 'none');
```

```matlab
99        hold on;
100       hHead = surf(headX, headY, headZ, 'FaceColor', colorCode,
             'EdgeColor', 'none');
101
102       if nargout==1
103           arrowHandle = [hStem, hHead];
104       end
```

```matlab
1   function arrowHandle = arrow3Dmaxy(pos, deltaValues,
        colorCode, stemRatio)
2
3   % arrowHandle = arrow3D(pos, deltaValues, colorCode,
        stemRatio)
        %%%%%%%%%%%%%%%%%%%%%%%%%%%%%%%%%%%%%%%%%%%%%%%%%%%%%%%%%%%%%%%%%%%%%%%%%%%%%%%%%%%
4   %
5   %       Used to plot a single 3D arrow with a cylindrical stem
        and cone arrowhead
6   %       pos = [X,Y,Z] - spatial location of the starting point
        of the arrow (end of stem)
7   %       deltaValues = [QX,QY,QZ] - delta parameters denoting
        the magnitude of the arrow along the x,y,z-axes (relative
        to 'pos')
8   %       colorCode - Color parameters as per the 'surf' command.
         For example, 'r', 'red', [1 0 0] are all examples of a
        red-colored arrow
9   %       stemRatio - The ratio of the length of the stem in
        proportion to the arrowhead.  For example, a call of:
```

```matlab
10  %                       arrow3D([0,0,0], [100,0,0] , 'r', 0.82)
       will produce a red arrow of magnitude 100, with the
       arrowstem spanning a distance
11  %                       of 82 (note 0.82 ratio of length 100) while
        the arrowhead (cone) spans 18.
12  %
13  %       Example:
14  %           arrow3D([0,0,0], [4,3,7]);   %—— arrow with default
       parameters
15  %            axis equal;
16  %
17  %     Author: Shawn Arseneau
18  %     Created: September 14, 2006
19  %     Updated: September 18, 2006
20  %
21  %
       %%%%%%%%%%%%%%%%%%%%%%%%%%%%%%%%%%%%%%%%%%%%%%%%%%%%%%%%%%%%%%%%%%%%%%%%%%%%%%%%%%%%%%

22      if nargin<2 || nargin>4
23          error('Incorrect number of inputs to arrow3D');
24      end
25      if numel(pos)~=3 || numel(deltaValues)~=3
26          error('pos and/or deltaValues is incorrect dimensions
               (should be three)');
27      end
28      if nargin<3
29          colorCode = 'interp';
30      end
31      if nargin<4
```

195

```matlab
32        stemRatio = 0.75;
33     end
34
35     X = pos(1); %———— with this notation, there is no need to
              transpose if the user has chosen a row vs col vector
36     Y = pos(2);
37     Z = pos(3);
38
39     [sphi, stheta, srho] = cart2sph(deltaValues(1),
           deltaValues(2), deltaValues(3));
40
41     %*********************************************** CYLINDER ==
              STEM ***********************************************
42     cylinderRadius = 0.75;
43     cylinderLength = srho*stemRatio;
44     [CX,CY,CZ] = cylinder(cylinderRadius);
45     CZ = CZ.*cylinderLength;       %———— lengthen
46
47     %———— ROTATE CYLINDER
48     [row, col] = size(CX);         %———— initial rotation to
              coincide with X-axis
49
50     newEll = rotatePoints([0 0 -1], [CX(:), CY(:), CZ(:)]);
51     CX = reshape(newEll(:,1), row, col);
52     CY = reshape(newEll(:,2), row, col);
53     CZ = reshape(newEll(:,3), row, col);
54
55     [row, col] = size(CX);
```

```matlab
56    newEll = rotatePoints(deltaValues, [CX(:), CY(:), CZ(:)])
          ;
57    stemX = reshape(newEll(:,1), row, col);
58    stemY = reshape(newEll(:,2), row, col);
59    stemZ = reshape(newEll(:,3), row, col);
60
61    %————— TRANSLATE CYLINDER
62    stemX = stemX + X;
63    stemY = stemY + Y;
64    stemZ = stemZ + Z;
65
66    %********************************************** CONE ==
          ARROWHEAD
          **********************************************
67    coneLength = srho*(1-stemRatio);
68    coneRadius = cylinderRadius*1.5;
69    incr = 4;   %———— Steps of cone increments
70    coneincr = coneRadius/incr;
71    [coneX, coneY, coneZ] = cylinder(cylinderRadius*1.5:-
          coneincr:0);   %———————— CONE
72    coneZ = coneZ.*coneLength;
73
74    %————— ROTATE CONE
75    [row, col] = size(coneX);
76    newEll = rotatePoints([0 0 -1], [coneX(:), coneY(:),
          coneZ(:)]);
77    coneX = reshape(newEll(:,1), row, col);
78    coneY = reshape(newEll(:,2), row, col);
79    coneZ = reshape(newEll(:,3), row, col);
```

```matlab
80
81         newEll = rotatePoints(deltaValues, [coneX(:), coneY(:),
              coneZ(:)]);
82         headX = reshape(newEll(:,1), row, col);
83         headY = reshape(newEll(:,2), row, col);
84         headZ = reshape(newEll(:,3), row, col);
85
86         %—— TRANSLATE CONE
87         V = [0, 0, srho*stemRatio];     %—— centerline for
              cylinder: the multiplier is to set the cone 'on the
              rim' of the cylinder
88         Vp = rotatePoints([0 0 -1], V);
89         Vp = rotatePoints(deltaValues, Vp);
90         headX = headX + Vp(1) + X;
91         headY = headY + Vp(2) + Y;
92         headZ = headZ + Vp(3) + Z;
93         %
                ***************************************************************
94         hStem = surf(stemX, stemY, stemZ, 'FaceColor', colorCode,
              'EdgeColor', 'none');
95         hold on;
96         hHead = surf(headX, headY, headZ, 'FaceColor', colorCode,
              'EdgeColor', 'none');
97
98         if nargout==1
99             arrowHandle = [hStem, hHead];
100        end
```

```
1  function arrowHandle = arrow3Dmaxy(pos, deltaValues,
       colorCode, stemRatio)
2
3  % arrowHandle = arrow3D(pos, deltaValues, colorCode,
       stemRatio)
       %%%%%%%%%%%%%%%%%%%%%%%%%%%%%%%%%%%%%%%%%%%%%%%%%%%%%%%%%%%%%%%%%%%%%%%%%%%%%%%%%%%%%%%%%%%%%

4  %
5  %     Used to plot a single 3D arrow with a cylindrical stem
       and cone arrowhead
6  %       pos = [X,Y,Z] - spatial location of the starting point
       of the arrow (end of stem)
7  %       deltaValues = [QX,QY,QZ] - delta parameters denoting
       the magnitude of the arrow along the x,y,z-axes (relative
       to 'pos')
8  %       colorCode - Color parameters as per the 'surf' command.
         For example, 'r', 'red', [1 0 0] are all examples of a
       red-colored arrow
9  %       stemRatio - The ratio of the length of the stem in
       proportion to the arrowhead.  For example, a call of:
10 %                    arrow3D([0,0,0], [100,0,0] , 'r', 0.82)
       will produce a red arrow of magnitude 100, with the
       arrowstem spanning a distance
11 %                    of 82 (note 0.82 ratio of length 100) while
        the arrowhead (cone) spans 18.
12 %
13 %       Example:
14 %          arrow3D([0,0,0], [4,3,7]);   %-- arrow with default
       parameters
```

199

```matlab
15  %           axis  equal ;
16  %
17  %      Author :  Shawn  Arseneau
18  %      Created :  September  14 ,  2006
19  %      Updated :  September  18 ,  2006
20  %
21  %
    %%%%%%%%%%%%%%%%%%%%%%%%%%%%%%%%%%%%%%%%%%%%%%%%%%%%%%%%%%%%%%%%%%%%%%%%%%%%%%%%%%

22      if  nargin <2  ||  nargin >4
23          error ( ' Incorrect  number  of  inputs  to  arrow3D ' ) ;
24      end
25      if  numel ( pos )~=3  ||  numel ( deltaValues )~=3
26          error ( ' pos  and/or  deltaValues  is  incorrect  dimensions
                 ( should  be  three ) ' ) ;
27      end
28      if  nargin <3
29          colorCode  =  ' interp ' ;
30      end
31      if  nargin <4
32          stemRatio  =  0.75 ;
33      end
34
35  X  =  pos ( 1 ) ;  %——  with  this  notation ,  there  is  no  need  to
             transpose  if  the  user  has  chosen  a  row  vs  col  vector
36  Y  =  pos ( 2 ) ;
37  Z  =  pos ( 3 ) ;
38
```

```matlab
39      [sphi, stheta, srho] = cart2sph(deltaValues(1),
            deltaValues(2), deltaValues(3));
40
41      %***************************************** CYLINDER ==
            STEM *****************************************
42      cylinderRadius = 25;
43      cylinderLength = srho*stemRatio;
44      [CX,CY,CZ] = cylinder(cylinderRadius);
45      CZ = CZ.*cylinderLength;      %—— lengthen
46
47      %—— ROTATE CYLINDER
48      [row, col] = size(CX);      %—— initial rotation to
            coincide with X-axis
49
50      newEll = rotatePoints([0 0 -1], [CX(:), CY(:), CZ(:)]);
51      CX = reshape(newEll(:,1), row, col);
52      CY = reshape(newEll(:,2), row, col);
53      CZ = reshape(newEll(:,3), row, col);
54
55      [row, col] = size(CX);
56      newEll = rotatePoints(deltaValues, [CX(:), CY(:), CZ(:)])
            ;
57      stemX = reshape(newEll(:,1), row, col);
58      stemY = reshape(newEll(:,2), row, col);
59      stemZ = reshape(newEll(:,3), row, col);
60
61      %—— TRANSLATE CYLINDER
62      stemX = stemX + X;
63      stemY = stemY + Y;
```

```
64      stemZ = stemZ + Z;

65

66      %********************************************** CONE ==
           ARROWHEAD
           **********************************************
67      coneLength = srho*(1−stemRatio);
68      coneRadius = cylinderRadius*1.5;
69      incr = 8;  %──── Steps of cone increments
70      coneincr = coneRadius/incr;
71      [coneX, coneY, coneZ] = cylinder(cylinderRadius*1.5:−
           coneincr:0);  %──────── CONE
72      coneZ = coneZ.*coneLength;

73

74      %──── ROTATE CONE
75      [row, col] = size(coneX);
76      newEll = rotatePoints([0 0 −1], [coneX(:), coneY(:),
           coneZ(:)]);
77      coneX = reshape(newEll(:,1), row, col);
78      coneY = reshape(newEll(:,2), row, col);
79      coneZ = reshape(newEll(:,3), row, col);

80

81      newEll = rotatePoints(deltaValues, [coneX(:), coneY(:),
           coneZ(:)]);
82      headX = reshape(newEll(:,1), row, col);
83      headY = reshape(newEll(:,2), row, col);
84      headZ = reshape(newEll(:,3), row, col);

85

86      %──── TRANSLATE CONE
```

```matlab
87        V = [0, 0, srho*stemRatio];      %——— centerline for
              cylinder: the multiplier is to set the cone 'on the
              rim' of the cylinder
88        Vp = rotatePoints([0 0 -1], V);
89        Vp = rotatePoints(deltaValues, Vp);
90        headX = headX + Vp(1) + X;
91        headY = headY + Vp(2) + Y;
92        headZ = headZ + Vp(3) + Z;
93        %
              ************************************************************

94        hStem = surf(stemX, stemY, stemZ, 'FaceColor', colorCode,
              'EdgeColor', 'none');
95        hold on;
96        hHead = surf(headX, headY, headZ, 'FaceColor', colorCode,
              'EdgeColor', 'none');
97
98        if nargout==1
99            arrowHandle = [hStem, hHead];
100       end

1  function arrowHandle = arrow3Dmaxy(pos, deltaValues,
       colorCode, stemRatio)
2
3  % arrowHandle = arrow3D(pos, deltaValues, colorCode,
       stemRatio)
       %%%%%%%%%%%%%%%%%%%%%%%%%%%%%%%%%%%%%%%%%%%%%%%%%%%%%%%%%%%%%%%%%%%%%%

4  %
```

```
5  %        Used  to  plot  a  single  3D  arrow  with  a  cylindrical  stem
         and  cone  arrowhead
6  %        pos  =  [X,Y,Z]  −  spatial  location  of  the  starting  point
         of  the  arrow  (end  of  stem)
7  %        deltaValues  =  [QX,QY,QZ]  −  delta  parameters  denoting
         the  magnitude  of  the  arrow  along  the  x,y,z−axes  (relative
         to  'pos')
8  %        colorCode  −  Color  parameters  as  per  the  'surf'  command.
           For  example,  'r',  'red',  [1  0  0]  are  all  examples  of  a
         red−colored  arrow
9  %        stemRatio  −  The  ratio  of  the  length  of  the  stem  in
         proportion  to  the  arrowhead.  For  example,  a  call  of:
10 %                  arrow3D([0,0,0],  [100,0,0]  ,  'r',  0.82)
         will  produce  a  red  arrow  of  magnitude  100,  with  the
         arrowstem  spanning  a  distance
11 %                  of  82  (note  0.82  ratio  of  length  100)  while
          the  arrowhead  (cone)  spans  18.
12 %
13 %        Example:
14 %        arrow3D([0,0,0],  [4,3,7]);  %—— arrow  with  default
         parameters
15 %        axis  equal;
16 %
17 %    Author:  Shawn  Arseneau
18 %    Created:  September  14,  2006
19 %    Updated:  September  18,  2006
20 %
```

```matlab
21   %
     %%%%%%%%%%%%%%%%%%%%%%%%%%%%%%%%%%%%%%%%%%%%%%%%%%%%%%%%%%%%%%%%%%%%%%%%%%%%%%%%%%%%%%%%%%%%%%%%%%%%%%%

22       if nargin<2 || nargin>4
23           error('Incorrect number of inputs to arrow3D');
24       end
25       if numel(pos)~=3 || numel(deltaValues)~=3
26           error('pos and/or deltaValues is incorrect dimensions
                    (should be three)');
27       end
28       if nargin<3
29           colorCode = 'interp';
30       end
31       if nargin<4
32           stemRatio = 0.75;
33       end
34
35       X = pos(1); %----- with this notation, there is no need to
                     transpose if the user has chosen a row vs col vector
36       Y = pos(2);
37       Z = pos(3);
38
39       [sphi, stheta, srho] = cart2sph(deltaValues(1),
             deltaValues(2), deltaValues(3));
40
41       %********************************************** CYLINDER ==
             STEM **********************************************
42       cylinderRadius = 0.05;
43       cylinderLength = srho*stemRatio;
```

```
44      [CX,CY,CZ] = cylinder(cylinderRadius);
45      CZ = CZ.*cylinderLength;      %——— lengthen
46
47      %——— ROTATE CYLINDER
48      [row, col] = size(CX);      %——— initial rotation to
           coincide with X-axis
49
50      newEll = rotatePoints([0 0 -1], [CX(:), CY(:), CZ(:)]);
51      CX = reshape(newEll(:,1), row, col);
52      CY = reshape(newEll(:,2), row, col);
53      CZ = reshape(newEll(:,3), row, col);
54
55      [row, col] = size(CX);
56      newEll = rotatePoints(deltaValues, [CX(:), CY(:), CZ(:)])
           ;
57      stemX = reshape(newEll(:,1), row, col);
58      stemY = reshape(newEll(:,2), row, col);
59      stemZ = reshape(newEll(:,3), row, col);
60
61      %——— TRANSLATE CYLINDER
62      stemX = stemX + X;
63      stemY = stemY + Y;
64      stemZ = stemZ + Z;
65
66      %******************************************* CONE ==
           ARROWHEAD
           ***********************************************
67      coneLength = srho*(1-stemRatio);
68      coneRadius = cylinderRadius*1.5;
```

```matlab
69        incr = 8;   %—— Steps of cone increments
70        coneincr = coneRadius/incr;
71        [coneX, coneY, coneZ] = cylinder(cylinderRadius*1.5:−
             coneincr:0);   %———————— CONE
72        coneZ = coneZ.*coneLength;
73
74        %—— ROTATE CONE
75        [row, col] = size(coneX);
76        newEll = rotatePoints([0 0 −1], [coneX(:), coneY(:),
             coneZ(:)]);
77        coneX = reshape(newEll(:,1), row, col);
78        coneY = reshape(newEll(:,2), row, col);
79        coneZ = reshape(newEll(:,3), row, col);
80
81        newEll = rotatePoints(deltaValues, [coneX(:), coneY(:),
             coneZ(:)]);
82        headX = reshape(newEll(:,1), row, col);
83        headY = reshape(newEll(:,2), row, col);
84        headZ = reshape(newEll(:,3), row, col);
85
86        %—— TRANSLATE CONE
87        V = [0, 0, srho*stemRatio];    %—— centerline for
             cylinder: the multiplier is to set the cone 'on the
             rim' of the cylinder
88        Vp = rotatePoints([0 0 −1], V);
89        Vp = rotatePoints(deltaValues, Vp);
90        headX = headX + Vp(1) + X;
91        headY = headY + Vp(2) + Y;
92        headZ = headZ + Vp(3) + Z;
```

```matlab
%
% *********************************************************************

hStem = surf(stemX, stemY, stemZ, 'FaceColor', colorCode, ...
    'EdgeColor', 'none');
hold on;
hHead = surf(headX, headY, headZ, 'FaceColor', colorCode, ...
    'EdgeColor', 'none');

if nargout==1
    arrowHandle = [hStem, hHead];
end
```

Appendix C

REPRINTS RIGHTS

The respective publishers provided permissions for reprinting figures published in this dissertation. A list for all the permissions is attached.


Figure C.1: Reprint rights obtained from Rightslink

Figure C.2: Reprint rights obtained from SCIPRIS